FAR-ULTRAVIOLET MOLECULAR HYDROGEN FLUORESCENCE IN PHOTODISSOCIATION REGIONS

by

Kevin C. France

A dissertation submitted to The Johns Hopkins University in conformity with the requirements for the degree of Doctor of Philosophy.

Baltimore, Maryland

November, 2005

Abstract

Molecular hydrogen constitutes a large fraction of the baryonic matter in the universe and plays a role in regulating the physics and chemistry of many astrophysical environments. It is an important coolant during the formation of the first structures in the universe, is the dominant mass component in star-forming regions today, and is ubiquitous in the interstellar medium. As a homonuclear molecule, it has no permanent electric dipole moment, but the quadrupole rovibrational transitions provide diagnostic information about the physical state of interstellar clouds. Electronic transitions of the molecule are allowed and the absorption lines arising from these transitions are used to probe the physical conditions of the interstellar medium. However, the subsequent emission that is the dominant de-excitation route of the molecule is poorly constrained by both observations and theory. The purpose of this dissertation is to examine molecular hydrogen by using new and existing ultraviolet observations to test models of the fluorescent emission process.

This dissertation will report on new observations made by sounding rocket experiments and the *Far Ultraviolet Spectroscopic Explorer* to expand the observational basis for molecular hydrogen studies. This new data set allows us to explore models of ultraviolet fluorescence under a range of astrophysical conditions. The observational survey includes a variety of photodissociation regions, including the emission nebula IC 63, the star-forming region near the Orion Nebula, the emission/reflection nebula IC 405, and the pure reflection nebulae NGC 2023 and NGC 7023. We detect the fluorescent signature in the first three objects, and we use these data to develop the first model of this emission that is consistent with observation. We do not detect hydrogen fluorescence as presently understood in the latter two objects, and explanations are discussed.

Acknowledgements

"I know what I believe. I will continue to articulate what I believe and what I believe – I believe what I believe is right." – George W. Bush

This thesis would not have been possible without the guidance and support of my academic and research advisors, Paul Feldman and Stephan McCandliss. The faith they showed by offering me a research position before my first day of graduate school has been a constant source of motivation over the last six years, I hope they are not too disappointed with the investment. From the rocket flight during my first year at Hopkins, getting me through written and oral exams, and their patient tolerance of the quality of my research writing, I have enjoyed working with them and offer my most sincere thanks. That being said, I also would like to thank the group in Boston for making me employable by the JHU Rocket Group, specifically Supriya Chakrabarti, Dan Cotton, and Tim Cook.

It goes without saying that I certainly would have never even made it to graduate school without the unfaltering support of my family. My Mom and Dad have never once hesitated to support my educational goals, from paying for college (BU: All of the Ivy League cost without the pesky prestige) to constantly encouraging me to pursue a graduate career in a field I considered worthwhile. I would also like to thank my brother and sister, Patrick and Brittney. My thesis has also been strongly motivated by my oldest and truest friend, Emily Calwell. It was my relationship with her that first led me to think beyond a conventional and traditional career path (becoming the *other* kind of doctor). She has always backed my choices, even when they meant prolonging our physical separation. Her love, support, and commiseration about the ups and downs of academic life have been an immeasurable comfort over the ten years of college life.

I also have to thank a number of people in the JHU department of Physics and Astron-

Contents

x

List of Figures

List of Tables

Chapter 1

Introduction

*"...science will lead men into such confusion and confront them
with such dilemma and insoluble riddles that the fierce and
rebellious will destroy one another."* – Fyodor Dostoevsky

The material that fills the space between stars in the Milky Way, the interstellar medium (ISM), is made up of two dominant constituents. Gas and dust grains are the main components that are seen when astronomers look beyond our solar system. This interstellar gas and dust affect almost every astronomical observation at some level as the light we observe must necessarily travel through this intervening material on its way to Earth-borne or Earth-orbiting observatories. The gas in the ISM is made up of different temperature and ionization phases and a varying mix of atomic and molecular species. Interstellar dust is mainly composed of carbonaceous and silicate grains, also seen to vary in composition and ionization state.

The majority of the gas in the ISM is hydrogen. Hydrogen, made up of a single proton and electron, was created with the highest abundance following the Big Bang. It is still the most abundant element today, despite stellar processes that convert hydrogen into heavier elements. Hydrogen is present in atomic and molecular form in many phases of the ISM, from the tenuous diffuse regions of interstellar space, to the dense clouds of gas and dust that collapse to form stars. The abundance of hydrogen and its relatively early creation imply that the first baryonic structures in the universe were mainly comprised of hydrogen, and it played a vital role in the cooling that must have occurred in order to form the first

generation of stars. Molecular hydrogen (H$_2$) is particularly important for allowing individual pre-stellar clouds to cool below a few tens of thousands of degrees Kelvin, facilitating cloud collapse and star formation. A thermally (i.e. collisionally) excited atom or molecule removes energy from a cloud by emitting a photon, and energy dissapation from escaping photons has a cooling effect.

Molecular hydrogen is present at sites of star formation and in the cloud of gas and dust that surrounds the resultant new star(s). Depending on the mass of the star and its evolutionary stage, astronomers define different types of objects in which hydrogen is observed. Stars that are massive and produce a sufficient quantity of ultraviolet (UV) radiation to ionize the surrounding material are known as H II regions. An example of such a region is the Trapezium region of the Great Nebula in Orion (M42, Figure 1.1). If the star is less massive and the starlight is predominately scattered by dust grains, it is referred to as a reflection nebula. The well-known Pleiades star cluster illuminates a reflection nebula. There is not a well-defined boundary between the two cases, and many objects show both scattered starlight and emission lines from excited nebular gas species.

Figure 1.1 Left: A *Hubble Space Telescope* image of the Orion Nebula (M42), an example of an H II region. θ^1 Ori is the bright cluster at the center of the image (APOD/C. O'Dell and S. Wong). Right: An amateur astronomer image of the Pleiades reflection nebula (M45; APOD/M. Russell).

1.1 Molecular Hydrogen

Molecular hydrogen is not only present in these regions, but is the dominant molecular species both in terms of number and mass, yet it has traditionally been very challenging to study observationally. Modern astronomy has focused on the visible portion of the electromagnetic spectrum (3500 – 7500 Å). This range is the window through which Earth's atmosphere is transparent and light from distant objects can reach ground-based telescopes. H_2 does not have strong transitions in this wavelength regime, hence this dominant astrophysical molecule was only speculated about theoretically until relatively recently. The discovery of astronomical H_2 was made by Carruthers in 1970. Advances in infrared (IR) detector technology and space-based observatories have opened up the near and mid-IR spectral windows to astronomical study (Treffers et al., 1976). These spectral regimes are home to several H_2 transitions, and while widely used to determine physical properties of molecular gas, are still observationally challenging due to the weakness of the vibrational and rotational transitions of the molecule discussed below.

H_2 is a homonuclear molecule, and, as such, it has no intrinsic dipole moment as one finds in a molecule such as carbon monoxide. This lack of dipole moment means that excited rovibrational states radiate primarily through the slower channel of quadrupole transitions. H_2 can be excited (or *pumped*) into higher electronic states by the absorption of a far-UV photon ($912 \leq \lambda \leq 1110$ Å) coming from the UV radiation field of a star or by collisions with non-thermal electrons. The absorption of a far-UV photon causes an electronic excitation to a higher bound state (usually $B^1\Sigma_u^+$ or $C^1\Pi_u$), see Figure 1.2. There are no selection rules on the vibrational transitions that may occur during the electronic transition, and many excited vibrational levels of the upper electronic state may become populated during this process. The molecule then emits to a discrete vibrational level of the ground electronic state ($X^1\Sigma_g^+$), producing a fluorescent spectrum in the UV from 912 – 1650 Å (Sternberg, 1989). The molecule can then cascade back to the ground vibrational state via quadrupole transitions, producing a fluorescent spectrum in the near-infrared (Martini et al., 1999).

Figure 1.3 shows examples of both the far-UV and near-IR emission spectra of H_2. The far-UV spectrum was created using the code discussed in Chapter 2, the near-IR
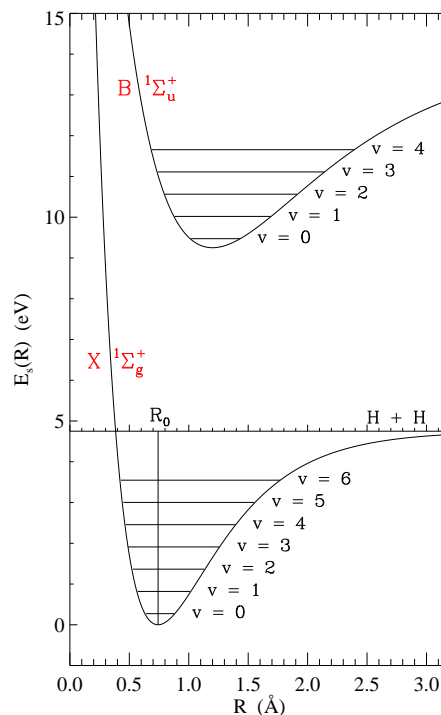
Figure 1.2 A schematic representation of the ground and first excited electronic states of the hydrogen molecule. The first few vibrational energy levels of each state are displayed as bands that give substructure to the electronic levels. Each vibrational level is further decomposed into individual roatational states, but these are below the resolution of this figure (Roberge, 2003).

spectrum comes from the rovibrational transitions of the molecule in the reflection nebula NGC 2023 (Martini et al., 1999). Approximately 10 - 15% of the time, this fluorescent pumping process will leave the molecule in the vibrational continuum of the ground electronic state, resulting in its dissociation (Stecher and Williams, 1967).

The stronger dipole allowed electronic transitions of molecular hydrogen are more abundant and thus easier to observe in principle. This is complicated by the difficulty in accessing the far-UV portion of the electromagnetic spectrum. Earth's atmosphere is opaque to radiation with wavelengths shorter than ~ 3000 Å, meaning that observing the far-UV spectrum described above requires a space-based instrument. This has been made possible over the past 40 years by sub-orbital rocket experiments as well as longer duration
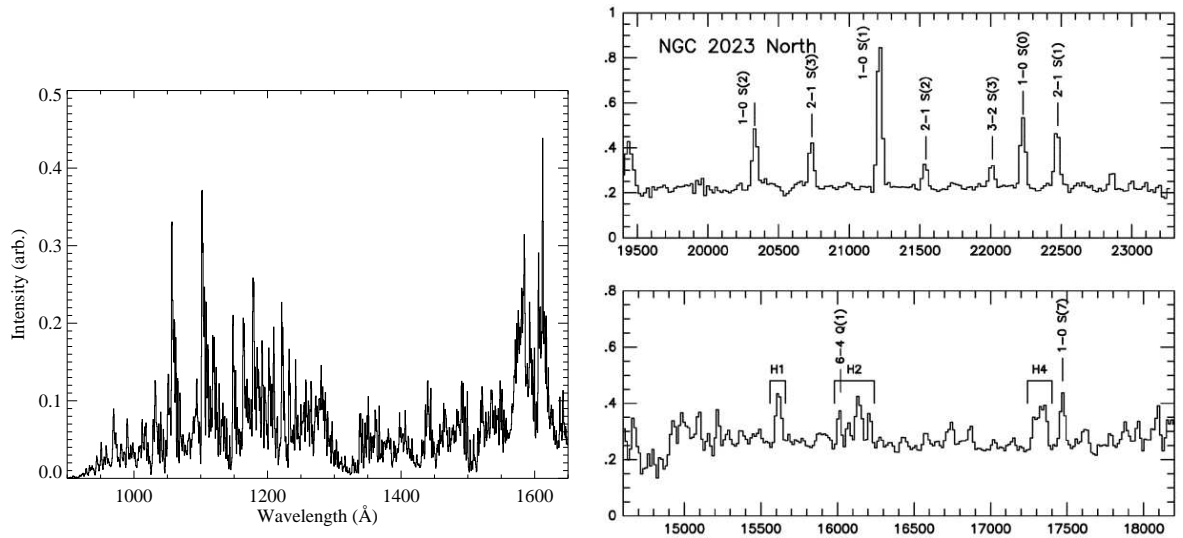
Figure 1.3 Examples of the far-UV and near-IR spectra of H_2. Left: A synthetic molecular hydrogen spectrum created with the code described in Chapter 2. This spectrum was created to simulate the expected laboratory performance of the LIDOS instrument described in Chapter 2 and the Appendix. Right: The near-IR spectrum of the reflection nebula NGC 2023 from Martini et al. (1999). A discussion of NGC 2023 is presented in Chapter 5.

observatories and instruments such as *Copernicus*, the *International Ultraviolet Explorer* (*IUE*), the Hopkins Ultraviolet Telescope (HUT), the instruments aboard the *Orbiting and Retrievable Far and Extreme Ultraviolet Spectrograph* (*ORFEUS*), the Space Telescope Imaging Spectrograph (STIS) and most recently the *Far Ultraviolet Spectroscopic Explorer* (*FUSE*). These instruments, in conjunction with observations in the IR, have enabled astronomers to confirm the existence of molecular hydrogen in a wide range of astronomical objects.

The physical conditions required for fluorescent excitation lead one to expect to observe H_2 in regions where there are enough far-UV photons to produce the excitation, but enough hydrogen molecules to generate an observable signal. Photodissociation regions (PDRs) are located at the interface of gas ionized by a stellar radiation and a dense cloud (Hollenbach and Tielens, 1997). PDRs exist in a variety of astronomical objects. In addition to the H II regions (Chrysostomou et al. 1993, Luhman et al. 1994, Kristensen et al. 2003) and reflection nebulae (Gatley et al. 1987, Takami et al. 2000), H_2 has been observed in stars

just being born (Wilkinson et al., 2002), atmospheres of low mass stars (Redfield et al., 2002), circumstellar disks around brown dwarfs (Gizis et al., 2005) systems of interacting stars (Wood and Karovska, 2004) and in the expanding envelopes of dying stars (e.g. planetary nebulae: Zuckerman & Gatley 1988, Luhman & Rieke 1996, Speck et al. 2002, Chapter 6). Finally, H_2 has been seen in absorption along many sightlines through the diffuse ISM (Spitzer et al., 1974; Rachford et al., 2002). The references listed above are a minute portion of the total census of galactic molecular hydrogen research in the literature.

1.2 Interstellar Dust

Interstellar dust grains are often found to be spatially correlated with H_2 (Witt et al., 1989; Werner et al., 2004). Grains are the primary formation site for H_2 in the present epoch (Hollenbach and Tielens, 1997). Hydrogen atoms are adsorbed onto a grain, and surface diffusion can bind two hydrogen atoms into a hydrogen molecule (Cazaux and Tielens, 2002). The hydrogen molecule then gives up some fraction of its binding energy ($E_{bind} \approx 4.5$ eV) and escapes from the grain in an excited rovibrational level of the ground electronic state. This excitation mechanism is known as formation pumping. The detailed physics of this process is an ongoing area of research, but it has been suggested that formation pumping could lead to significant deviations from a thermal rovibrational population of the ground electronic state (Takahashi and Uehara, 2001). Changes in the ground state population could alter the IR and far-UV emission spectra of H_2. In addition to the creation of new H_2 molecules, grains can shield molecules from UV photons that lead to their dissociation, allowing molecules to survive for long periods of time in intense UV radiation fields (Speck et al., 2002; Kristensen et al., 2003).

This shielding effect is also responsible for interstellar reddening - dust preferentially absorbing and scattering radiation with shorter wavelengths. Dust extinguishes UV light with a much greater efficiency than it does light at visible and infrared wavelengths (Cardelli et al., 1989; Fitzpatrick and Massa, 1990). The degree of differential absorption and scattering is seen to vary between different stars, and this gives rise to an extinction curve for an individual line of sight. Figure 1.4 shows examples of extinction curves for a few of the ob-

jects studied in this dissertation. With the exception of the purple attenuation curve derived for starburst galaxies by Leitherer et al. (2002), the curves (for Milky Way dust) are seen to show the same qualitative shape, with differences in the details. The two most prominent features of galactic extinction curves are the "blue bump" at 2175 Å ($\lambda^{-1} \sim 4.6\,\mu m^{-1}$) and a steep "far-UV rise" at the shortest wavelengths ($\lambda^{-1} \geq 8.0\,\mu m^{-1}$). Attenuation curves derived for dust located in the Small Magellenic Cloud, Lyman break galaxies, and many γ-ray burst host galaxies do show evidence for a blue-bump and display a more dramatic far-UV rise (Vijh et al., 2003).

Extinction curves are created by taking the ratio of the sightline of interest to a star of the same spectral type that does not show the effects of reddening, known as the pair method (Fitzpatrick and Massa 1990 and references therein). Correcting for brightness (i.e. distance) differences, the extinction curve is given in magnitudes of extinction, normalized by color excess E_{B-V} ($\equiv (B$ - $V)_{observed}$ - $(B$ - $V)_{theoretcal}$, where B and V are the stellar brightnesses in magnitudes). UV extinction curves are often fit by the six-parameter formalization of Fitzpatrick and Massa (1990). Figure 1.4 shows the curves computed using this method as solid lines, with the black dots derived directly from the pair method for the central star of IC 405, further described in Chapter 4. The blue triangles represent values of the observed average Milky Way extinction curve (Mathis, 1990). A survey of Milky Way extinction curves has recently been presented by Valencic et al. (2004).

The generic properties of the average interstellar extinction curve are well explained by models of dust composed of a mixture of carbonaceous grains and amorphous silicate grains (Draine, 2003b). Grain radii are thought to range between 50 and 10,000 Å (Weingartner and Draine, 2001), but the carbon grain population extends down to very small sizes (Draine, 2003b). The smallest grains are individual polycyclic aromatic hydrocarbons (PAHs, made up of chains of $\sim 20 - 10^5$ C atoms). Interstellar dust reprocesses the energy it absorbs in the UV to the IR portion of the electromagnetic spectrum. PAHs are seen to show strong mid-IR ($3 \leq \lambda \leq 20\,\mu$m) emission features in PDRs (Werner et al. 2004; Chapter 6), presumably heated by the absorption of a single photon (van Dishoeck, 2004). Larger grains are warmed by continuous exposure to UV photons and reradiate this thermally in the far-IR ($\lambda \geq 20\,\mu$m).
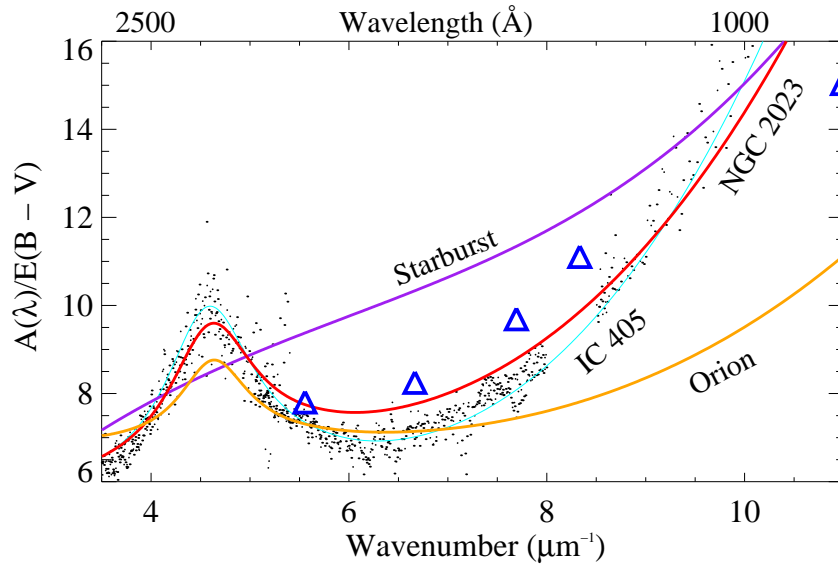
Figure 1.4 An example of several extinction curves. The black dots are an experimental curve, created using the pair method, combining the sounding rocket data of IC 405 (presented in Chapter 4) and archival *IUE* and HUT spectra. The cyan curve is a fit to the data using the parameterization of Fitzpatrick and Massa (1990). The red (NGC 2023) and orange (Orion) curves are other examples of Fitzpatrick and Massa (1990) extinction curves for lines of sight in the Milky Way. The blue triangles are the average galactic extinction, presented in the review of Mathis (1990). The purple (Starburst) curve is the average attenuation observed in external star-forming galaxies (Leitherer et al., 2002). It shows the far-UV rise seen in galactic extinction curves, but does not show the prominent 4.6 μm^{-1} feature.

1.3   Scientific Objectives

Much is now known about the properties of molecular hydrogen absorption and interstellar extinction in the diffuse ISM. Less is known about the ultraviolet emission properties of molecular hydrogen and the extinction properties (dust distributions) within individual PDRs where the gas and dust are being actively influenced by the ultraviolet radiation field of a star. Prior to this work, the one PDR for which an ultraviolet H_2 emission spectrum had been published, IC 63, differed with theoretical predictions by as much as an order of magnitude (Witt et al., 1989; Sternberg, 1989; Hurwitz, 1998). The complicated dust geometries within PDRs have led some authors to question the reliability of dust grain properties derived from observations of these objects (Mathis et al., 2002; Draine, 2003b).

Despite the fact that they are the strongest transitions of the most abundant molecules in molecule-rich environments, the far-UV emission lines of H_2 in PDRs have been studied little since the ability to do so became possible with the launch of *IUE* (Duley and Williams, 1980). The primary goal of this thesis is to measure and characterize the far-ultraviolet spectra of nearby PDRs (galactic emission and reflection nebulae) to determine the contribution to their spectra from molecular hydrogen, atomic species, and dust-scattered stellar light. This work presents new observations of several PDRs, determines the ionization state of the nebular material, and examines the relative contributions of the three components. These measurements provide constraints on models of PDRs, and this work addresses the large discrepancy in the expected and observed properties of photo-excited H_2 through modeling efforts. As dust is inexorably tied to molecular hydrogen, a secondary goal of this work addresses the suggested problems in using observations of gaseous nebulae to determine grain properties. This is accomplished by using simple dust models to compare with suitable observations (Burgh et al., 2002).

The ultraviolet data for this work comes from a number of space-based spectrographs. The two main instruments used in this dissertation are sounding rockets flown by the Johns Hopkins University Sounding Rocket Group and *FUSE*. Supporting observations come from archival data obtained with *IUE* and HUT. In the Appendix, a discussion of the details of the sounding rocket observations (such as absolute calibration determinations, development of science and calibration instruments, mission planning, etc.) is included.

The majority of the $FUSE$ data presented here were obtained through the $FUSE$ Guest Investigator Program.

Chapters 2 through 5 will focus on the far-UV spectra of individual PDRs. Chapter 2 deals with the emission/reflection nebula IC 63, the first object in which continuum-pumped fluorescence was detected (Witt et al., 1989). It brings together $FUSE$, HUT, and rocket observations aimed at measuring the extent of the H_2 emitting region and resolving the order of magnitude discrepancy between the shortest and longest ultraviolet wavelengths described by Hurwitz (1998). Chapter 3 addresses a diffuse region near the star-forming Orion Nebula observed by $FUSE$. This result shows the dominance of the Trapezium star θ^1 Ori C to the energetics of the region, and rules out shock-only models for explaining the near-IR emission from H_2 seen in previous studies. The subject of Chapter 4 is emission/reflection nebula IC 405. This work uses rocket and $FUSE$ data to study the molecular hydrogen fluorescence in the nebula, explore the nebular extinction properties, and presents a dust grain analysis. Chapters 2 through 4 have been published as articles in the Astrophysical Journal. Chapter 5 deals with the classical, well-studied reflection nebulae NGC 2023 and NGC 7023. These objects display no clear evidence for hydrogen emission in their $FUSE$ spectra despite the fact that it is seen in prior observations at longer UV wavelengths and in vibrational and rotational emission in the infrared (Martini et al., 1999; Takami et al., 2000; Burgh et al., 2002; Werner et al., 2004). Possible explanations are discussed. Chapter 6 will provide conclusions, summary, and possibilities for applying this work to future studies.

Chapter 2

Fluorescent Molecular Hydrogen Emission in IC 63: $FUSE$, HUT, and Rocket Observations

> *"There is considerable filamentous nebulosity*
> *in this region."*   – Edwin Hubble

2.1   Introduction to IC 63

Far-ultraviolet emission from molecular hydrogen was first predicted to be detectable in diffuse objects by Duley and Williams (1980). Witt et al. (1989) detected this emission in IC 63 with the Short Wavelength Primary (SWP) camera on IUE, representing the first astronomical detection of the ultraviolet H_2 fluorescence spectrum pumped by a continuum source. Luhman et al. (1997) reported the detection of the near-infrared emission spectrum of fluorescent H_2, making IC 63 the first object seen to exhibit both the ultraviolet and infrared emission from H_2 excited by ultraviolet continuum photons. Hurwitz (1998) presented the first spectrum of IC 63 at wavelengths shorter than the IUE bandpass, using the Berkeley Extreme and Far-ultraviolet Spectrograph aboard $ORFEUS-II$.

IC 63 is a bright emission/reflection nebula illuminated by the hot star γ Cas (HD 5394), a lightly reddened B0.5 IV star ($E_{B-V} = 0.03$; Hurwitz 1998). Assuming that the star and

the nebula are co-spatial at a distance of ≈ 200 pc, the bright optical nebula is projected to be 1.3 pc from the star (Figure 4.1). A number of arguments are given in the literature to support fluorescent pumping by the ultraviolet continuum of γ Cas as the process that gives rise to the H_2 emission observed by Witt et al. (1989), Luhman et al. (1997), and Hurwitz (1998). Witt et al. (1989) present calculations of the energy budgets for competing processes such as a collisional excitation from a stellar wind or non-thermal excitation from electrons produced by stellar X-rays, and find that these explanations are insufficient to reproduce the nebular brightness observed in IC 63. The infrared H_2 line ratios seen by Luhman et al. (1997) are consistent with fluorescence rather than collisional excitation. Hurwitz (1998) discounts the possibilities of shocks by the narrow line widths seen in sub-mm molecular observations (Jansen et al., 1994), but finds that models of UV fluorescence overpredict the amount of far-UV emission observed. Hurwitz (1998) found that the absolute flux of the far-UV emission lines were an order of magnitude fainter than what would be expected based on the longer wavelength ultraviolet lines.

This chapter presents the results of *Far Ultraviolet Spectroscopic Explorer* (*FUSE*) and Hopkins Ultraviolet Telescope (HUT) observations of IC 63. The high spectral resolution of *FUSE* enables us to separate fluorescent emission from the dust scattered continuum and resolve the lines into their individual rotational components. The HUT observation covers the entire 912 – 1650 Å region spanned by the fluorescent emission. Additionally, we present the far-UV spectrum of the incident radiation field from γ Cas obtained with a rocket-borne spectrograph. This data has been used to calibrate a high-resolution scattered light spectrum from *FUSE*, allowing us to model the fluorescent H_2 using realistic physical parameters for the exciting radiation field.

2.2 Far-Ultraviolet Observations of the IC 63 System

2.2.1 Sounding Rocket Observation of γ Cas

γ Cas was observed by a rocket-borne spectrograph in 2003 December. This was the first flight of the Long-slit Imaging Dual-Order Spectrograph (LIDOS, McCandliss et al. 2003). LIDOS employs two complimentary ultraviolet-sensitive detectors to achieve a large
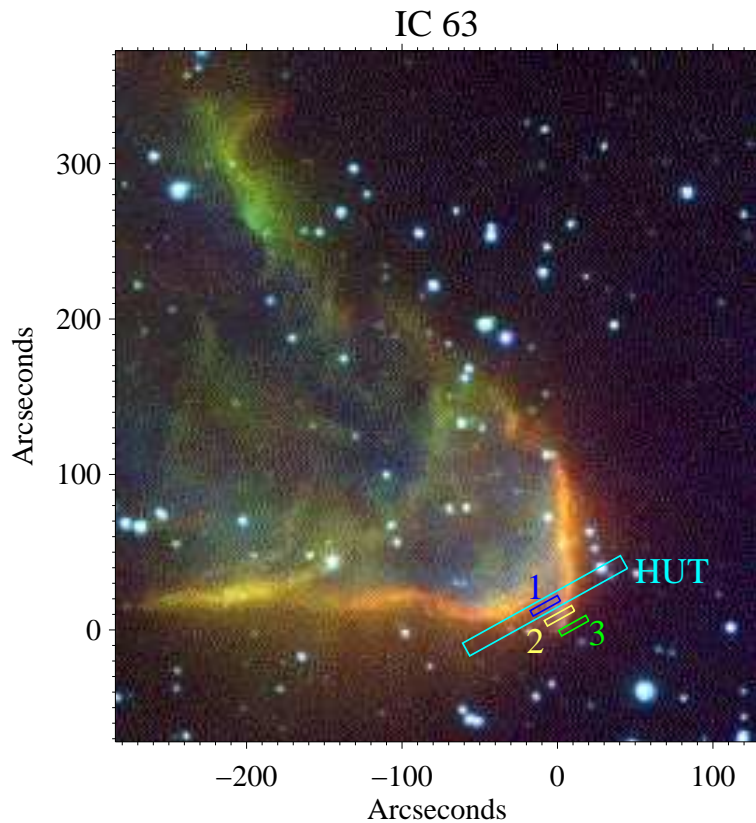
Figure 2.1 IC 63 with relevant aperture overlays. γ Cas is located approximately $20'$ to the southwest. The image was taken with the WIYN 0.9-meter, courtesy of Eric B. Burgh.

dynamic range in flux for imaging spectroscopy. An updated version of the Faint Object Telescope (0.4-meter diameter, f/15.7 Dall-Kirkham; Hartig et al. 1980; McCandliss et al. 1994; France et al. 2004) focuses light at the entrance aperture of the spectrograph, a mirrored slit-jaw into which a long-slit ($10'' \times 300''$) is etched. The light entering the 600 mm diameter Rowland spectrograph is dispersed by a silicon carbide grating. Far-UV light diffracted in the +1 order ($900 - 1590$ Å) is recorded by a windowless δ-doped CCD that is sensitive to bright objects whereas the -1 order UV light ($930 - 1680$ Å) is recorded by a photon-counting micro-channel plate (MCP) detector with a CsI photocathode, read out by a double delay-line anode (McPhate et al., 1999). The MCP detector has a low background

equivalent flux, extending our detection limit towards fainter diffuse objects.

LIDOS was launched aboard a Black Brant IX sounding rocket (NASA 36.208 UG) from White Sands Missile Range, New Mexico, on 2003 December 16 at 20:00 MST. The pointing was obtained using an axially mounted onboard startracker with a field of view of $\pm 2°$. Target acquisition was within a few arcminutes of the nominal pointing, and this field was relayed to the ground in real-time through a Xybion TV camera imaging the slitjaw ($20'$ field-of-view). Fine adjustments (e.g. placing the star in the slit) were performed via commands to the ACS in real-time by a ground based operator. γ Cas was placed in the spectrograph slit near T+200 seconds and a 28 second exposure was obtained with the CCD, shown in Figure 2.2. Bias and dark frames were also obtained in-flight. Following the CCD exposure, the MCP high-voltage was turned on and pointing offsets were made to both IC 59 and IC 63. The integration time was sufficiently short on the two nebulae that only a scattered light spectrum of γ Cas was detected at the position of IC 63.

The rocket data were analyzed using IDL code customized to read the data as supplied by the telemetry system. A background subtraction can be made by measuring the flux on the detector adjacent to where the star was located. The data are then calibrated with measurements of the telescope mirror reflectivities and spectrograph quantum efficiencies, measured both before and after flight in the calibration facilities located at The Johns Hopkins University. A more complete description of the instrument and calibration procedures can be found in the Appendix. The high levels of CCD background and fixed pattern noise, combined with a telescope focus problem experienced during flight, prevent a detailed analysis of the stellar spectrum, but the flux calibration can be transferred to *FUSE* LWRS observations of the scattered spectrum of γ Cas described above. Spectral windows with appreciable signal-to-noise in the rocket data were transferred to the *FUSE* spectrum, with the long wavelength end required to match the *IUE* spectrum of γ Cas. This flux-calibrated spectrum of HD 5394, shown in Figure 2.3, is used as the input spectrum for the molecular hydrogen fluorescence model described in Section 2.4.

14
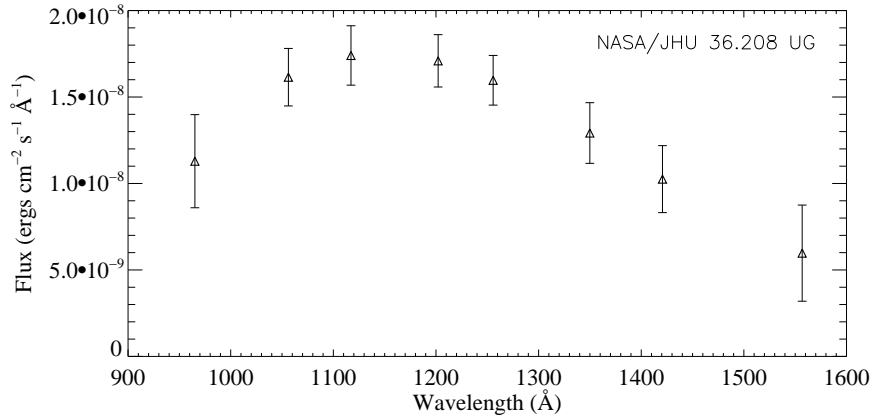
Figure 2.2 Low resolution rocket-borne CCD spectrum of γ Cas. The absolute calibration of this spectrum was used to transfer calibration to the scattered light spectrum obtained by *FUSE*.

2.2.2 *FUSE* Observations

IC 63 was observed by *FUSE* on 2001 September 09 and 10 (see Moos et al. 2000 for a satellite description and Sahnow et al. 2000 for on-orbit performance characteristics). The $(4'' \times 20''$, filled-slit resolving power $R \sim 8000$) MDRS aperture was used to acquire spectra at three positions in the nebula. POS1 was observed for 15.9 ks and is located in the bright "bullet-tip" of IC 63. This position was chosen to overlap with previous pointings made with *IUE*, *ORFEUS*, and HUT where ultraviolet fluorescence was detected (Witt et al. 1989; Hurwitz 1998; this chapter). POS2 is located along the limb of the bright optical emission, and was observed for 17.6 ks (Figure 2.5). POS3, observed for 31.5 ks, samples the region just outside the optical nebula. Sample spectra for all three pointings are shown in Figure 2.4 and a summary of the *FUSE* observations of IC 63 is given in Table 1. The data were obtained in time-tagged (TTAG) mode and have been reprocessed using the CalFUSE pipeline version 3.0.2. In order to minimize channel drift in the LiF2 and the two SiC channels, channel alignment (PEAK-UP) was performed once per orbit using the star HD 6417. *FUSE* data acquired in TTAG mode register the light through all three science apertures (LWRS, MDRS, and HIRS), and while no signal was detected through the HIRS

15
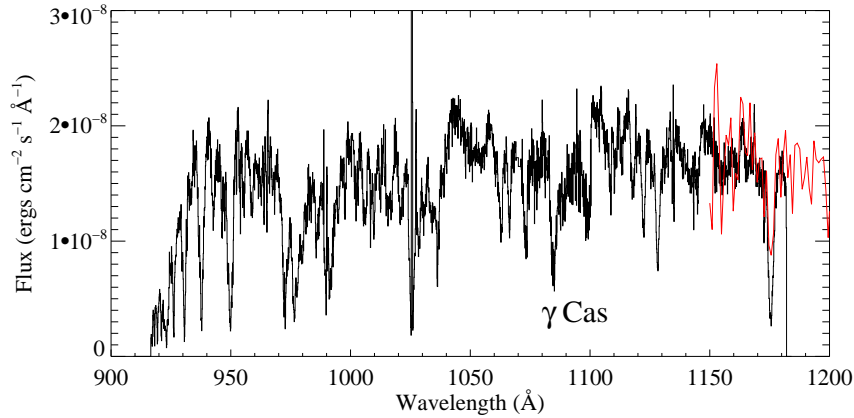
Figure 2.3 The *FUSE* scattered light spectrum of γ Cas (HD 5394) was flux calibrated by comparison with a low resolution rocket-borne spectrograph. The *IUE* spectrum of γ Cas is shown in red in the overlap region. The calibrated *FUSE* spectrum was used as the incident radiation field in the fluorescence model described in the text.

slit, we obtained off-nebula spectra in the LWRS ($30'' \times 30''$) aperture. It was necessary to redefine the regions used for background subtraction by the CalFUSE pipeline in order to accommodate the signal in the LWRS slit. The nominal background regions used by CalFUSE include all regions on the detectors outside of the area of the spectrum from the primary slit. We defined four smaller background regions on the detectors that avoided all three science apertures.

γ Cas exceeds the *FUSE* bright target limit by almost two orders of magnitude, but observing the instrumentally scattered spectrum of the star allows the spectral characteristics to be recorded while protecting the primary science detectors. γ Cas was observed using this offset technique on 2002 December 16 under the *FUSE* project bright-object test program (S52107). During this 3.1 ks observation, the LWRS aperture was located $\sim 1'$ from γ Cas (RA = $00^h 56^m 50.65^s$, δ = $+60° 42' 53.0''$, J2000). Spectra were obtained on the 2A and 2B detector segments, providing wavelength coverage from 916.6 – 1181.9 Å. A flux calibration was performed using the sounding rocket spectrum of γ Cas described in the previous section.

16

Table 2.1. Summary of *FUSE* observations of IC 63.

Position	Program	RA (2000) (^{h} ^{m} ^{s})	δ (2000) ($^\circ$ ′ ″)	Integration Time (seconds)
IC63-POS1	B11201	00 59 01.29	+60 53 17.9	15886
IC63-POS2	B11201	00 58 59.04	+60 53 06.4	17564
IC63-POS3	B11203	00 58 56.79	+60 52 54.9	31509

2.2.3 Description of the HUT Observation

IC 63 was observed by HUT, aboard *Astro*-1, on 1990 December 08. 1668 seconds of nighttime data were obtained in the 830-1880 Å bandpass using the primary ($9.4''\times116''$) aperture (spectrum ic63_144, Figure 2.6). A description of the HUT instrument and data reduction can be found in Davidsen et al. (1992). The spectrum was acquired from the Multi-Mission Archive at the Space Telescope Science Institute (MAST). The pointing is identical to where Witt et al. (1989) detected ultraviolet H_2 fluorescence which is coincident with the *FUSE* POS1.

2.3 Nebular Line Identification

Our *FUSE* observations show a detection of fluorescent H_2 clearly at POS1 and POS2, and there is a tentative detection at POS3. The strongest molecular hydrogen line complexes are centered on 1055, 1100, 1115, and 1161 Å. C II* λ1037 and N II*/N II** λ1085 are seen strongly at all three positions. S III** λ1021 is seen clearly at POS1 and POS3. Interestingly, we do not detect the ground state transitions of C II (λ1036) and S III (λ1012), and only marginally detect N II λ 1084 at POS1 and POS3. C II λ1036, for example, would be expected to be roughly half as strong as the excited C II* line (shown in Figure 2.4), detectable at the S/N of these observations. We attribute this behavior to self-absorption by ground state ions within the nebula. This is supported by the off-nebula spectra simultane-
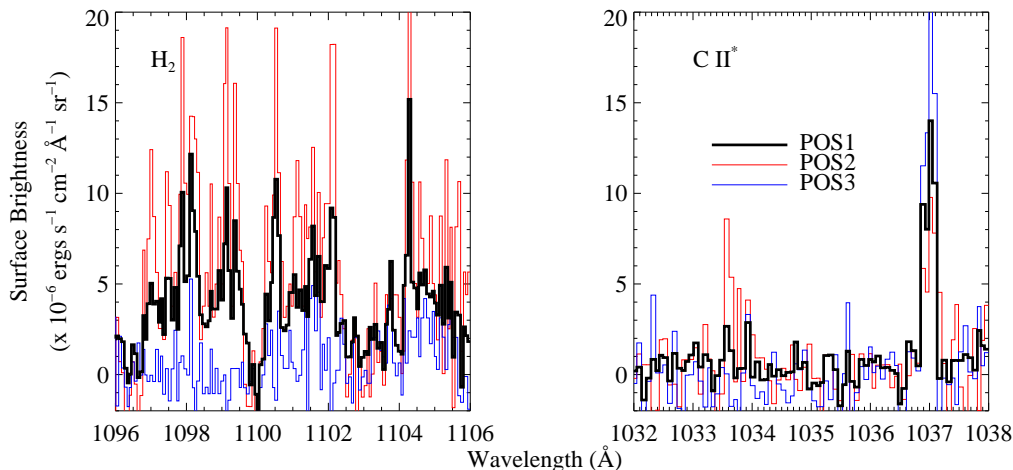
Figure 2.4 Line strengths seen in the *FUSE* spectra vary with position. These two regions are representative of the trends followed by the molecular hydrogen and the ionic species. H_2 shows a peak at POS2 (shown in red), falling to nearly zero at POS3 (shown in blue). The ionic lines, represented here by C II* $\lambda1037$, display the opposite behavior (with the exception of N II** $\lambda1085$). For this comparison, the spectra were shifted to a common background level.

ously acquired in the LWRS aperture. While C II $\lambda1036$ is still undetected, the lower lying transitions of N II ($\lambda1084$) and S III ($\lambda1012$ and $\lambda1015$) are seen. This suggests that the ionized nebula extends beyond both the bright optical emission and the molecular emission, traced by the H_2 fluorescence and the CO maps of Jansen et al. (1994). This picture agrees with the findings of Karr et al. (2005), who find an ionization front in the direction of γ Cas giving way to molecular material (traced by PAH emission) deeper into the nebula.

Line strengths are measured by integrating over wavelength and subtracting the integrated continuum of a nearby region to account for the large uncertainty in the image background subtraction. The ionic and the H_2 line strengths, listed in Table 2.2, display inverse relationships with distance from the *IUE*/HUT position. The ions show a dip in strength at POS2, rising to a maximum at POS3 whereas the molecular hydrogen lines show a peak at POS2, and fall to nearly zero beyond the optical nebula (POS3). The exception to this

Table 2.2.   Line strengths seen in the *FUSE* spectra of IC 63.

Line	λ (Å)	Line Strengths[a]		
		POS1[b] (0″)	POS2 (28″)	POS3 (56″)
H_2	1055	5.2 x 10^{-6}	9.5 x 10^{-6}	~ 0
H_2	1100	3.1 x 10^{-5}	6.3 x 10^{-5}	5.9 x 10^{-6}
C II*	1037	2.8 x 10^{-6}	1.9 x 10^{-6}	4.0 x 10^{-6}
N II	1084	1.8 x 10^{-6}	3.7 x 10^{-7}	7.3 x 10^{-7}
N II*	1085	4.6 x 10^{-6}	4.0 x 10^{-6}	4.1 x 10^{-6}
N II**	1085	9.5 x 10^{-6}	1.0 x 10^{-5}	5.0 x 10^{-6}
P II[c]	962	4.8 x 10^{-6}	1.2 x 10^{-5}	2.5 x 10^{-5}
S III**	1021	1.5 x 10^{-6}	8.5 x 10^{-7}	1.9 x 10^{-6}

[a]In units of ergs s^{-1} cm^{-2} sr^{-1}, errors are estimated to be $\pm$ 25%

[b]Displacements are relative to the HUT pointing in IC 63

[c]Tentative identification

anti-correlation is N II** λ1085, which roughly follows the molecular trend, but does not truncate as sharply as the H_2 at POS3. Errors are difficult to estimate due to the differences in the size and location of the extraction regions used, we conservatively assign errors of $\pm$ 25% to the quoted values. We measure the widths of the ionic lines to be $\sim 0.1 - 0.15$ Å, and find them to be at their rest wavelengths. This is consistent with the $1 - 2$ km s^{-1} velocities found by Karr et al. (2005). We would not expect to measure a wavelength shift at the resolution of the *FUSE* instrument. The molecular hydrogen lines are found to be somewhat broader, as discussed in Section 2.5. Finally, we have found an unidentified triplet feature near 962 Å whose brightness increases in the MDRS aperture from POS1 to POS3. This feature is most likely P II λ961.04/962.12/962.57, however it does not exhibit the spatial variation seen in any of the other species. This feature is not seen in the LWRS aperture, confining its spatial extent to within $\approx 200''$ of the optical nebula.

The strongest nebular feature seen in the HUT spectrum is the λλ1578/1608 H_2 emission. The short-wavelength hydrogen bands are suggested, but are hard to identify unambiguously at the HUT resolution ($\geq$ 3 Å, depending on the filling fraction within the slit). C II λ1335 and N II λ1085 are seen as well a scattered light contribution from nebular dust. The HUT spectrum gives us the opportunity to compare the emission from H_2 both above and below Ly-α, necessary for a thorough test of molecular hydrogen fluorescence models (see §2. 4). The HUT spectrum of IC 63 is shown in Figure 2.6 following a scattered light subtraction similar to the correction described by Witt et al. (1989). The scattered light was assumed to have a form $aF_\star \lambda^\beta$ where $F_\star$ was made from a composite spectrum of γ Cas created from archival *IUE* data and the *FUSE* spectrum described above. The *FUSE* data were degraded to the *IUE* resolution and then joined to created a composite stellar spectrum spanning the entire range ($\approx 900 - 1900$ Å) covered by HUT. Following this procedure, we find that $a = 1.3 \times 10^{-5}$ and β = 1.5.

2.4   Fluorescent Molecular Hydrogen Model

Synthetic spectra of fluorescent emission from molecular hydrogen can be made by computing the radiative excitation rates into the upper electronic states of H_2. Such models

assume a ground electronic state population, then use photoexcitation cross sections and an incident radiation field to calculate the rovibrational levels of the upper electronic state (predominantly $B^1\Sigma_u^+$ and $C^1\Pi_u$). The molecules will then return to the ground electronic state following the appropriate branching ratios, producing the observed ultraviolet emission lines and leaving the molecules in excited rovibrational levels. Sternberg (1989) has described calculations of the far-ultraviolet spectrum of H_2. However, Hurwitz (1998) finds that these models overpredict the observed short-wavelength intensity by roughly an order of magnitude. Such trends are hinted at in the model spectrum of Witt et al. (1989), although it seems that their IUE observations did not go deep enough into the far-ultraviolet to see this effect fully.

We have adopted a modified version of the synthetic molecular hydrogen emission code presented by Wolven et al. (1997) to model fluorescence induced by solar Ly-α at the Shoemaker-Levy 9 impact site on Jupiter. We begin by creating a an electronic ground state population for the molecules. This is done following the formalism of Herzberg to create a matrix of possible energy levels, characterized by their rotational and vibrational quantum numbers, J and v, respectively (Herzberg, 1950). The total energy of a state is given by the sum of the energies from each type of excitation, with E_e, the electronic energy, equal to zero for the ground state. The total energy is then $E_{TOT} = E_{vib} + E_{rot}$. The energy levels can be expressed in terms of their wavenumbers (in units of cm^{-1}), for which vast tables of molecular constants exist. The total energy as expressed in wavenumbers is then

$$
\begin{aligned}
\sigma &= \sigma_e + G + F \\
&\quad \textit{where} \\
G &= \omega_e(v+1/2) - \omega_e x_e(v+1/2)^2 + \cdots \\
F &= B_v J(J+1) - D_v J^2(J+1)^2 + \cdots
\end{aligned}
\tag{2.1}
$$

and σ_e is the wavenember analog to the electronic energy ($= 0$). The ω_e terms above are molecular constants, but the B_v and D_v terms represent a coupling between the rotational and vibrational states. For example, one might imagine a high J-state "stretching" the molecule, producing anharmoninicity in the vibrational potential, or the molecule's moment of inertia changing (and hence it's rotational energy) in an excited vibrational state.

21

To first order, these coupling terms can be expressed as

$$
\begin{aligned}
B_v &= B_e - \alpha_e(v + 1/2) + \cdots \\
D_v &= D_e - \beta_e(v + 1/2) + \cdots
\end{aligned}
\tag{2.2}
$$

where B_e, D_e, α_e, and β_e, are all molecular constants (Herzberg and Huber, 1960). It can be seen then that the energy can be decomposed into terms proportional to J, terms proportional to v, and a cross term that is approximately

$$
\varepsilon_{coupling} = -3(v + 1/2)(J(J+1))
\tag{2.3}
$$

The wavenumber expressions of the energy are then converted back into units of energy (ergs), and an occupation probability of a given rovibrational state, $P(v, J)$, is found multiplying the Boltzmann factor by the degeneracy of a given state. The rotational and vibrational components of the energy are separated and assigned individual temperatures in the Boltzmann factor. The physical basis for separating the rotational and vibrational populations is to mimic the effects of multiple pumping by UV photons. As described in the Chapter 1, the fluorescence process can leave the molecule in an excited vibrational level of the ground electronic state. Since the quadrupole decay rates are comparatively slow, the molecule can absorb another UV photon before it has returned to the ground vibrational state. We simulate this excited vibrational population with the second, higher temperature component. The higher temperature applies only to the distribution of vibrational levels and is not coupled to the population of the rotational states.

Equation 2.3 shows that the decoupling of the rotational and vibrational populations is not strictly complete. In order to understand what complications may arise from this term, a series of tests were run for a range of single temperature models both with and without the coupling term. We found that the coupling term had a negligible effect on the occupation probability for all vibrational states and for rotational states of $J \leq 12$ at temperatures less than the collisional disassociation temperature (≈ 4000 K; Shull and Beckwith, 1982).

Once the ground state population is created, the molecules are "illuminated" by the UV-field described above, and excitation into the upper states are determined by theoretical rates at the Born limit, then re-emit using the calculated emission probabilities of Abgrall

22

et al. (1993a,b). The excitation rate is given by

$$R(vJ \to nv'J') \;=\; I_\lambda \frac{\tau_\lambda^n}{\tau_\lambda} \tag{2.4}$$

where v and J are again the vibrational and rotational quantum numbers of the ground electronic state and v' and J' are the vibrational and rotational quantum numbers of the n excited electronic level. τ_λ is the total optical depth at at a given wavelength, and τ_λ^n is the optical depth for the transition connecting vJ and $nv'J'$. The intensity of radiation being absorbed at a given wavelength, I_λ, is

$$I_\lambda \;=\; I_\lambda^o(1 - e^{-\tau_\lambda}) \tag{2.5}$$

where I^o is the incident radiation field, given by the sounding rocket calibrated *FUSE* spectrum (Figure 2.3) in the case of IC 63.

Following the absorption, the molecules emit following the branching ratios. The emission rate from a particular level of $nv'J'$ to a level $v''J''$ of the ground electronic state is given by

$$S(nv'J' \to v''J'') \;=\; R(nv'J')[1 - \eta(nv'J')]\frac{A_{nv'J' \to v''J''}}{A_{nv'J'}} \tag{2.6}$$

where $R(nv'J')$ is the excitation rate of the excited electronic level, $\eta(nv'J')$ is the efficiency for predissociation in the excited electronic state, and ratio of transition probabilities (A_{nvJ}-values in equation 2.6; Abgrall et al. 1993a,b) is the branching ratio (Liu and Dalgarno, 1996).

The Wolven models differ from those of Sternberg (1989) by including absorption out of upper vibrational states ($v \geq 0$), and a first-order correction for self-absorption by H_2 at wavelengths shorter than 1100 Å. These models also take into account electronic transitions to the B', B'', D, and D' states, although their relative contribution to the resultant spectrum is small. Finally, transitions to predissociating states and vibrational states that result in dissociation ($v'' > 14$, the vibrational continuum) are included. For the model developed for IC 63, we find a dissociation fraction of 16.8%.

There are several important differences between the model described in Wolven et al. (1997) and the one presented here. The first is that we only consider the photo-induced fluorescence, no electron-impact induced contribution is included. Witt et al. (1989), comparing the energy budgets of stellar UV photons, non-thermal electrons produced by the

23

X-ray source associated with γ Cas, and the known stellar wind conclude that only UV photons have the required power to excite the observed H_2 emission. Collisonal processes lack the required energy by several orders of magnitude. Hurwitz (1998) has provided additional evidence against contributions from high-energy electrons, noting that excitation by electrons with energy of $\approx$ 100eV have a steeper short-wavelength slope than that observed.

The solar Ly-α profile that was used as the excitation spectrum in Wolven et al. (1997) has been replaced by the flux calibrated *FUSE* spectrum of γ Cas, described in Section 2.2.2 and shown in Figure 2.3. We only include the 917 – 1182 Å region covered, but with the majority of the upper states populated through absorption between the Lyman limit and the (0 - 0) band near 1110 Å, we expect errors induced by this approximation to be minor.

In addition to the incident radiation field, the model inputs are the two temperatures, the column density (N(H_2)), the Doppler *b*-value (in km s^{-1}, contributing to the line-shape), and a flag that controls the degree of absorption by atomic hydrogen (this value can be converted into a molecular fraction). The two temperature components used to model the fluorescence in IC 63 were chosen from the literature and an empirical analysis of the HUT spectrum. The rotational temperature was taken from Habart et al. (2004), 620 K, and a higher "non-thermal" vibrational temperature of 2500 K that was required to find agreement with the HUT data. The feature near 1578 Å that is produced in transitions to the vibrational continuum of the ground electronic state was underpredicted without a high-temperature component (Figure 2.6).

We adopted a Doppler *b*-value of 2 km s^{-1}. Sub-mm molecular line widths are seen to be quite narrow (Jansen et al., 1994; Hurwitz, 1998), and 2 km s^{-1} is the smallest *b*-value that is compatible with the H_2ools optical depth templates described by McCandliss (2003). The model is largely insensitive to the actual choice of *b*-value for values of a few km s^{-1}. The ratio of atomic to molecular hydrogen column densities is fixed to be 0.1 for our analysis of IC 63, extrapolating the values found in the translucent cloud survey of Rachford et al. (2002).

We also use the column density from Habart et al. (2004; 5×10^{21} cm^{-2}) in the fluorescence code. We found that the model required an additional molecular hydrogen absorption component (of the same column and *b*-value used in the emission model) to

agree with the HUT data at the 1100 Å H_2 emission band. This additional absorption component was calculated using the *H_2ools* templates (McCandliss, 2003). The *FUSE* spectra are better fit without this added absorption. As the bulk of the H_2 emission seen in the HUT data is unaffected by this additional absorption component, it is difficult to assign the a level of significance to this result, especially given the uncertainties discussed below. Assuming that the interstellar extinction along the line of sight to IC 63 is small, as is the case for γ Cas, we do not include a reddening correction.

2.5   Discussion

2.5.1   Spatial Extent of the IC 63 Fluorescing Region

We can gain an estimate of the size of the region from which the H_2 fluorescence emanates by comparing the line fluxes observed by *FUSE*, *ORFEUS* and HUT. The slit areas of these three instruments were 80, 530 & $1090''^2$, respectively. Based on the MAST archival spectra we find that the integrated fluxes for the line complexes at $\sim$1055Å and $\sim$1100Å we find the the fluxes observed by *ORFEUS* and HUT are consistent with each other at $\sim$2 and 3×10^{-13} ergs s^{-1} cm^{-2}, respectively. The same two regions yield integrated fluxes of $\sim$5 and 7×10^{-14} ergs s^{-1} cm^{-2} in the *FUSE* observations. Although such a comparison is complicated by the fact that the slit geometries differ, with *FUSE* and HUT having rectangular slits while *ORFEUS* employed a circular slit, we find that the region giving rise to the H_2 fluorescence extends beyond the area of the *FUSE* MDRS slit, but does not fill the HUT or *ORFEUS* slits. If we assume that the emitting region is of uniform surface brightness, we can use the flux ratios to estimate that the *ORFEUS* slit was about 60 % filled. As the emission seen by *FUSE* towards POS2 is of similar strength as POS1 we conclude that the center of the emitting region is probably located between these two positions. If we assume that the emitting region is a circle, centered between our POS1 and 2, we can then estimate that the diameter of the emitting region is about $30''$.
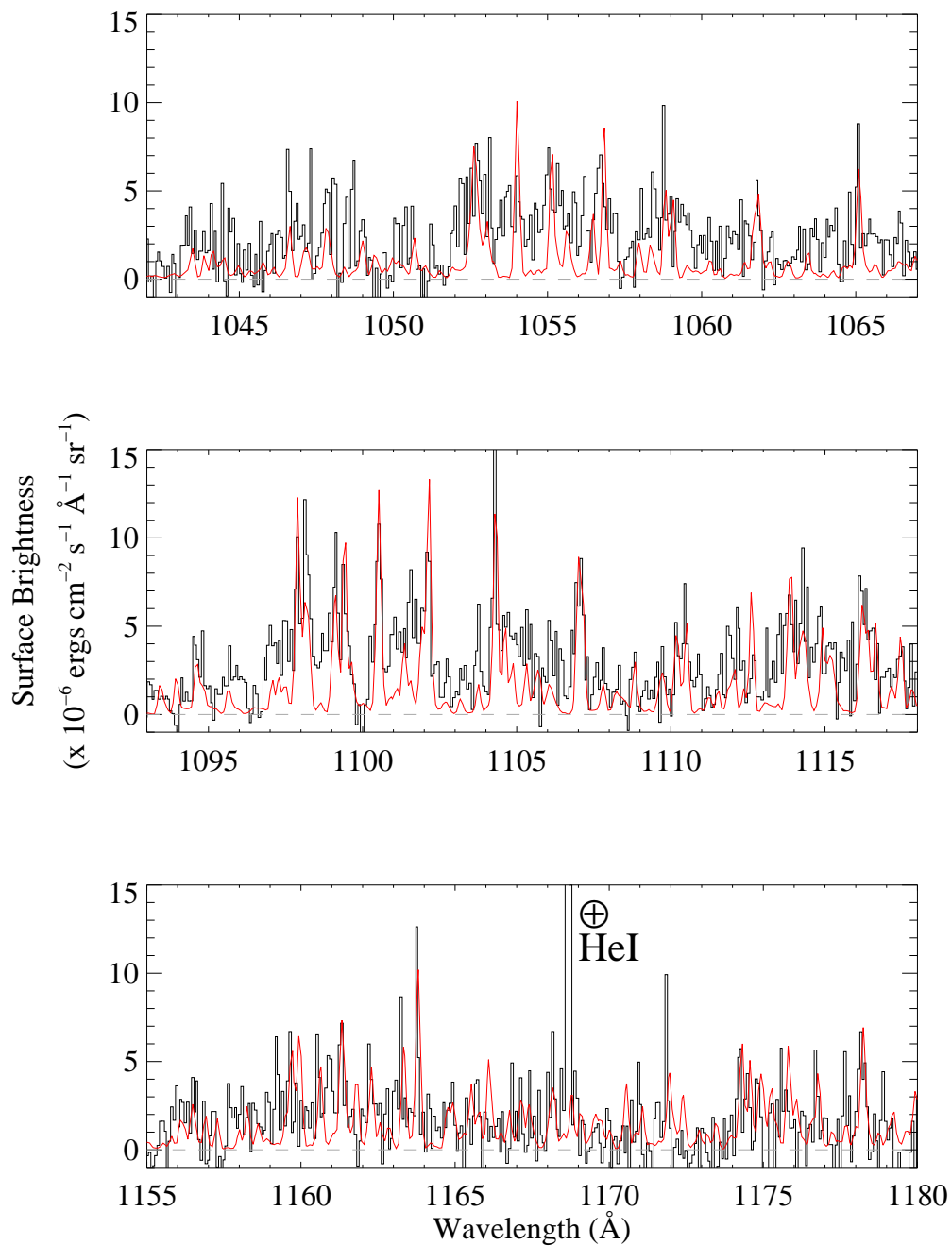
Figure 2.5 25 Å windows of the *FUSE* spectra of POS2 overplotted with the H_2 emission model described in §4. The model spectrum has been convolved to 0.15 Å. These spectra were acquired in the LiF 1a and LiF 2a channels.
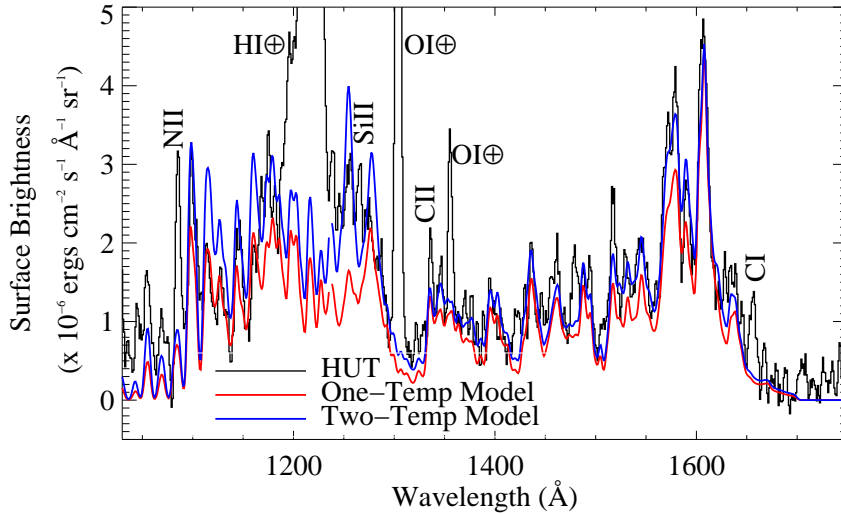
Figure 2.6 The HUT spectrum of IC 63 following a scattered light subtraction of the form $aF_\star\lambda^\beta$, as described in the text. The molecular hydrogen fluorescence models described in the text have been convolved to a resolution of 4 Å. A single temperature model (620 K) is shown in red to demonstrate the need for two temperature components (620 + 2500 K), plotted in blue. Nebular atomic emission lines are labeled.

2.5.2 H_2 Modeling Results; IC 63

Figures 2.5 and 2.6 show a comparison of the nebular H_2 emission spectrum with the model described above. The HUT data allow us to test this model both above and below Lyman-α for the first time while the *FUSE* spectrum gives us the opportunity to study the short wavelength H_2 spectrum in detail. In each instance, the model requires an offset in the absolute flux to agree with the observations. Our H_2 model is seen to roughly fit the spectrum of IC 63 both below Ly-α and at the longest ultraviolet wavelengths (~ 1600 Å), resolving the order of magnitude discrepancy between the relative strengths of the ultraviolet emission components seen in Hurwitz (1998) and suggested in the spectrum presented by Witt et al. (1989). Our model still shows some deviation at short wavelengths, but the differences are a factor of two at the most. H_2 emission in the 1115 and 1143 Å bands are better fit with the single temperature model, shown in red in Figure 2.6, despite the

27

underprediction of this model elsewhere in the spectrum. Disagreement between the model and the data could be due to an imperfect scattered light subtraction and/or an unknown amount of interstellar extinction. To achieve the fit to the HUT spectrum, the model requires an overall scale factor of 11, yet this is probably an underrepresentation of the actual scaling required because the molecular emission is unlikely to be filling the entire HUT aperture (§ 2.5.1).

We find that the model shows relatively good agreement with the strengths of the rotationally resolved lines in the *FUSE* data. The lines appear broader than would be expected from a purely instrumental effect. We expect a filled-slit resolution of ≈ 0.125 Å in the MDRS aperture, yet some H_2 lines are broader than 0.25 Å. We tentatively explain this as a redistribution effect caused by coherent scattering in the damping wings of the absorbing transition (Hummer, 1962). The exact cause is beyond the scope of this thesis and will be addressed in future work. In contrast to the HUT spectrum, where the model needed to be scaled up to fit the data, we find that in order to achieve a good fit to the H_2 lines observed in the *FUSE* spectra, the model needs to be scaled down by a factor of 0.5. One possible explanation for the variations we find in the scaling needed to reach agreement between the model and the different data sets could be the clumpy nature of the molecular gas in IC 63. Recent work has found that molecular gas and dust tend to form dense knots in the presence of an intense ultraviolet radiation field (O'Dell, 2000; Huggins et al., 2002; France et al., 2004). If we assume that such knots exist in IC 63, then the $30''$ emitting region may be composed of dense clumps instead of smoothly distributed molecular gas. This could reconcile the scaling we require to bring our model into agreement with the data. The larger HUT aperture may have included several of these dense clumps, whereas the smaller *FUSE* MDRS aperture may have picked up fewer, or simply missed the brightest of these knots. Differing contributions from dense regions in IC 63 could explain the different scale factors needed to predict the absolute flux seen in the nebular spectra.

The two strongest arguments for these models being an improvement over what was presented in Sternberg (1989) is the relative agreement across the far-UV bandpass and the satisfactory qualitative agreement with the rotational structure seen in the *FUSE* data. The differences between the models presented in this chapter and those of Sternberg (1989) can be attributed to four primary factors: the self-absorption correction, considering molecular

dissociation, considering multiple pumping, and the use of a realistic incident radiation field. The self-absorption correction suppresses the flux at short wavelengths, alleviating the large discreperancy seen in the models of Sternberg (1989). Including the possiblilty of dissociation predicts the $\lambda 1578$ line complex (absent in the Sternberg, 1989 models) and including the effects of multiple pumping allows us to accurately predict the strength of it and other bands. Finally, using the excitation spectrum of γ Cas itself enables us to explore which individual lines are absent due to a lack of the necessary exciting transition (caused by photospheric and/or intervening absorption).

2.6 Summary of Chapter 2

This chapter has presented far-ultraviolet spectroscopy of the emission/reflection nebula IC 63. The MDRS aperture on $FUSE$ was used to obtain high-resolution spectra of three positions within the nebula across the 912 – 1187 Å bandpass. These data were complemented by an archival HUT spectrum of IC 63 at lower resolution, extending the wavelength coverage to beyond 1700 Å. These data confirm the presence of a population of fluorescing H_2 seen in previous studies. Models of this emission have been shown to overpredict the relative strength of the shortest wavelength lines by as much as an order of magnitude. We use these data to develop a model that not only accurately describes the detailed rotational structure of the emission lines, but resolves the perceived discrepancy between the shortest and longest ultraviolet wavelengths spanned by H_2. This model incorporates a realistic incident radiation field by using sounding rocket observations to calibrate a $FUSE$ scattered light spectrum of the exciting star, γ Cas. Our model finds satisfactory agreement with the spectral structure seen with $FUSE$ and finds relative consistency at all wavelengths. Our model still does not predict the correct absolute flux that is observed, and the emission lines in the $FUSE$ spectra are broader than what would be expected from instrumental effects alone. This effect can be seen more strongly in the following chapters, and possible physical explanations are described in more detail in chapters 5 and 6.

Chapter 3

Molecular Hydrogen in Orion as Observed by the *Far Ultraviolet Spectroscopic Explorer*

> *"Don't look to rockets for salvation-"*   – Kurt Vonnegut

3.1   Introduction to the Orion Nebula

The Orion Nebula (M42) is among the most well-studied objects in the sky. Its proximity to the Sun combined with a bright Photo-Dissociation Region (PDR) and a giant molecular cloud make it an ideal region to study a range of astrophysical processes. Molecular hydrogen (H_2) should account for the majority of the molecular mass in this region. Previous observations of H_2 emission in Orion have been limited to the weak quadrupole rovibrational transitions arising in the near and mid-infrared (IR; see references above as well as Habart et al. 2004). In this chapter, we present an analysis of the first far-ultraviolet fluorescent emission spectra of the electronic transitions of H_2 in Orion, obtained by the *Far Ultraviolet Spectroscopic Explorer* (*FUSE*). These spectra have been presented by Murthy et al. (2005), in work focusing on the dust scattering properties of the region. The spectra show a dust scattered continuum, onto which absorption and emission features of H_2 are identified.

The excitation mechanism of the near-IR lines of H_2 has long been a point of disagreement. Numerous authors have argued for excitation by either shock processes or UV fluorescence. In a gas-rich region that contains outflows from young stars and an intense ultraviolet radiation field produced by O and B stars, it seems likely that multiple processes are at work. Near-IR observations of H_2 in Orion have been used to distinguish which of these excitation mechanisms are consistent with the observed emission (Luhman et al., 1994; Kristensen et al., 2003). These *FUSE* observations do not rule out the possibility of a contribution from shocks, however they provide solid evidence for UV fluorescence in Orion.

In §3.2, we present the *FUSE* data obtained during a serendipitous pointing equilibration observation (see Murthy et al. (2005) for a comprehensive description of the observations). Murthy et al. (2005) find that the dust scattered light is dominated by the intense radiation field of θ^1 Ori C (HD 37022; O6V Maiz-Apellaniz et al. 2004), despite the small angular separation of the observed field from HD 36981 (B5V). Given its intense far-UV output, θ^1 Ori C is likely to be the dominant source of excitation for the H_2 emission observed in Orion. A model of the H_2 fluorescence, using the unattenuated continuum of θ^1 Ori C as the excitation source, is described in §3.3; that model is compared to the observations in §3.4. These observations provide evidence that UV excitation gives rise to the observed near-IR emission lines in the Orion Nebula region, in agreement with the findings of Luhman et al. (1994).

3.2   *FUSE* Observations of M 42

The diffuse region of the Orion Nebula located at RA = $05^h35^m12.43^s$, δ = -05° 11′35.3″, J2000, was observed by *FUSE* for 16.7 ks in time-tagged (TTAG) mode on 2001 November 26 as part of the S405 channel realignment program described by Murthy and Sahnow (2004) and Murthy et al. (2005). Nebular spectra were acquired across the *FUSE* bandpass (905 – 1187 Å) in the (30″ × 30″) LWRS aperture (Figure 3.1). The spectra were obtained from the Multi-Mission Archive at STScI (MAST), and were analyzed with the original CalFUSE calibration (version 1.8.7). The calibrated data files for each orbit were
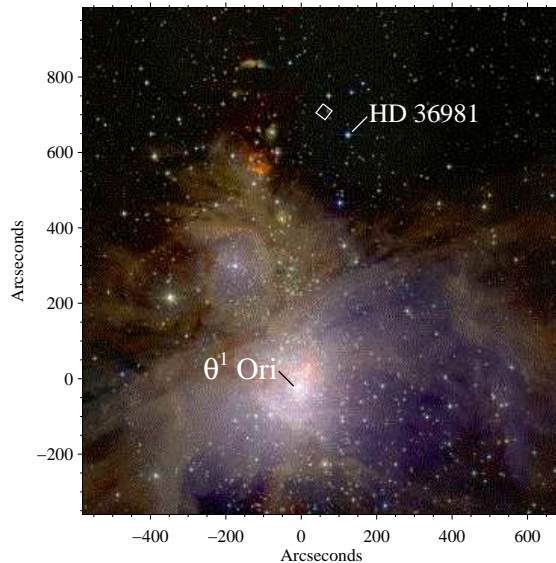
Figure 3.1 2MASS Atlas image of the Orion Nebula, M42. θ^1 Ori is at the origin and the *FUSE* LWRS aperture overlay is shown at the upper right near HD 36981. The pointing was determined from an alignment of the FES image with the target field. Atlas Image mosaic obtained as part of the Two Micron All Sky Survey, a joint project of the University of Massachusetts and the Infrared Processing and Analysis Center/California Institute of Technology, funded by the National Aeronautics and Space Administration and the National Science Foundation.

then coadded using IDL software and the individual channels were combined using a cross-correlation algorithm. The exact pointing was determined by comparing Fine Error Sensor (FES) images with images generated by sky simulator software.

This chapter presents the S4054601 spectra at wavelengths longer than Ly-β (Figure 3.2), where the bulk of the far-UV emission from H_2 resides. In addition to the numerous absorption lines coming from molecular hydrogen discussed below, we see the scattered photospheric lines from C III λ977/1176, P V λ1118/1128, and Si IV λ1122/1128, as well as interstellar absorption from C II λ1036 and N I λ1135. These features are identified in Figure 2. The fact that the P V λ1118 line was seen in the spectrum is probably the

most conclusive argument for θ^1 Ori C (as opposed to HD 36981) illuminating this region of Orion. Atomic hydrogen lines are highly contaminated by the interstellar medium and Pellerin et al. (2002) find that P V is not present in stars of spectral type later than B2V. Finally, we find an unidentified absorption feature at 1031.4 Å that we tentatively assign to blue-shifted O VI. Blue-shifted O VI absorption is seen in many stars of of this spectral type (Pellerin et al., 2002), however we cannot conclusively identify it as the $\lambda 1038$ component of the doublet falls in a region dominated by H_2 and C II absorption.

3.3 Modeling Molecular Hydrogen in Orion

The ultraviolet absorption and emission features of H_2 observed in Orion are seen superimposed on the dust scattered continuum of θ^1 Ori C (Murthy et al., 2005). A model of the nebular dust-scattering continuum is beyond the scope of this work, but we set the baseline for the molecular hydrogen by fitting the continuum with a double power-law of the form

$$S(\lambda) \;=\; (\frac{\lambda}{\lambda_0})^\alpha \;-\; C(\frac{\lambda - \lambda_0}{\lambda_0})^\beta \tag{3.1}$$

scaled to the data. This simple empirical fit with λ_0 of 1187 Å, yields $\alpha = 0.1$, $\beta = 2.0$, and $C = 5.0$. An H_2 absorption spectrum was calculated using the H_2ools optical depth templates (McCandliss, 2003). As the Doppler b-value of is uncertain, we have adopted 2 km s^{-1} for this diffuse region, consistent with b-values observed along the line of sight to other stars in this region of Orion (Spitzer et al., 1974; Jenkins and Peimbert, 1997). With that assumption, we used the templates to fit the (4 - 0) band ($\lambda \approx 1050$ Å) and find a total $N(H_2) = 4.7 \times 10^{18}$ cm^{-2}. Absorption out of the ground electro-vibrational state for the first six rotational states was considered, but most of the absorption comes from $J = 0$ and 1. Because the absoption lines are partially filled in by the fluorescent emission (see below), the true $N(H_2)$ for this line of sight is most likely greater than 4.7×10^{18} cm^{-2}. This level of H_2 absorption is surprising, studies of stars in this region find a very low molecular fraction in the intervening gas (Abel et al. 2004 and references therein).

We fit the emission spectrum of H_2 seen in these *FUSE* data using the hydrogen fluorescence model described in Chapter 2. The model uses parameters for the Orion region

found in the literature for $N(H_2)$ and temperature. Kristensen et al. (2003) imaged regions of the Orion Nebula in the near-IR rovibrational lines of H_2 to determine the excitation temperature. They find a clear delineation between hot and cold zones, requiring more than one temperature component to produce a reasonable fit to the observations. We therefore adopted the rotational temperature of 390 K from Habart et al. (2004) as the cool (thermal) component and a vibrational temperature of 2500 K as representative of the hot (shocked or non-thermal) component (Chapter 2). An $N(H_2) = 1 \times 10^{21}$ cm^{-2} (Habart et al., 2004) was used with a b-value of 2 km s^{-1}. Each of these parameters affects the resultant model spectrum differently. The model spectra change very little with b for values of a few km s^{-1}. Varying the column density changes the total emitted power, higher density giving more output photons, but self-absorption begins to surpress discrete lines at columns greater than $\sim 5 \times 10^{21}$ cm^{-2}. Temperature controls both the shape and scale of the model spectra, more levels of the ground electronic state are populated at higher temperatures.

Radiation from θ^1 Ori C dominates the ambient field in this part of Orion (Murthy et al., 2005). It is most likely responsible for pumping the observed fluorescence, and should thus be used as the input field for modeling the H_2 emission. This is complicated by two factors: 1) a well flux-calibrated far-UV spectrum of θ^1 Ori C does not exist and 2) the majority of the absorption seen on the HD 37022 line of sight is thought to be located in intervening clouds (Bautista et al., 1995; Murthy et al., 2005). A spectrum of θ^1 Ori C as observed from Earth will not be representative of that seen by the molecules in Orion. In an attempt to overcome these concerns, we chose a lightly reddened SMC star of similar spectral type (AV 243, O6V, $E_{B-V} = 0.09$) from the *FUSE* Magellenic Cloud Atlas of Danforth et al (2002; see also Walborn et al. 2002). A simple correction for the differences between Milky Way and SMC dust was made using the computed extinction curves of Weingartner and Draine (2001), assuming the reddening of θ^1 Ori C at the *FUSE* pointing is similar to what is observed along the HD 36981 sightline ($E_{B-V} = 0.04$). We assumed that the reddening on the AV 243 line of sight was due to equal contributions from Milky Way and SMC dust. An *IUE* spectrum of θ^1 Ori C (swp01394, also obtained from MAST; Bohlin & Savage 1981) was used to cross-calibrate the surrogate *FUSE* spectrum in the overlap region between 1150 and 1187 Å. Primary uncertainties in this approach
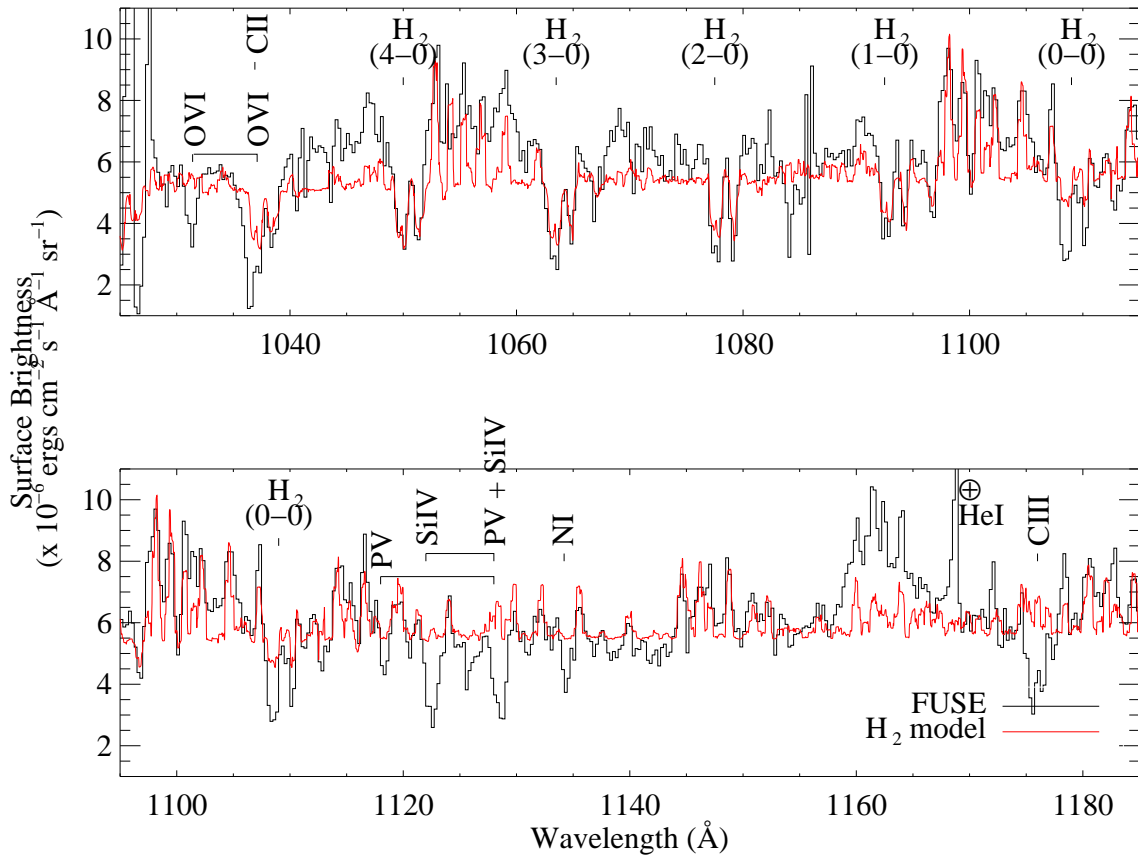
Figure 3.2 The *FUSE* spectrum described in the text overplotted with the H_2 emission model described in §3.3. The model spectrum has been convolved to a resolution of 0.5 Å. H_2 lines are the dominant features seen in both absorption and emission between Ly-β and the end of the *FUSE* bandpass. C II and N I are of interstellar origin. The longest wavelength H_2 absorption strengths are underpredicted due to an offsetting contribution from the emission lines, as described in § 4.

36

are a lack of knowledge about the attenuation between the star and the nebula, the actual contribution from SMC and Milky Way dust, and possible calibration problems with the *IUE* spectrum (Massa and Fitzpatrick, 2000). Using this incident radiation field and the parameters described above, we constructed the fluorescence spectrum (convolved with a 0.5 Å box kernel) for comparison with the data.

3.4 Discussion

The nebular spectra and the model described above are shown in Figure 3.2. The model finds satisfactory qualitative agreement with the relative line strengths seen in the *FUSE* spectra between Ly-β and the end of the bandpass. We find effects similar to those seen in far-UV spectra of the emission/reflection nebula IC 63, namely that the observed H_2 emission lines are seen to be broader than what is expected from the instrumental profile for these filled aperture observations Chapter 2. A study of the possible mechanisms that would produce this broadening is underway. The two major discrepancies that we find between the data and the relative strengths predicted by the model are in the region between 1040 – 1050 Å, and the band of lines centered on 1161 Å. The 1040 –1050 region may be contaminated by broad wind emission from O VI, θ^1 Ori C also shows an "excess" in this range (Murthy et al., 2005), but the exact cause is uncertain. The 1161 band seems to be sitting on a "shelf" that is not predicted by the model. One hypothesis that we explored was the possibility of hot H_2 (T $\geq$ 2500 K) being fluoresced by nebular Ly-α, as is seen in the far-UV spectra of pre-main-sequence stars (Wilkinson et al., 2002) and accreting binary systems (Wood and Karovska, 2004). In order to test this theory, we added a linear continuum that extended the excitation spectrum to 1300 Å and a Gaussian emission line at Ly-α. This additional excitation out of excited states of H_2 does not resolve our problem with the 1161 band. We find that as the 1161 band begins to fill in that numerous other lines are predicted that we do not observe in the *FUSE* spectra. The most likely conclusion is that our model is lacking some physical mechanism that gives rise to these features.

The model does not agree with the observed absolute flux. We find that in order to correctly predict the observed absolute flux, our model output needs to be scaled up by

a factor of two. We attribute this to three possible causes: 1) an uncertainty in the degree of H_2 clumping in this region, 2) an uncertainty of the true strength of the exciting radiation field, and 3) a similar piece of physics that causes discrepancies at 1045 and 1161 Å is missing from our model. Dust and molecular hydrogen are known to be found in clumpy and/or filamentary structures in regions where hot stars interact with their surroundings (O'Dell, 2000; Kristensen et al., 2003; France et al., 2004), however we find this explanation unlikely. Creating similar models at higher column densities shows that while the overall emitted power increases with column, the majority of this extra emission is located outside of the $FUSE$ bandpass ($\lambda \geq 1200$ Å). The second possibility is that our input excitation field does not accurately represent the local absolute radiation field. We feel confident that the spectral characteristics of the input spectrum are good based on the relative agreement with the H_2 emission spectrum, but are less confident in the absolute scale. Changes in our reddening assumptions, absolute calibration of the IUE spectrum we used (Massa and Fitzpatrick, 2000), and uncertainties in the nebular distance/geometry can easily explain the scaling required. Finally, further modeling efforts are underway to resolve the problems described above.

The molecular hydrogen absorption lines present in the spectra also show an interesting behavior. One would expect, based on the decreasing oscillator strengths as a function of decreasing upper vibrational quantum number (Abgrall et al 1993a,b), that the lines would be shallower during the progression to smaller vibrational transitions ($4-0$ to $0-0$, shown in Figure 3.2). We find that the absorption profiles are of almost identical depth in each of the bands. We attribute this to a filling effect by the emission from H_2 where the emitting and absorbing transitions overlap. There are a greater number of emitting transitions overlapping with the absorption lines at shorter wavelengths, so fitting the absorption lines at the $(4-0)$ band leads to an under prediction of the strength of the lines in the longer wavelength bands of molecular hydrogen. This finding leads us to stress that meaningful column densities cannot be determined without correcting for the emission lines and properly addressing the dust scattering to set the continuum level.

There has been uncertainty in the degree to which shocks or ultraviolet photo-excitation leads to the observed near-IR lines of molecular hydrogen seen in Orion (Burton et al., 1989; Luhman et al., 1994; Kristensen et al., 2003). These $FUSE$ data rule out models that

consider only shocks as the mechanism producing the near-IR emission. Shocks cannot populate the excited electronic states of molecular hydrogen that give rise to the emission lines seen (Shull and Beckwith, 1982). Hydrogen molecules will be dissociated by collisions at temperatures greater than roughly 4000 K, thus they would be destroyed before reaching temperatures sufficient to begin populating the first excited electronic state, $B^1\Sigma_u^+$ (E $\approx$ 11 eV). These data cannot exclude shocks from making a contribution to the near-IR H_2 emission (Kristensen et al., 2003), but ultraviolet excitation clearly contributes to the rovibrationally excited population of hydrogen molecules in the Orion Nebula.

Chapter 4

Rocket and *FUSE* Observations of IC 405: Differential Extinction and Fluorescent Molecular Hydrogen

> *"I know it sounds nuts, but hey, you've read the first half of the book."*   – Michael J. Fox

4.1 Introduction to IC 405

As described in the Introduction to this dissertation, observations aimed at determining the far-ultraviolet properties of dust grains are challenging as they require space-borne instrumentation designed specifically for such studies. The lack of data has hampered testing models of interstellar dust grains in the far-ultraviolet (far-UV) spectral region below Lyman-α where dust most strongly attenuates the radiation field. Constraints can be placed on the physical properties of dust grains by studying how they absorb and scatter far-UV light where the two interact, either near a bright source of ultraviolet photons or in the diffuse interstellar medium. Reflection nebulae have been used by a number of observers in an attempt to derive the properties of grains (see Draine 2003a for a recent review). The interpretation of these observations is complicated by geometric uncertainties in the nebular dust distribution, contamination by emission from atomic and molecular species within

the nebula, and uncertainties in the incident spectral energy distribution (Witt et al., 1993; Burgh et al., 2002; Hurwitz, 1998). Burgh et al. (2002) have made the first measurement of the dust albedo (a) and phase function asymmetry parameter ($g \equiv \langle \cos \theta \rangle$) below Ly-$\alpha$, using long-slit spectroscopy to constrain both quantities. However, Mathis et al. (2002) have argued that observations of reflection nebulae are so confused by the clumpy nature of the dust distributions that the derived grain properties are highly unreliable. To further address this problem, we present far-UV observations of IC 405. IC 405 (The Flaming Star Nebula) is an emission/reflection (Herbig, 1999) nebula in Auriga, illuminated by a dominant star, AE Aur (HD 34078). AE Aur is one of the stars thought to have been ejected from the Orion region roughly 2.5 million years ago in a binary-binary interaction that led to the creation of the well studied ι Ori binary system (Bagnuolo et al., 2001). Consequently, AE Aur is moving with a large proper motion through the nebula at ≈ 40 milliarcseconds yr^{-1} (Blaauw and Morgan, 1954). Herbig (1999) used repeated observations of this high proper motion object to search for interstellar line variations, providing information about clump structure in the ISM .

Presently, AE Aur is thought to be cospatial with the nebula at a distance of about 450 pc. It is bright in both the visible (V = 6.0) and the ultraviolet (O9.5 Ve), although it is rather extinguished ($E(B - V) = 0.53$ and $R_V = 3.42$; Cardelli, Clayton, & Mathis 1989). In this chapter, we present far-UV observations of IC 405 made with a rocket-borne long-slit spectrograph and the *Far Ultraviolet Spectroscopic Explorer* (*FUSE*). Figure 4.1 shows the nebula with the various spectrograph apertures overlaid. Section 4.2 includes a description of the rocket experiment, the observations, and the data reduction. In § 4.3, we describe the *FUSE* observations and reduction. Section 4.4 puts the IC 405 data in context with previous studies of other reflection nebulae, including discussion and interpretation of the results and their possible consequences. Our observations of IC 405 are summarized in § 4.5.
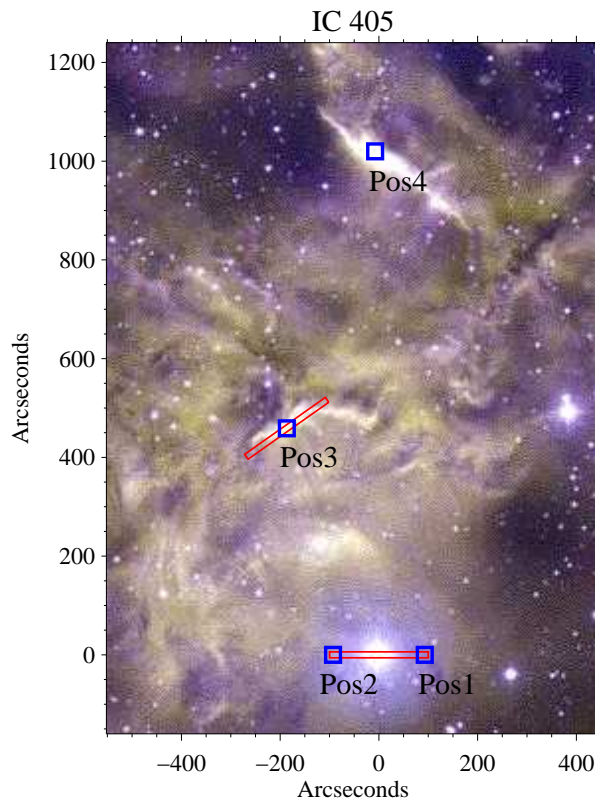
Figure 4.1 IC 405 with the relevant aperture overlays, HD 34078 is located at the origin. The long slits represent the aperture of the rocket spectrograph, and the boxes represent the *FUSE* LWRS aperture. Optical image from *APOD*, T.A.Rector and B.A.Wolpa/NOAO/AURA/NSF.

4.2 Rocket Observations of IC 405

Long-slit spectroscopy is a technique that lends itself to the study of reflection nebulae where the exciting star(s) typically are embedded in or near the gas and dust with which they are interacting. The extended aperture allows nebular spectra to be measured continuously along the slit, and variations can be observed in both wavelength and angle from the central object. This information can also be obtained through small apertures, but this

requires multiple observations, which is costly in the far-UV bandpass where observing time is at a premium.

4.2.1 Instrument Description and Observations

The sounding rocket experiment consists of a telescope and spectrograph designed for use in the far-UV. The telescope is an updated version of the Faint Object Telescope (FOT), a 40 cm diameter, f/15.7 Dall-Kirkham (Hartig et al., 1980; McCandliss et al., 1994; Burgh et al., 2002). The optics are coated with a layer of ion-beam sputtered SiC to enhance the reflectivity at far-UV wavelengths. The telescope is housed in an invar heat-shield with a co-axially mounted startracker which provides error signals to the Attitude Control System (ACS).
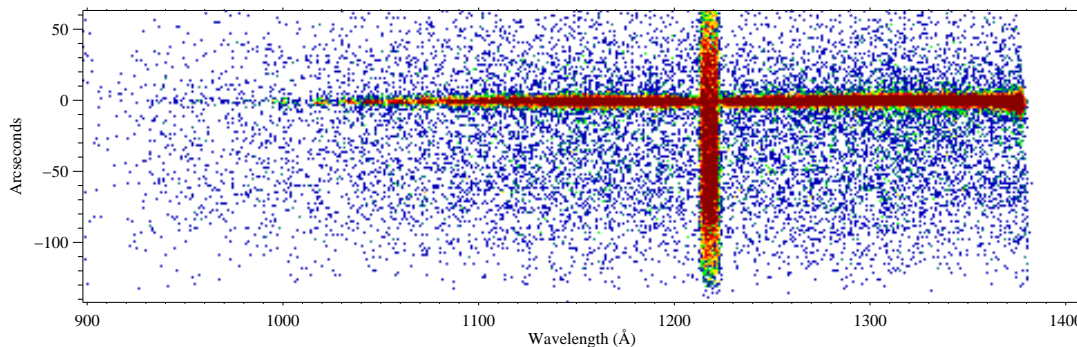
Figure 4.2 The spectrogram of the rocket data, following time-tagged correction for pointing. HD 34078 is the horizontal strip, the nebular spectra are above and below the star, and the broad vertical feature is geocoronal Ly-α.

The FOT focuses the target at the entrance aperture of the instrument, an evacuated 400 mm diameter Rowland Circle spectrograph (the predecessor to the LIDOS instrument described in Chapter 2) using a holographically ruled, SiC coated, diffraction grating in the first order. The detector is a microchannel plate stack with a KBr photocathode, read out by a double delay-line anode (Siegmund et al., 1993). The spectrograph is kept at a vacuum of $\approx 10^{-8}$ Torr and isolated from the spectrograph section by a gate valve that opens under

timer control in flight. The spectrograph and telescope sections share a common vacuum ($<$ few $\times$ 10^{-5} Torr). A mirrored slitjaw, angled $22°$ from the optical axis, lies at the telescope focus. A long slit ($12''\times 200''$ projected on the sky, 5.6×10^{-8} sr) is etched into the slitjaw, defining the entrance aperture to the spectrograph. The spectrograph achieves a pointing limited spectral resolution of ≈ 3 Å. A more complete description can be found in the Appendix.

This experiment was launched aboard a Black Brant IX sounding rocket (NASA/JHU 36.198 UG) from White Sands Missile Range, New Mexico ($106°3$ West, $32°4$ North), on 09 February 2001 at 21:00 MST. The target was obtained by referencing the startracker to two bright guide stars (Sirius and Capella), then reorienting to the target. The acquired field is within a few arcminutes of the expected pointing. The field is relayed to the ground in real-time through a Xybion TV camera imaging the slitjaw ($20'$ field-of-view). Fine adjustments are performed in real-time via commands to the ACS. HD 34078 was placed in the spectrograph slit at T+150 seconds and data was taken continuously until detector high-voltage turn-off at T+490 seconds. The stellar spectrum was recorded for 106.2 seconds of the flight (hereafter the "on-star" pointing). Two offset pointings within the nebula were observed with only one having a count rate higher than the background (observed for 68.7 seconds, hereafter the "off-star" pointing). Figure 4.2 shows the pointing corrected long-slit spectrogram of the data obtained from target acquisition to detector turn-off.

4.2.2 Analysis of the Rocket Observations

Flight data were analyzed using IDL code customized to read the data as supplied by the telemetry system. A background subtraction can be made by measuring the flux on the detector after instrument turn-on, but prior to target acquisition. The primary source of background flux is geocoronal airglow from atomic hydrogen and oxygen. The data are then calibrated with measurements of the telescope mirror reflectivities and spectrograph quantum efficiency, measured both before and after flight in the calibration facilities located at The Johns Hopkins University. Calibration procedures are described in more detail in the Appendix.

The stellar spectrum is extracted following corrections for pointing errors and detec-

tor drift. Figure 4.3 shows the spectrum of the HD 34078 obtained during the flight. The spectrum is of high quality (S/N ≈ 10-15 at $R = 300$), and is consistent with previous far-UV measurements (*IUE*; Penny et al. 1996 and *FUSE*; Le Petite et al. 2001). In Figure 4.3, the measured spectrum has been shown overplotted with a synthetic stellar spectrum. The model has been extinguished using the parametrization of Fitzpatrick anbd Massa (1990, see §4.4.4) and the H_2ools molecular hydrogen absorption templates (Mc-Candliss, 2003) for a $b = 3$, as determined by Le Petite et al. (2001), and a total column density $N(H_2) = 8.1 \times 10^{20}$ cm^{-2}, that we determined from the *FUSE* spectrum of the star, described below. The stellar spectrum shows interstellar absorption features of H I, H_2, C II, and O I and photospheric C III absorption. After the star is removed, the spectra from different regions within the nebula can be separated by "time-tagging" the data from a playback of the slitjaw camera that shows the flight time. Integrating the nebular spectra over the area of the slit allows one to measure the nebular surface brightness. Using the vacuum collimator described by Burgh et al. (2001), we can determine the instrumental line-spread-function, and we find that the in-flight stellar profile matches our post-flight calibrations. Figure 4.4 shows the spatial profile of the nebular brightness (corrected for Ly-α airglow) that extends well beyond the intrinsic instrumental profile. Once the nebular surface brightness and stellar flux have been measured, their ratio (S/F$_\star$) can be taken. This reveals the most surprising feature of our observations: the ratio of nebular surface brightness to stellar flux rises roughly two orders of magnitude to the blue from 1400 to 900 Å, as shown in Figure 4.5. This sharp rise in S/F$_\star$ is in stark contrast with similar observations of the reflection nebulae NGC 2023 and 7023 (Burgh et al., 2002; Witt et al., 1993; Murthy et al., 1993), where the S/F$_\star$ is found to be constant with wavelength in the far-UV regime.

4.3   *FUSE* Observations of IC 405

Additional nebular observations were made by *FUSE* from 11 to 13 March 2003 on four positions within IC 405 (programs D12701, 02, 03, and 04). Spectra were obtained in the 905–1187 Å bandpass with the low-resolution (LWRS) aperture ($30'' \times 30''$) on *FUSE* (see Moos et al. 2000 for a satellite description and Sanhow et al. 2000 for on-orbit per-
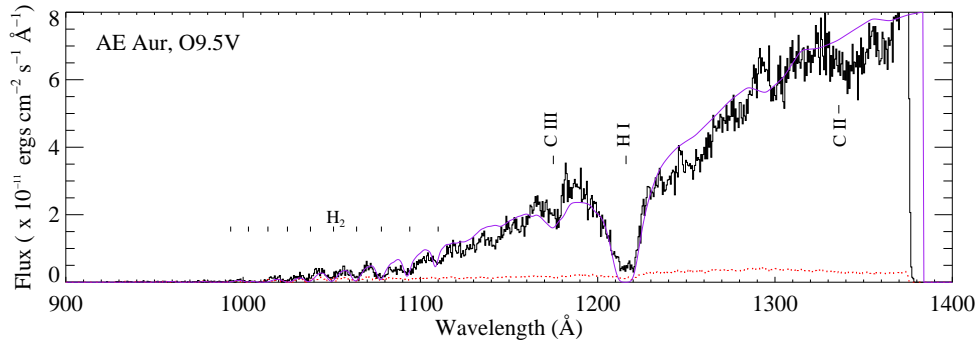
Figure 4.3 The spectrum of HD 34078, overplotted with a stellar model extinguished by the parametrization of Fitzpatrick and Massa and a model of H_2 absorption.

Position	Program	RA (2000) (^{h} ^{m} ^{s})	δ (2000) ($^\circ$ $'$ $''$)	Integration Time (seconds)	B(1060 Å)
IC405-01	D12701	05 16 12.15	+34 18 49.3	1850	2.0 x 10^{-5}
IC405-02	D12701	05 16 24.15	+34 18 49.3	1880	2.7 x 10^{-5}
IC405-03	D12703	05 16 30.21	+34 24 56.4	12630	3.5 x 10^{-6}
IC405-04	D12704	05 16 18.64	+34 32 25.2	12445	1.1 x 10^{-6}

Table 4.1 Summary of *FUSE* observations of IC 405.

formance characteristics). Assuming that the nebulosity fills the LWRS aperture, a spectral resolution of 0.33 Å is achieved at 1060 Å. Positions 01 (Pos1) and 02 (Pos2) were observed for 1850 and 1880 seconds, respectively, corresponding to the bottom and top of the long-slit of the rocket spectrograph. Position 03 (Pos3) was observed for 12.6 ks, overlapping with the "off-star" rocket pointing and Position 4 (Pos4), a bright optical filament north of the star was observed for 12.4 ks. Using an approach similar to the unsharp masking technique described by Witt and Malin (1989), we suspect Pos4 to exhibit Extended Red Emission (ERE). A list of the *FUSE* pointings is given in Table 5.1. The brightnesses quoted in the table are in units of ergs cm^{-2} s^{-1} Å^{-1} sr^{-1}.

Data for all four pointings were obtained in "time-tagged" (TTAG) mode and were initially processed using the CALFUSE pipeline, version 2.2.3. The calibrated data files for each orbit were then combined using IDL software, and when possible, the individual
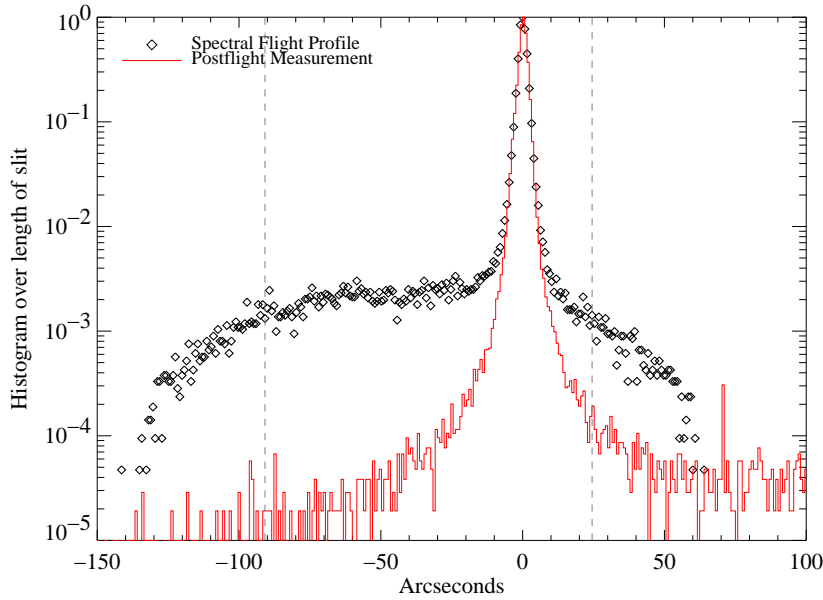
Figure 4.4 Spatial profile of the flight data in black (excluding Ly-α airglow). Postflight determination of the instrument line-spread-function reproduces flight profile. The dashed lines represent the portion of the spectrograph slit unaffected by instrumental vignetting. One notices the extension of the nebula beyond the stellar peak.

channels were combined using a cross-correlation algorithm. Due to the diffuse nature of the targets, there were instances where this algorithm failed; in these cases, the channels were analyzed independently.

The increased sensitivity and spectral resolution of *FUSE* allowed us to confirm the blueness found in IC 405 and to determine the contribution of fluorescent H_2 to the nebular surface brightness. HD 34078 has been observed by *FUSE* under program A070 and stellar spectra were obtained from the MultiMission Archive at the Space Telescope Science Institute (MAST). With the spatial information obtained by multiple pointings in the case of the *FUSE* data, we were able to confirm the rocket result independently. Figure 4.6 shows a similar blue $S/F_\star$ at all four pointings. The $\log_{10}(S/F_\star)$ was fit at wavelengths unobstructed by terrestrial airglow lines or interstellar absorption from 912 – 1150 Å in the Pos1 spectrum, where the scattered stellar continuum was bright (the long wavelength
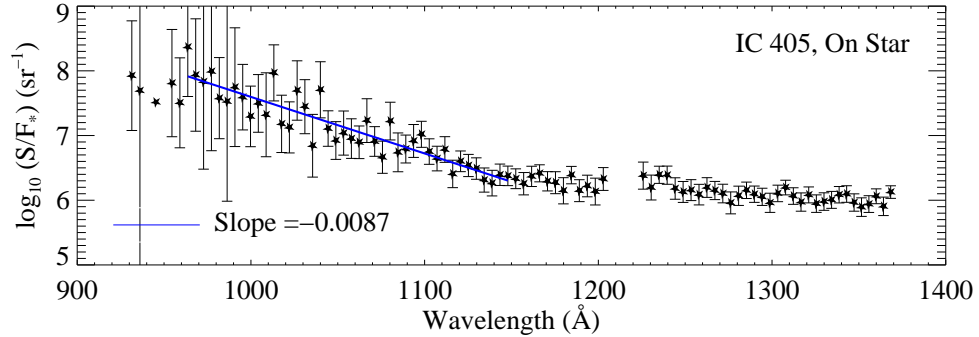
Figure 4.5 The ratio of nebular surface brightness to stellar flux measured by the sounding rocket experiment. Note the rise of approximately two orders of magnitude to the blue across the bandpass.

limit was chosen to avoid "The Worm" present in the data). We find that the data is well matched by a linear fit with a slope of $(8.4 \pm 0.4) \times 10^{-3}$, averaged over all positions. For comparison, the rocket derived $S/F_\star$ was fit using the same procedure and the agreement is good, $(8.7 \pm 0.6) \times 10^{-3}$.

Figures 4.7 and 4.8 display the nebular spectra evolving from the influence of a strong radiation field very near the star (Pos1, $\chi \sim 10^5$, where χ is the average interstellar radiation field; Draine (1978)) to the furthest offset, approximately $1000''$ to the north (Pos4, $\chi \sim 10^3$). Both spectra are overplotted with a synthetic H_2 emission spectrum, created by a fluorescence code similar to the one described in Wolven et al. (1997). Pos1 and Pos2 are dominated by a scattered stellar spectrum, with pronounced H_2 absorption troughs but only hints of H_2 emission near 1100 and 1160 Å. Pos3 shows the scattered stellar spectrum less strongly as the influence of HD 34078 diminishes with distance, and the H_2 emission becomes clear. The separation from the star is great enough at Pos4 (≈ 2 pc at the stellar distance of 450 pc) that the numerous fluorescent emission lines appear strongly from 1050 Å to the end of the bandpass near 1187 Å. The observed nebular lines arise from electronic transitions ($B^1\Sigma_u^+$ and $C^1\Pi_u$ to $X^1\Sigma_g^+$) that decay from the ground and first excited vibrational state ($v = 0, 1$).

49

4.4   Results and Discussion

The strong blue rise in IC 405 is remarkable because both observational (Burgh et al., 2002; Witt et al., 1993; Murthy et al., 1993) and theoretical (Weingartner and Draine, 2001) studies find a decreasing albedo across the far-UV bandpass. What mechanism is responsible for not only overcoming the falling albedo but increasing the observed nebular brightness? We consider:

- Peculiar dust grain properties (unusual values of a and g) in IC 405,

- Strong fluorescent H_2 emission that falls below the sensitivity and spectral resolution of the rocket experiment,

- Unusually small grain distribution leading to a strong Rayleigh scattered component of the nebular brightness,

- An unusual dust emission process, an extended blue emission, and

- Differential extinction in IC 405 due to a complicated local geometry or an intervening clump of gas and dust along the line of sight to HD 34078

4.4.1   Dust Modeling

The dust scattering in IC 405 was modeled using a modified version of the code described by Burgh et al. (2002), employing a Monte Carlo dust radiative transfer model (see also Gordon et al. 2001). The model follows the path (direction and position) of each photon in the nebula from its "creation" at the position of the star, until it leaves the nebula (i.e., its radial position is outside the defined size of the nebula). The factors that determine the position and direction of the photons during their propagation through the nebula are the optical depth of the dust, the fraction of photons scattered by the dust rather than absorbed (the albedo), the angular distribution of the scattered photons (parameterized by g in the scattering distribution given by the Henyey-Greenstein 1941 phase function), and the geometry of the dust distribution. Although Draine (2003b) has argued that the H-G function does not reproduce the scattering function calculated from the optical properties of dust

models in the far-UV bandpass, we use it here to allow for a direct comparison with the result from Burgh et al. (2002). A revision of our model replacing the H-G phase function with a function that depends on the scattering cross-sections for dust grains in the far-UV (as well as more sophisticated geometries) will be addressed in a future work. Given inputs for the number of photons followed, the optical depth, albedo, and g, the model outputs an image of the nebular surface brightness that can be compared to the distribution measured by the rocket experiment. The rocket data are binned by wavelength region to improve S/N, and then plotted as a function of spatial position along the slit.
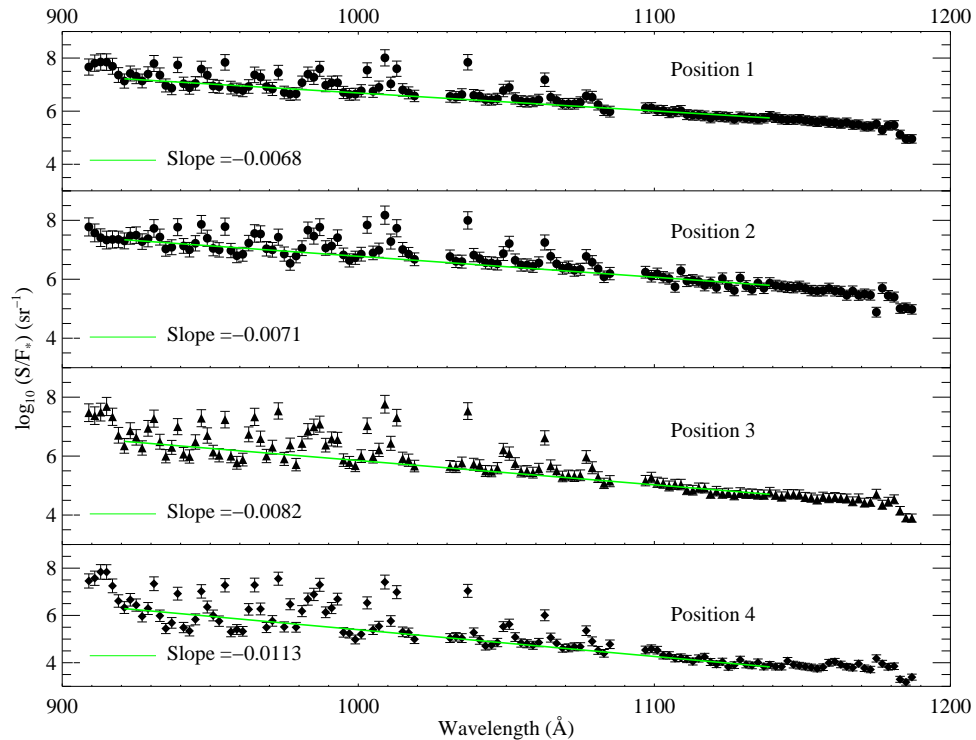
Figure 4.6 The ratio of nebular surface brightness to stellar flux at the four positions observed by *FUSE* confirm the blue rise discovered by the rocket data. The slope was determined at wavelengths where there was no contamination from airglow features or interstellar absorption in the Pos1 S/F$_\star$.

This model, which works well to closely approximate the observed surface brightness distribution in the bright reflection nebula NGC 2023, fails to reproduce the nebular surface brightness of IC 405 by orders of magnitude (Figure 4.10). Models were run for a number

of values for the optical depth, *a*, *g*, and nebular geometry. Models explored spherical geometries with constant density and $\rho \propto r^{-\alpha}$, as well as spherical shell and a constant density slab. The results are best illustrated by considering two specific cases, shown in Figure 4.10, the first using the *a* and *g* from Weingartner and Draine (2001) for $R_V = 4.0$. The model shows poor agreement across the bandpass, particularly at the short wavelength end (a result of the nebular blueness). The second model finds the best fit to the short wavelength data, revealing $a = 0.9$, $g = 0.1$, in strong disagreement with both theoretical and other measured values in this wavelength regime (see Draine 2003a and references therein). Additionally, a 50% differential extinction was needed in the best-fit 950-1050 Å model; i.e. the stellar flux directly along the line of sight to the observer was reduced by a factor of two. As this model begins to reproduce the short wavelength result, the longer wavelength data is in poor agreement. This exercise clearly shows that this reflection nebula is not well described by a smooth and uniform dust distribution. More sophisticated models, employing varying dust densities, complex geometries, and more appropriate scattering phase functions than exist at present may be able to reproduce our observations of IC 405.

4.4.2 Comparison with Previous Studies of Other Reflection Nebulae

Only one far-ultraviolet observation exists that includes both spatial and spectral information, however there are a few previous data sets that put our $S/F_\star$ result in context. Burgh et al. (2002) reported on observations of NGC 2023 made with the same rocket-borne imaging spectrograph described above. This nearly identical observation, made in 2000 February, found that the ratio of nebular surface brightness to stellar flux was constant with wavelength across the 900 to 1400 Å bandpass. They model the nebular scattering properties (as described above) and determine that a decreasing dust albedo is being offset by grains that are more strongly forward scattering at shorter wavelengths (increasing *g*).

Witt et al. (1993) and Murthy et al. (1993) used observations made by the *Hopkins Ultraviolet Telescope* (*HUT*) to measure $S/F_\star$ in another bright reflection nebula, NGC 7023, without the benefit of a spatially resolved slit. Murthy et al. describes the *HUT* observations made during the Astro-1 mission in 1990 December, obtaining a spectrum of the central star (HD 200775) and then offsetting to a pointing within the nebula. They

obtained data with an appreciable signal in the 1100 – 1860 Å region and also found that the S/F$_\star$ ratio was constant with wavelength. They use a Monte Carlo scattering model (described by Witt et al. 1982) and find a decreasing albedo for $\lambda <$ 1400 Å (assuming $g = 0.7$). This result agrees with that of Witt et al. (1993), who combined the *HUT* stellar observation with data from the ultraviolet spectrometer on *Voyager* 2 and found a drop in the albedo of 25% between 1300 and 1000 Å. The observed S/F$_\star$ is found to be flat across this wavelength region. An increase in nebular surface brightness of 25% from an unresolved H$_2$ emission component is assumed to counteract the falling albedo (Witt et al., 1993; Sternberg, 1989). Ultraviolet studies of a similar nature have been carried out on the Scorpius OB association (Gordon et al., 1994), IC 435 (Calzetti et al., 1995), and the Pleiades reflection nebula (Gibson and Nordsieck, 2003), but these studies focused on longer wavelengths than considered here. Far-UV Observations of NGC 2023 and NGC 7023 at wavelengths below Ly-α are presented in Chapter 5.
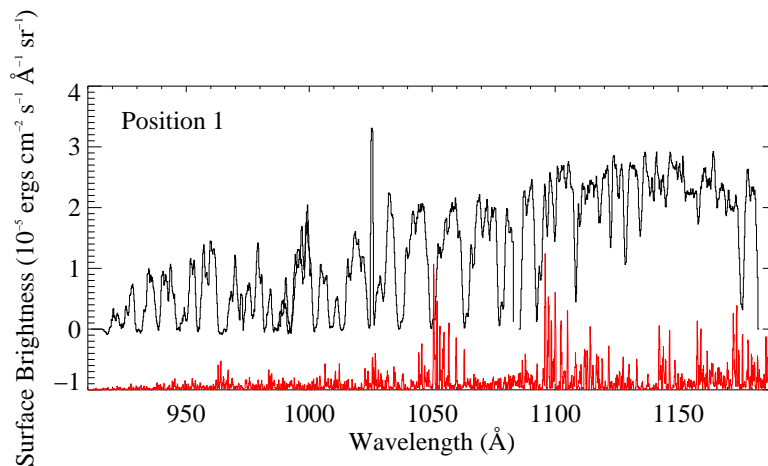

Figure 4.7 The *FUSE* spectrum of Pos1. The spectrum is dominated by scattered stellar continuum. The data have been smoothed with a 5-pixel boxcar average for display purposes. The brightest emission feature is geocoronal Ly-β. A synthetic spectrum of fluorescent H$_2$ is overplotted as a red dashed line to guide the eye.

4.4.3 Mechanisms for Producing the Blue Rise

As our dust scattering models fail to reproduce the short wavelength rise in S/F$_\star$ for realistic values of grain parameters in IC 405, we consider other possibilities. Ultraviolet H$_2$ emission is clearly present in IC 405, the double peaked emission feature near 1600 Å was first seen by *HUT* (spectrum ic405_080, Figure 4.9) and our *FUSE* data resolve the individual rotational components of several vibrational bands between 1050 and 1185 Å (Figure 4.8). Near HD 34078 however, we find little evidence for H$_2$ emission as either the continuum overwhelms the fluorescent signal or the χ/n environment is unfavorable for the fluorescent process (Sternberg, 1989). Regardless of the relative contribution of fluorescing H$_2$ to the nebular spectrum, each of our pointings in IC 405 reveal a very similar, blue S/F$_\star$ ratio. The evolution of the fluorescence signature with distance from the exciting star is interesting, but the constancy of the nebular brightness to stellar flux rules out molecular hydrogen as the dominant cause of the blue rise in IC 405.
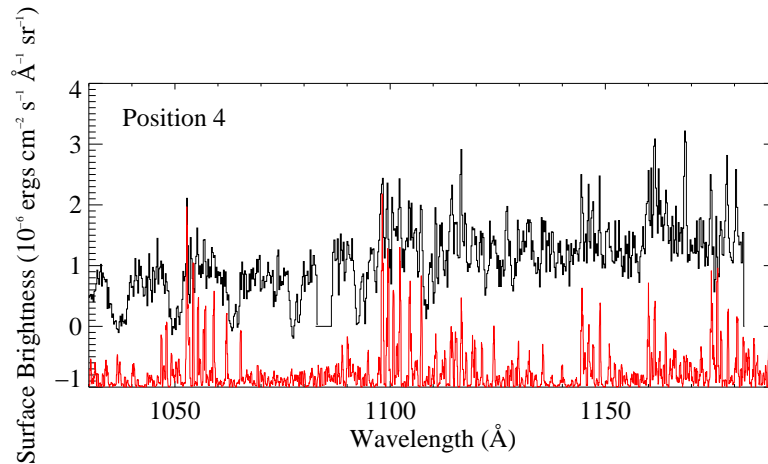
Figure 4.8 *FUSE* spectrum of Pos4, 1000$''$ north of the star. H$_2$ emission is now the most prominent spectral feature from 1050 to 1180 Å.

A small grain population has been suggested for NGC 7023 (Murthy et al., 1993; Witt et al., 1993), yet these grains are expected to be efficient absorbers of far-UV radiation. We have no reason to expect to find a unique distribution of high albedo grains in IC 405, although we note that the large proper motion of HD 34078 brings it into contact with grains
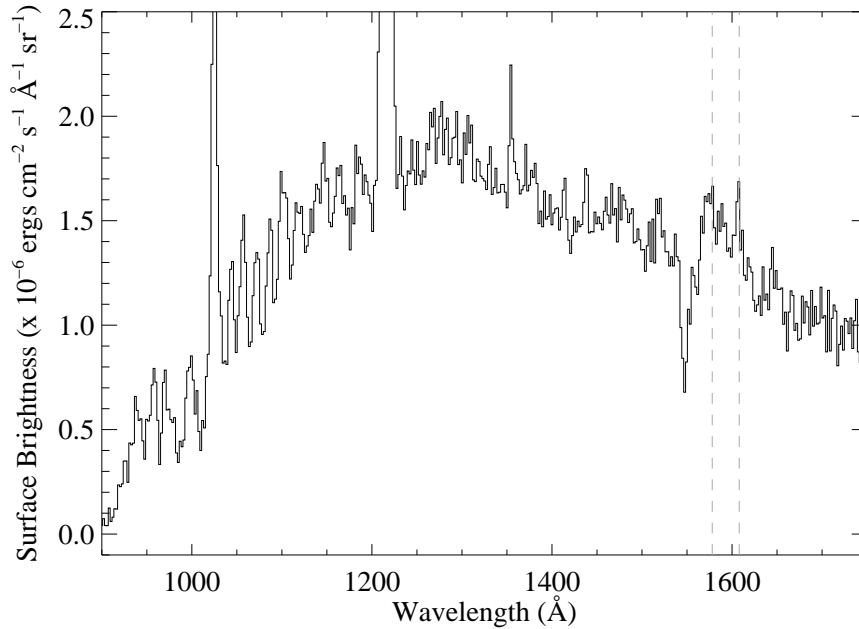
Figure 4.9 The raw HUT spectrum of IC 405 showing the $\lambda\lambda 1578/1608$ H_2 emission feature. This spectrum was acquired near Pos3.

that are unlikely to have undergone significant processing by UV photons. The exciting stars of NGC 2023 and 7023 are thought to be born in the presence of the dust with which they are interacting, clearly a different scenario than in IC 405. It is interesting to note that Vijh et al. (2004) have recently found a continuous near-UV/optical emission in the Red Rectangle nebula which they attribute to fluorescence by small polycyclic aromatic hydrocarbon (PAH) molecules. We are unaware of a molecular continuum process that operates at far-UV wavelengths, however we cannot conclusively rule out a contribution from PAH molecules. Further studies of the vacuum ultraviolet emission and absorption properties of PAH molecules would be of interest.

Mathis et al. (2002) have argued that clumpy dust distributions make grain properties derived from observations of reflection nebulae unreliable. They develop a model of hierarchical clumping that predicts widely varying determinations of the albedo and the scattering parameter depending on the viewing angle, the degree of clumping, whether the central star
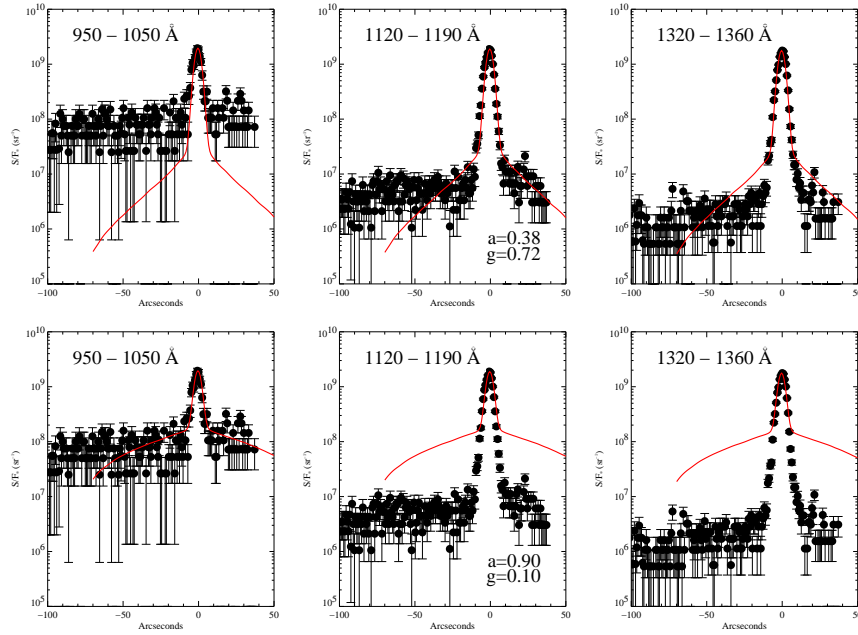
Figure 4.10 Spatial S/F$_\star$ measured with the rocket experiment compared with models. The top panels are models using theoretical values of *a* and *g* at 1350 Å, the bottom panels attempt to fit the short wavelength S/F$_\star$, using a differential extinction of 50% with *a*=0.9 and *g*=0.1. The models differ from the one described in Burgh et al. by the use of a geometry that employs a larger inner cavity cleared out by the stellar wind and high proper motion and includes the differential extinction correction.

happens to reside inside a dense clump, and the density of the interclump medium. As dust scattering models and molecular hydrogen fluorescence have failed to reproduce our data, and other explanations seem speculative at this time, we adopt differential extinction due to a clumpy dust distribution as the most probable explanation for the blue S/F$_\star$ ratio in IC 405. A small interstellar clump/filamentary structure or circumstellar feature directly along the sight line to HD 34078, but not present in front of the rest of the nebula would preferentially extinguish the shorter wavelength stellar photons reaching us directly, thus making the denominator in S/F$_\star$ small at short wavelengths. Our dust scattering models are unable to account for such complex geometries, but we can begin to study the degree of clumpiness by examining the extinction in IC 405.

4.4.4 Differential Extinction Limits

We can put limits on a differential extinction level that can account for the blue rise by quantifying the extinction properties and physical size of an obscuring clump. We begin by determining the level of variation in the extinction curve between HD 34078 and the region surrounding it. Using the extinction curve to deredden the HD 34078 line of sight will constrain the difference in attenuation between the stellar and nebular lines of sight. We deredden the HD 34078 sight line by dividing the stellar spectrum by the observed extinction curve. An extinction curve is created following the pair method, a correction for molecular hydrogen absorption is applied, and then the resultant curve is fit using the parameterization of Fitzpatrick and Massa (1990). HD 93521, (09V, $E(B - V) = 0.02$; Buss et al. 1995) was used as the comparison star and the extinction curve was created between 900 and 3000 Å from a combination of the rocket data and archival IUE and HUT spectra. Molecular hydrogen absorption was corrected for using the H_2ools absorption templates for the parameters described in §2.2 (McCandliss, 2003; Sasseen et al., 2002). We find the FM-fit parameters to be $(x_0, \gamma, c_1, c_2, c_3, c_4) = (4.59, 0.94, 0.17, 0.37, 6.25, 1.05)$. Repeating our S/F$_\star$ analysis using the dereddened star, we find that the ratio is constant across the rocket bandpass. Assuming that the extinction curve only applies to the stellar sight line seems to account for the blue rise, but comes with the implication that the nebula has a foreground extinction of zero. If differential extinction is the sole mechanism at work in creating a blue S/F$_\star$ in IC 405, then all of the observed reddening would appear to originate in a small clump along a pencil-beam to HD 34078.

We determine the size of such a "small clump" by measuring the nebular brightness profile along the rocket slit at the "on-star" pointing, and find the the clump size must be smaller than about $20''$. It is unclear where the clump is located along the line of sight to HD 34078, but an upper limit on the physical size can be set by requiring it to be near the star, we find the upper limit to be 0.04 pc. Variations have recently been detected in the column density of CH along the line of sight to HD 34078, suggesting structure on the scale of tens of AU (Rollinde et al., 2003). One possible explanation for the N(CH) variation is the presence of a clump along the HD 34078 line of sight, newly present due to the high proper motion of the star, although the the analysis presented in Rollinde et al.

(2003) finds this hypothesis to be unlikely. Independent of the location of the clump, there is other evidence of multiple absorption components along the line of sight. In addition to the scattered stellar continuum seen at Pos1, $FUSE$ spectra of HD 34078 revealed both cold (T = 80 K) and highly excited H_2 in absorption (Le Petite et al., 2001; Rollinde et al., 2003). The ambient interstellar radiation field is insufficient to excite H_2 to the observed levels (up to $\nu = 0$, $j = 11$), implying the relative proximity of HD 34078.

4.4.5   Consequences for Unresolved Observations

We note that if IC 405 were observed in a spatially unresolved manner or seen from a large distance, HD 34078 would appear to be less extinguished than in the present case, where the star and nebula can be measured separately. If observed at a large distance, the integrated blue nebular continuum and the reddened star light would be considered stellar in origin, artificially dereddening the intrinsic stellar continuum. As a rough determination of how such an observation may be biased, we assume a uniform surface brightness filling the rocket slit at the on-star pointing, and estimate the contribution of the nebular flux to the total observed spectrum in the unresolved case. In the simple case of a constant surface brightness nebula the length of the rocket long-slit on each side ($200'' \times 200''$, ≈ 0.4 pc $\times 0.4$ pc), we determine a nebular filling factor correction of about 15. Multiplying the nebular flux measured during the on-star position by the filling factor and adding that to the stellar flux, we determine how bright HD 34078 would appear in an unresolved observation. Taking a constant flux of $\approx 1.0 \times 10^{-12}$ ergs cm^{-2} s^{-1} Å^{-1} at 1100 Å (from the nebular spectrum observed by the rocket, consistent with the $FUSE$ measurement), we find that the integrated nebular flux would be $\approx 1.5 \times 10^{-11}$ ergs cm^{-2} s^{-1} Å^{-1}, 50% brighter than the star itself. A spatially unresolved far-UV observation of IC 405 would lead one to measure a stellar flux level 2.5 times (one magnitude) greater than the true value. This effect is reminiscent of the observed UV properties of local starburst galaxies described by Calzetti (1997). Local starbursts show less extinction of the stellar continuum relative to the nebular emission lines, explained by a clumpy dust distribution that preferentially reddens nebular light due to the different filling factors of the stars and gas. Calzetti (1997) finds that stellar photons only encounter approximately 60% of the dust seen by nebular photons.

4.5 Summary of Chapter 4

The emission/reflection nebula IC 405 was observed by a rocket-borne, long-slit imaging spectrograph in the far-ultraviolet bandpass (900 – 1400 Å). A high quality spectrum (S/N $\approx$ 10 – 15) was obtained of the central star, HD 34078, as well as the spectra of the surrounding nebula out to an offset approximately a parsec from the star. We found that the ratio of nebular surface brightness to stellar flux (S/F$_\star$) rose by two orders of magnitude to the blue across the bandpass of the instrument. This result is in conflict with analogous observations of reflection nebulae in this wavelength regime (NGC 2023 and 7023), where flat S/F$_\star$s were observed. This result held true for both positions within the nebula. Additional observations were made with $FUSE$ in an attempt to clarify the process responsible for the blue rise. $FUSE$ observed four positions within IC 405, three coincident with the rocket pointings, and one along another bright nebular filament. These data revealed the nature of the nebular spectra: a progression from strong scattered stellar continuum near the star to the appearance of fluorescent emission from H$_2$ farthest from the star. An analysis of S/F$_\star$ confirmed the blueness throughout IC 405, showing little correlation with the nebular spectral characteristics.

Models of scattering in a uniform dust distribution, similar to those that accurately reproduce the observed S/F$_\star$ in NGC 2023, were unable to fit IC 405 for realistic values of the albedo and the phase function asymmetry parameter for the geometries studied. The presence of fluorescent H$_2$ creating excess emission to the blue while going undetected at the resolution of the rocket experiment has been ruled out by $FUSE$, as S/F$_\star$ remains constant regardless of the relative contribution of H$_2$ to the spectrum. More exotic explanations, such as an extended blue emission from dust, are speculative. We favor the hypothesis of differential extinction as caused by a clumpy dust distribution, which has been suggested by Mathis et al. (2002) to complicate the conclusions drawn from observations of reflection nebulae. Differential extinction along the line of sight to IC 405, such as a knot or filament of gas and dust on the sight line to HD 34078 but not crossing the path to the rest of the nebula can account for the blue rise if one assumes the obscuring material is very local to the HD 34078 line of sight. Our observations have placed an upper limit to the size of the intervening clump of 0.04 pc. If clumpy dust is responsible for the blue rise that we have

found, it seems that IC 405 is the prototypical example for arguments against the use of reflection nebulae for reliable determination of dust grain properties. IC 405 appears to be a local example of the differential extinction process that may take place in starburst systems on a global scale.

Chapter 5

On the Search for Far-Ultraviolet Molecular Hydrogen Fluorescence in the Reflection Nebulae NGC 2023 and NGC 7023

"The light in the dust lies dead; When the cloud is scattered,
The rainbow's glory is shed"   – Percy Bysshe Shelley

5.1   Introduction

Two of the best studied of the best-studied PDRs on the sky are the reflection nebulae are NGC 2023 and NGC 7023. Several studies of each object have been performed with the aim of understanding the ultraviolet properties of dust (Witt et al., 1993; Murthy et al., 1993; Burgh et al., 2002) as well as determining the infrared (IR) emission characteristics of H_2 and polycyclic aromatic hydrocarbons (PAHs, Gatley et al. 1987; Martini, Sellgren, and DePoy 1999; Takami et al. 2000; Werner et al. 2004). In this Chapter, we extend the molecular hydrogen studies cited above to the electronic transitions of the hydrogen molecule by presenting new far-UV observations of NGC 2023 and NGC 7023.

NGC 2023 is a reflection nebula in Orion, one of the brightest in the sky (Martini et al.,

1999; Burgh et al., 2002). It is illuminated by HD 37903, a B1.5V star which is embedded within the nebula (V = 7.84, d $\approx$ 450 pc). NGC 2023 was one of the first reflection nebulae in which H_2 was detected in the infrared (Gatley et al., 1987), and several groups have presented high-quality data sets of these emissions, using both spectroscopy and narrow band imaging (Martini, Sellgren, and DePoy 1999; Takami et al. 2000). NGC 2023 was also recently observed by a rocket-borne long-slit, imaging spectrograph at low resolution ($R \approx 300$) in the far-UV (900 – 1400 Å) and these data showed evidence for emission above the scattered light models used to characterize the nebular dust (Burgh et al., 2002). The authors tentatively conclude that this excess emission is due to a population of fluorescent H_2 that was unresolved at the rocket resolution.

NGC 7023 is located in Cepheus, at a distance of approximately 440 pc. The central star is HD 200775, a pre-main-sequence B3e (V = 7.42). As with NGC 2023, high quality infrared data sets exist, including images and spectra (Martini, Sellgren, and DePoy 1999; Takami et al. 2000, Werner et al. 2004). Witt et al (1993), combining spectra from the Hopkins Ultraviolet Telescope (HUT), aboard *Astro-1*, with data from *Voyager* 2, explain the roughly constant ratio of nebular surface brightness to stellar flux in the region from 1000 – 1300 Å as the result of fluorescent H_2 emission offsetting a decreasing dust albedo. This chapter presents new far-UV spectroscopy of these two objects obtained with the *Far Ultraviolet Spectroscopic Explorer* (*FUSE*) to search for the suggested emissions from H_2. We complement these *FUSE* data with archival observations made using HUT and the *International Ultraviolet Explorer* (*IUE*). These supporting observations allow us to sample the entire wavelength region spanned by the ultraviolet fluorescence of molecular hydrogen. In § 5.2, we briefly describe the *FUSE* observations. The supporting observations are described in § 5.2.1. § 5.3 describes the data analysis performed, including the correction made for contamination from dust scattered continuum, and observational results, the positive identification of H_2 in the *IUE* and HUT data and the surprising apparent lack of fluorescent emission in the *FUSE* spectra. Possible explanations for the non-detection are discussed in § 5.4 and a brief summary is presented in § 5.5.
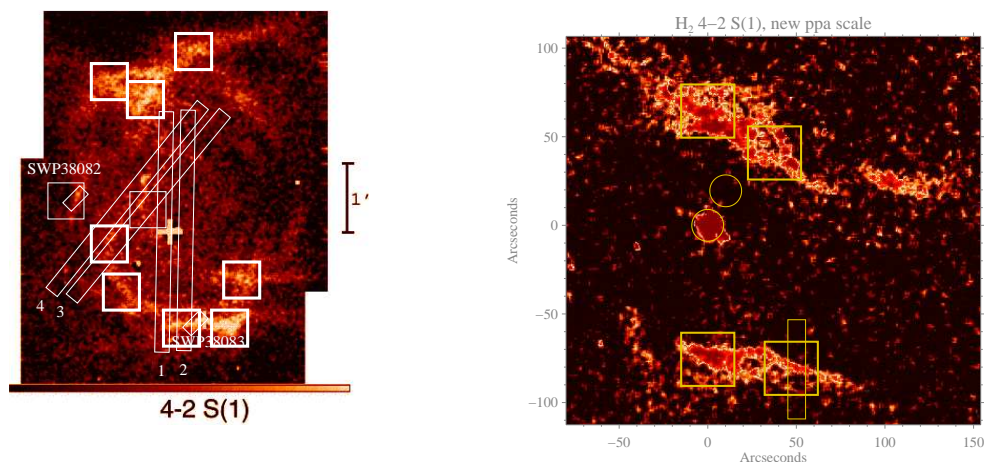
Figure 5.1 Images of NGC 2023 (Left) and NGC 7023 (Right) in the near-IR 4-2 S(1) emission line of H_2, from Takami et al. (2000). This line suggests that UV fluorescence is responsible for the molecular excitation. The projected apertures of the *FUSE* observations discussed in this Chapter are shown overplotted as boxes. The southwestern NGC 7023 pointing was not observed. (*NGC* 2023 *figure by Eric Burgh*.)

5.2 *FUSE* Observations of NGC 2023 and NGC 7023

NGC 2023 was observed by *FUSE* on 2004 January 13 and 14. The low-resolution aperture (LWRS; $30'' \times 30''$) was used to obtain nebular spectra at eight positions within the nebula, shown overlaid on the near-IR H_2 map of Takami et al. (2000) in Figure 5.1. These observations were made in time-tagged (TTAG) mode, with a total integration time of ~ 39 ksec. These data were obtained under the C127 guest investigator program, and were reduced using the CalFUSE pipeline v2.4.1. The near-IR maps of Takami et al. (2000) were also used to guide our observations of NGC 7023 (Figure 5.1). *FUSE* observed three positions within NGC 7023 on 2003 October 13 and 14. These data were also acquired in TTAG mode, with a total integration time of ~ 42 ksec. Nebular spectra of NGC 7023 were obtained under guest investigator program D127, and reduced with CalFUSE v2.4.1. These filled slit observations have a spectral resolution of roughly 0.33 Å. Details about the individual pointings are given in Table 5.1.

Table 5.1. Summary of *FUSE* observations of NGC 2023 and NGC 7023.

| Position	Program	RA (2000) (^{h} ^{m} ^{s})	δ (2000) ($^\circ$ $'$ $''$)	Integration Time (seconds)
NGC2023-N1	C12701	05 41 41.60	-02 13 28.4	3166
NGC2023-N2	C12702	05 41 39.60	-02 13 43.4	7826
NGC2023-N3	C12703	05 41 37.00	-02 13 03.4	4613
NGC2023-E1	C12704	05 41 41.60	-02 15 43.4	4692
NGC2023-E2	C12705	05 41 41.00	-02 16 23.4	3523
NGC2023-S1	C12706	05 41 37.60	-02 16 53.4	4701
NGC2023-S2	C12707	05 41 35.00	-02 16 53.4	7836
NGC2023-S3	C12708	05 41 34.30	-02 16 13.4	2536
NGC7023-01	D12701	21 01 32.92	+68 10 12.0	15774
NGC7023-02	D12702	21 01 36.92	+68 09 30.0	19203
NGC7023-03	D12703	21 01 36.92	+68 10 26.0	7126
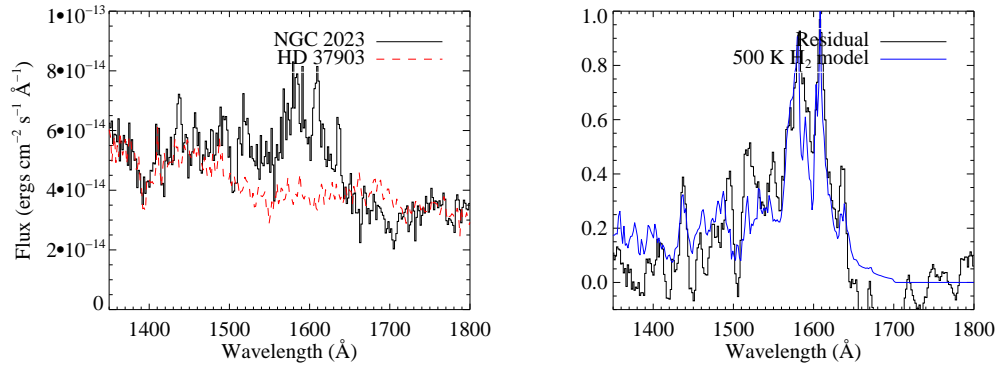
Figure 5.2 A portion of the *IUE* spectra of NGC 2023 and the central star HD 37093, scaled to the nebular flux. The stellar flux is used to subtract the dust scattered light. The residual spectrum is shown with a synthetic H_2 spectrum overplotted in blue for comparison.

5.2.1 Supporting Far-UV Observations and Analysis

NGC 2023 was observed by *IUE* on 1990 January 26. A 10.8 ksec exposure was made through the low dispersion large aperture and recorded by the Short Wavelength Primary camera (spectrum SWP38082; Burgh et al. 2002). The scattered light subtraction described below was made using the stellar flux from SWP08055, a 32 second exposure of HD 37903 taken on 1980 August 15. Comparable observations of NGC 7023 were made with HUT. The spectrum of a nebular pointing was obtained by HUT during the *Astro-2* mission in 1995 March (ngc7023_098). 1668 seconds of nighttime data was recorded through the $10'' \times 56''$ aperture. The spectrum of HD 200775 was obtained through the $17''$ diameter circular aperture employed on *Astro-1* in 1990 December (hd200775_196). 1456 seconds of nighttime data was used to make a scattered light subtraction in this nebula. All of the supporting data presented here were obtained from the Multi-Mission Archive at the Space Telescope Science Institute (MAST).

5.3 Analysis of the Far-UV Data

The signal from H_2 emission in these UV data sets is expected to be entangled with dust scattered continuum from the central stars of the two objects. Thus, a subtraction of this
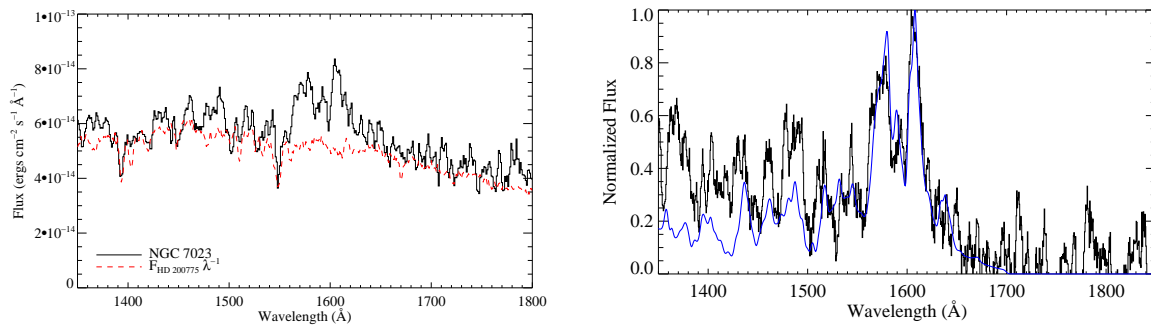
Figure 5.3 The HUT spectra of NGC 7023 and HD 200775. Again, the residual spectrum shows emission lines from H_2.

scattered continuum, similar to that described by Witt et al. (1989) (and applied to the HUT spectrum of IC 63 in Chapter 2) is necessary. We apply separate corrections of the form $aF_\star\lambda^\beta$ to both the long ($\lambda > 1200$ Å) and short ($\lambda < 1200$ Å) wavelength UV data. $F_\star$ is the stellar spectrum for the given spectral region, λ^β is used to adjust the overall shape (i.e.-slope or reddening) of the individual spectra, and a is a scale factor used to adjust the flux level. The value of β required for each nebular region was seen to vary between 0 and –3, most likely a result of differential extinction effects within the nebula. Figure 5.2 shows an example of this approach for NGC 2023, using a one-temperature (500 K) model similar to those described in Chapter 2 to compare with the data. The double peaked emission feature of fluorescent H_2 is clearly present in the residual spectrum. Figure 5.3 shows the HUT spectrum used to make the scattering correction and a comparison of the residual to a 500 K H_2 model. Again, the $\lambda\lambda$1578/1608 Å feature is visible.
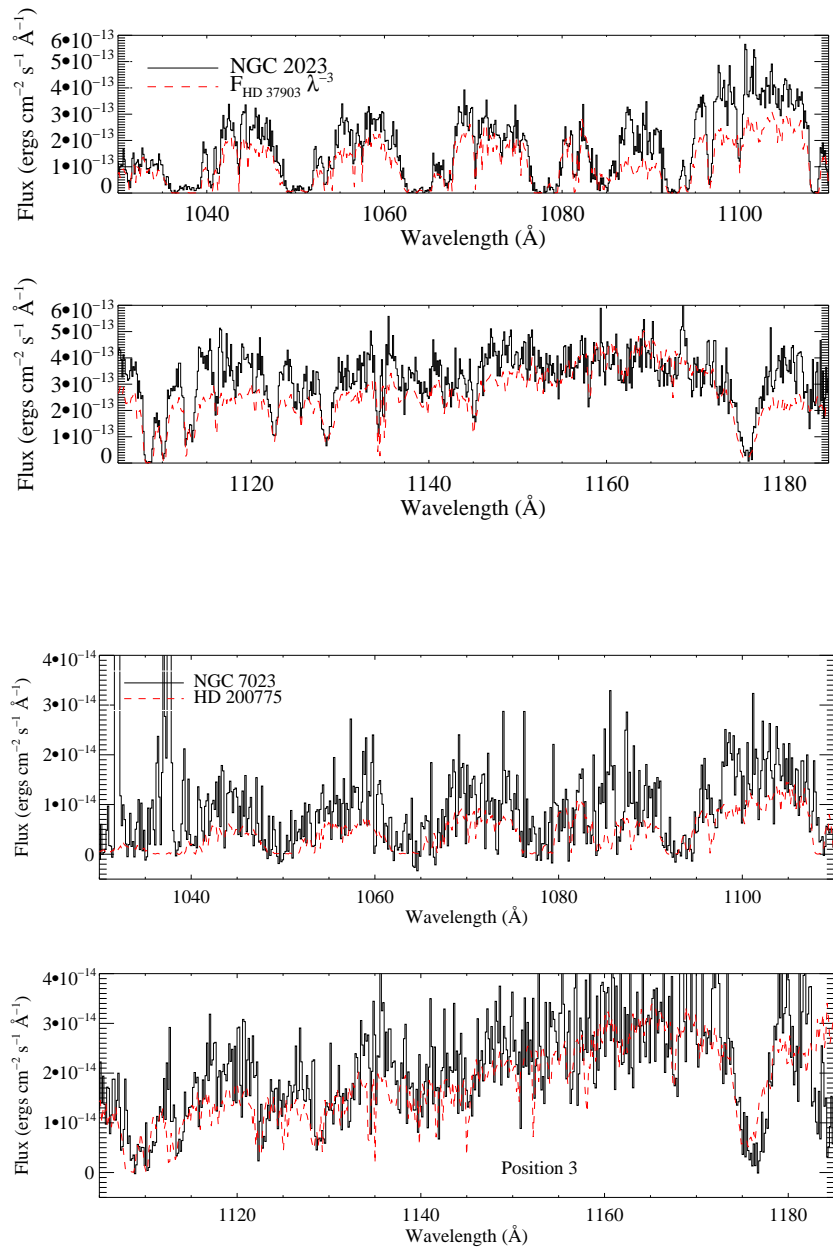
Figure 5.4 The *FUSE* spectra of NGC 2023 (Position E1) and NGC 7023 (Position 3) are shown in black. The scattered light spectra created using archival *FUSE* observations of their rescpective central stars, and are plotted as the broken red line. Extinction on the nebular line of sight limits the detectable signal to wavelengths longer than Ly-β in NGC 7023.
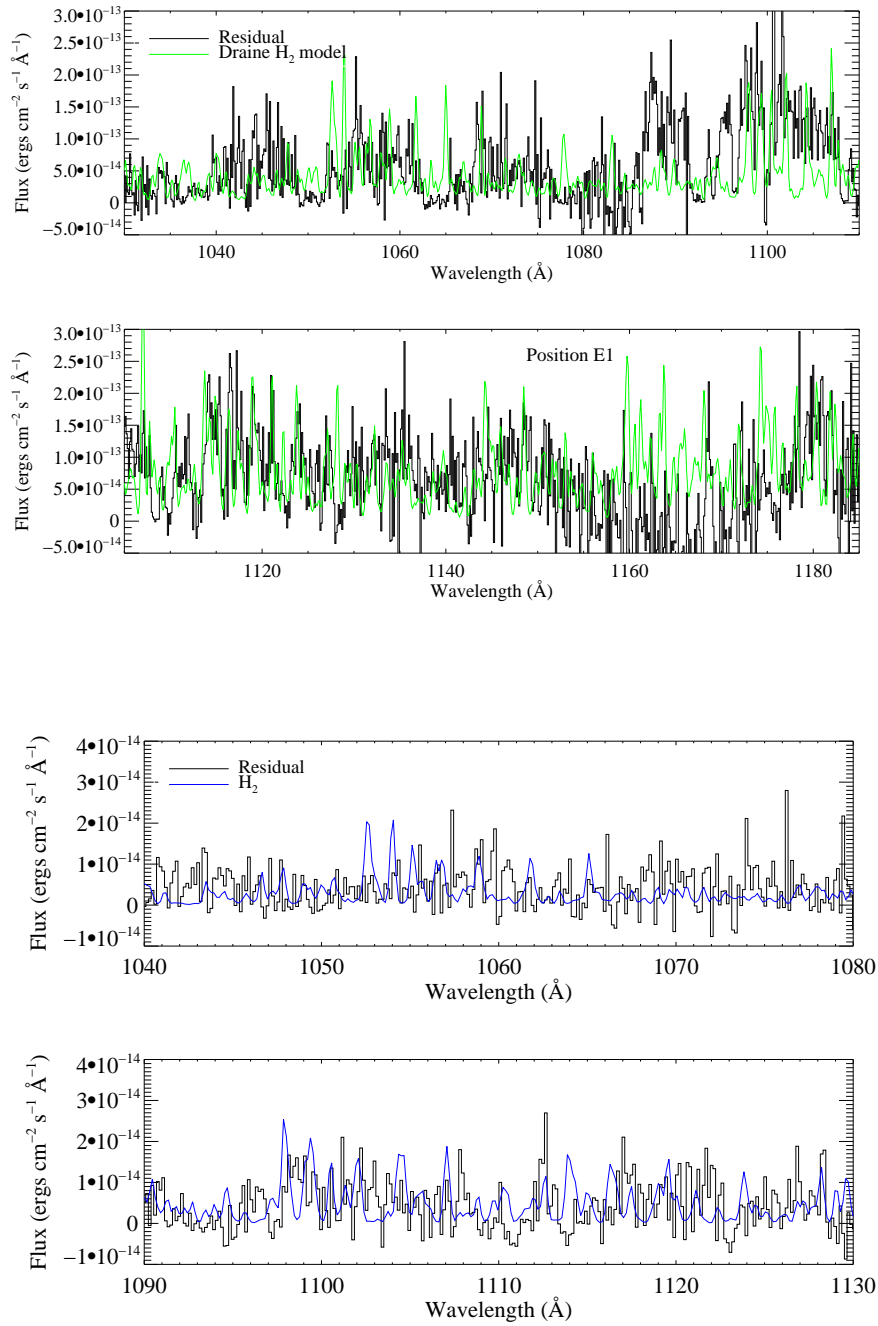
Figure 5.5 The residual spectra of NGC 2023 and NGC 7023 shows no clear evidence for H_2 emission. Overplotted on the NGC 2023 data in green is an H_2 emission model kindly provided by Bruce Draine. The model from Figure 5.3 is shown over NGC 7023.

The *FUSE* spectra of both reflection nebulae show a surprising lack of H_2 emission. Ratios of the near-IR emission lines are consistent with pumping by UV photons as the primary excitation mechanism (Takami et al., 2000), and the double-peaked emission feature near 1600 Å characteristic of continuum pumped fluorescence is shown in Figures 5.2 and 5.3. Despite these suggestions that NGC 2023 and NGC 7023 should be strong sources of H_2 emission in the *FUSE* band, comparison to to the continuum=pumped models described in this dissertation reveal large discrepancies. The spectra are dominated by scattered stellar continua, with imprints of the strong absorption by the $J = 0$ and 1 lines of H_2 and photospheric C III. The scattered light is mostly removed by the subtraction described above, and the residuals show nothing but airglow lines and incompletely subtracted scattered light. Figure 5.4 shows examples of the nebular spectra and the stellar spectra used for the scattered light subtraction. The residual spectra are plotted in Figure 5.5. For the case of NGC 2023, a synthetic H_2 spectrum created to predict the *FUSE* band emission in the nebula is overplotted (B. T. Draine 2000 - private communication). The residual spectrum of NGC 7023 is shown overplotted with the same 500 K synthetic spectrum that shows agreement with the residual HUT spectrum in Figure 5.3.

5.4 Where's the BEEF? (Bright Expected Emission Features)

This section addresses the question of why we do not appear to detect hydrogen fluorescence in NGC 2023 and NGC 7023 at *FUSE* wavelengths when it is predicted by theory and previous direct measurements of H_2 at other wavelengths. We suggest four possible causes for the non-detection:

- Far-UV H_2 emission is present in these objects and we simply looked in the wrong place

- The scattered light signal overwhelms the contribution from H_2, which can be understood as a geometrical effect

- Self-absorption by hydrogen molecules closer to us on the nebular lines of sight

- A coherent fluorescence process that smears out the closely spaced H_2 emission lines

Our pointing strategy for planning the *FUSE* observations was to choose observations that coincided with bright features in the near-IR maps of Takami et al. (2000) made in the 4–2 S(1) emission line of H_2 (Figure 5.1). Lines originating in highly excited vibrational states of the H_2 are thought to be populated following the UV fluorescence process, as collisional excitation would tend to dissociate the molecules. Additionally, the NGC 2023 E1 spectrum that is used as an example overlaps with the sounding rocket pointing that showed an excess over the scattered light model (Burgh et al., 2002). Figure 5.1 shows that our pointings cover a sizable fraction of the bright near-IR emission in both of the objects. One notable exception is the southwestern pointing in NGC 7023. This observation, which coincides with the HUT pointing presented here that shows the strong 1600 Å feature, was eliminated from our program by the review committee, citing low aperture filling fraction. Despite this unfortunate deletion, we feel that our spatial coverage was sufficient to detect the molecular emission from these objects, if it were present.

The second and third possibilities for the non-detection involve the nebular geometry. The spectra of both objects show the signature of scattered starlight, and given the strongly forward scattering nature of dust grains in the far-UV (Burgh et al., 2002; Draine, 2003b), it seems plausible that the surface brightness we observe is coming from the outer dust layers closest to us. Conversely the H_2 emission is only arising near the star where the UV flux is sufficiently intense to excite the molecules. A way of illustrating this is to compare the geometries of NGC 2023 and NGC 7023 with the geometries of IC 63 (Chapter 2) and IC 405 (Chapter 4). The regions that show a clear fluorescent H_2 signal in IC 63 and IC 405 are seen to have a "right angle" geometry with respect to their exciting stars. The central stars of NGC 2023 and NGC 7023 are more embedded in the clouds of gas and dust that they power. A cartoon example of this geometrical difference is shown in Figure 5.6. This geometrical argument explains both the absence of H_2 emission lines, they have been extinguished by the intervening nebular dust in the outer regions of the nebulae, and explains why the dust scattered stellar spectrum is observed.
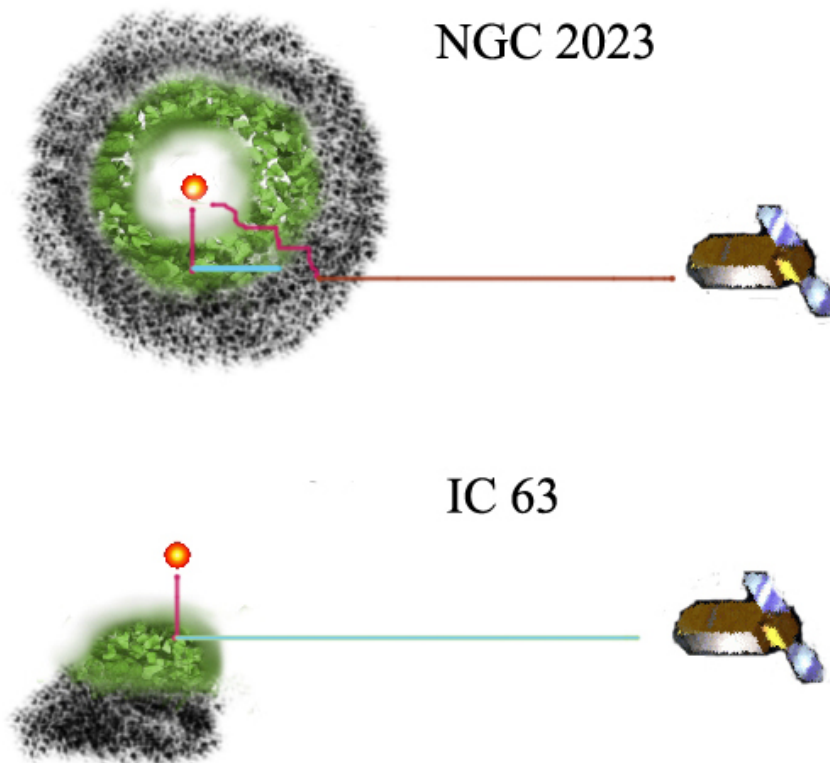
Figure 5.6 A cartoon cross-sectional view of the geometrical effects that may explain our non-detection of H_2 in NGC 2023 and NGC 7023. The central stars of these objects are imbedded in the nebular gas and dust which they excite. The fluorescing region (shown in green) may be behind an extended envelope of cold gas and dust (shown in gray) that absorbs the emission from the inner regions. A contrasting picture is presented for the "right angle" geometry most likely present where we do detect the far-UV H_2 emission, IC 63.

Similar conclusions can be reached if we assume that the optical depth in the absorption lines of molecular hydrogen in the outer nebular regions is high enough to absorb the photons emitted deeper in the cloud. This is complicated by the fact that absorption by H_2 out of the ground vibrational state is confined to wavelengths shorter than ≈ 1110 Å, whereas the emission bands continue to the end of the *FUSE* bandpass (1187 Å). An excited population of absorbing molecules resulting from multiply pumped H_2 would provide a higher density of discreet absorption lines in the $1110 - 1187$ Å region, and such an excited population has been observed towards HD 37903 (NGC 2023) by Meyer et al. (2001). However, the column densities in these excited lines are typically small ($N(H_2) < 10^{15}$ cm^{-2}) and we feel that absorption by dust is the more likely scenario.

The final possibility that we consider to explain the lack of H_2 emission in these *FUSE* observations is a poorly constrained coherent fluorescence process. In regions of high molecular hydrogen density ($n_H \sim 10^5$ cm^{-3}) such as NGC 2023 and NGC 7023, the absorbing transitions out of the ground and first excited rotational states ($j = 0$ and 1) of each vibrational band can have widths of several Ångstroms. If a molecule absorbs a UV photon away from the line center of the transition, the energy difference (ΔE) should be propagated through the re-emission coherently (Hummer, 1962). This coherent fluorescence predicts that lines fluoresced from damped transitions will be broader than lines fluoresced from saturated or optically thin transitions. Furthermore, the selection rules for H_2 state that *J* can change by at most $\pm$ 1 during an electronic transition, thus most of the molecules will remain in a low rotational state where such effects are important. Carrying this ΔE (which can be both positive and negative) through the resultant fluorescence will tend to broaden the emission lines. In dense media, this process could be be repeated several times before the photons escape.

An analogous process has been seen in the spectra of symbiotic stars (Birriel et al., 2000) and planetary nebulae (Arrieta and Torres-Peimbert, 2003). In this case, described as Raman scattering (Schmid, 1989) or optically thick fluorescence (Kastner, 1991), the atomic hydrogen column density is large enough that the Ly-β transition ($\lambda_0 = 1026$Å) can absorb photons emitted by the O VI doublet ($\lambda\lambda1032/38$). There is an energy shift from line center during the $1 - 3$ electronic transition. This energy shift is seen to propagate through the resultant emission spectrum in the optical; the Hα ($3 - 2$; $\lambda_0 = 6563$Å) emission

line is seen to have additional band structure at 6830 and 7088Å, consistent with O VI pumping (Schmid, 1989). This effect has also been seen in other lines populated by Lyman series absorption. In these cases, the atomic hydrogen is pumped by nearby transitions of He II (Birriel, 2004).

In a molecular envirnoment with a large number of absorbing transitions, this process will act as a boxcar smoothing of the H_2 emission lines, essentially eliminating the high resolution of $FUSE$. A boxcar smooth of sufficient width, applied to the parent emission spectrum, will result in a final output nebular spectrum that appears continuous. Figure 5.7 shows how this process would affect the nebular spectra. A parent emission spectrum is created by combining the scattered light component shown in Figure 5.4 with the H_2 model presented in Figure 5.5. A boxcar smooth is then applied to this original spectrum and the result is shown compared with the raw nebular spectrum (Figure 5.7).

The width of this smoothing will be governed by the widths of all of the absorbing transitions and the H_2 optical depth. This is not in conflict with the direct observation of the $\lambda\lambda 1578/1608$ Å feature seen by IUE and HUT. These two features are the superposition of several lines and continuum emission, but their overall line centers are sufficiently separated to be immune to a smoothing of a few Ångstroms. Our H_2 spectral synthesis code does not treat this redistribution process in a physically consistent way. It takes all of the absorbed photons, regardless of their actual wavelength and redistributes them to the line center during the subsequent emission. This study, as well as the unexpectedly wide H_2 lines observed in our studies of IC 63 and Orion (Chapters 2 and 3) have motivated us to work to develop a code that deals with this effect properly. The results of this modeling effort to resolve the unexpected results presented here are the subject of a future work (Chapter 6).

5.5 Summary

We have presented new far-UV nebular spectra of NGC 2023 and NGC 7023 obtained with $FUSE$, complimented by archival nebular and stellar spectra of these two reflection nebulae. Infrared observations of the rovibrational transitions of H_2 as well as the IUE and HUT data presented here suggest that these nebulae should show a strong signature
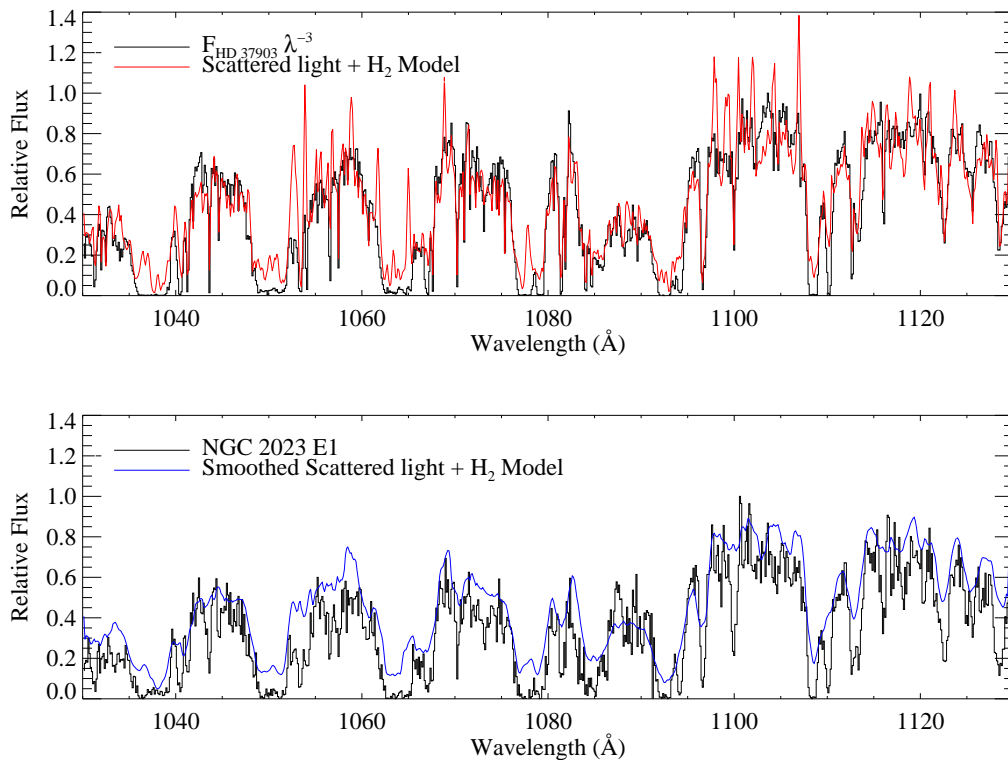
Figure 5.7 An example of how the coherent multiple fluorescence will affect the observed nebular spectrum. A parent spectrum is created by combining the scattered light with a model emission spectrum. A box car smooth corresponding to a resolution of 2.75 Å is then applied and compared with the observed nebular spectrum.

from fluorescent molecular hydrogen in the *FUSE* band. Surprisingly, we do not detect the expected fluorescence, only a dust scattered stellar continuum is observed. The contribution from scattered light is subtracted using the observed stellar spectra, but this procedure fails to reveal a H_2 emission signal in the *FUSE* data. The physical mechanism that gives rise to this apparent non-detection remains unknown, but we discuss several possibilities, including absorption within the nebula and a coherent fluorescence process that tends to smear out the closely spaced emission lines of H_2 at *FUSE* wavelengths. It is unclear which of these processes is playing the dominant role in NGC 2023 and NGC 7023, a combination of nebular absorption and coherent scattering seems most likely.

Chapter 6

Conclusions and Future Work

"A dog astride a fence, a dog astride a fence to the life!"   – Leo Tolstoy

6.1   Thesis Conclusions

This dissertation has examined the far-ultraviolet spectra of five gaseous nebulae. This work represents the first survey of molecular hydrogen and its relationship with interstellar dust and the ambient radiation field in diffuse clouds in the wavelength region between the Lyman limit and Lyman-α. To carry out this census, we have brought together data from orbital observatories including $FUSE$, HUT, IUE; sub-orbital sounding rockets (NASA/JHU 36.186, 36.198, and 36.208 UG); and ground based observatories (WIYN, 2MASS, KPNO, and NAOJ). In addition to a nebular spectral analysis, we have modified code to model the far-UV fluorescence of H_2 in these regions that takes into account the relevant local physical parameters.

Chapter 2 describes the ultraviolet study of IC 63, the first object in which continuum excited H_2 fluorescence was detected. That chapter analyzes the far-UV spectra from $FUSE$ and HUT and introduces the fluorescence model using a realistic exciting radiation field, flux calibrated by sounding rocket observations of γ Cassiopeia. Chapter 3 presents $FUSE$ spectroscopy of a diffuse region near Orion's Trapezium, showing a surprising H_2 emission signal from a seemingly empty portion of the sky. Chapter 4 brings together $FUSE$ and sounding rocket observations of IC 405, revealing a previously undetected pop-

ulation of molecular hydrogen and finding a high degree of differential dust extinction, calling into question the reliability of dust parameters inferred from the study of reflection nebulae. Chapter 5 completes the survey of emission/reflection nebulae with $FUSE$ observations of the well-studied objects NGC 2023 and NGC 7023. In contrast with the other objects in this thesis, previous observations, and theoretical predictions, these two nebulae show no evidence for UV fluorescence below Ly-α as we presently model it. A comparison of the $FUSE$ spectra of all five objects is shown in Figure 6.1.

The general conclusion of this dissertation is that dust scattered stellar continua and emission from H_2 dominate the far-ultraviolet spectra of photodissociation regions. This has been a long anticipated conclusion, but this work represents the first observational result that considers several nebulae that span multiple subclasses (i.e. - emission nebulae, star forming/H II regions, runaway stars, pure reflection nebulae). The relative contributions of the two components is seen to vary between objects and the observed emission lines are broader than one would expect from instrumental effects alone. At one end, cases where the star is clearly separated from the illuminated cloud (the "right angle" geometry of Chapter 5), fluorescent H_2 emission dominates the spectrum. Examples of this situation are IC 63 and the northern filament of IC 405. Conversely, nebulae in which the exciting star is embedded show little evidence for the emission lines below Ly-α, a dust scattered imprint of the central star is all that is seen. NGC 2023 and NGC 7023 are examples of these systems.

Far-UV spectra of two of the objects that clearly show H_2 emission, where the local physical conditions were known from previous studies at other wavelengths, enabled us to create and test models of the photo-excitation of H_2. These models found good agreement with the relative strengths of the lines across the ultraviolet bandpass, resolving the order of magnitude discrepancy between theory and observation in IC 63. The absolute flux predictions of these models tended to be off by factors between two and ten, but given uncertainties in distance, geometry, the clumping of nebular gas and dust, etc., we do not consider these disagreements to be unreasonable.
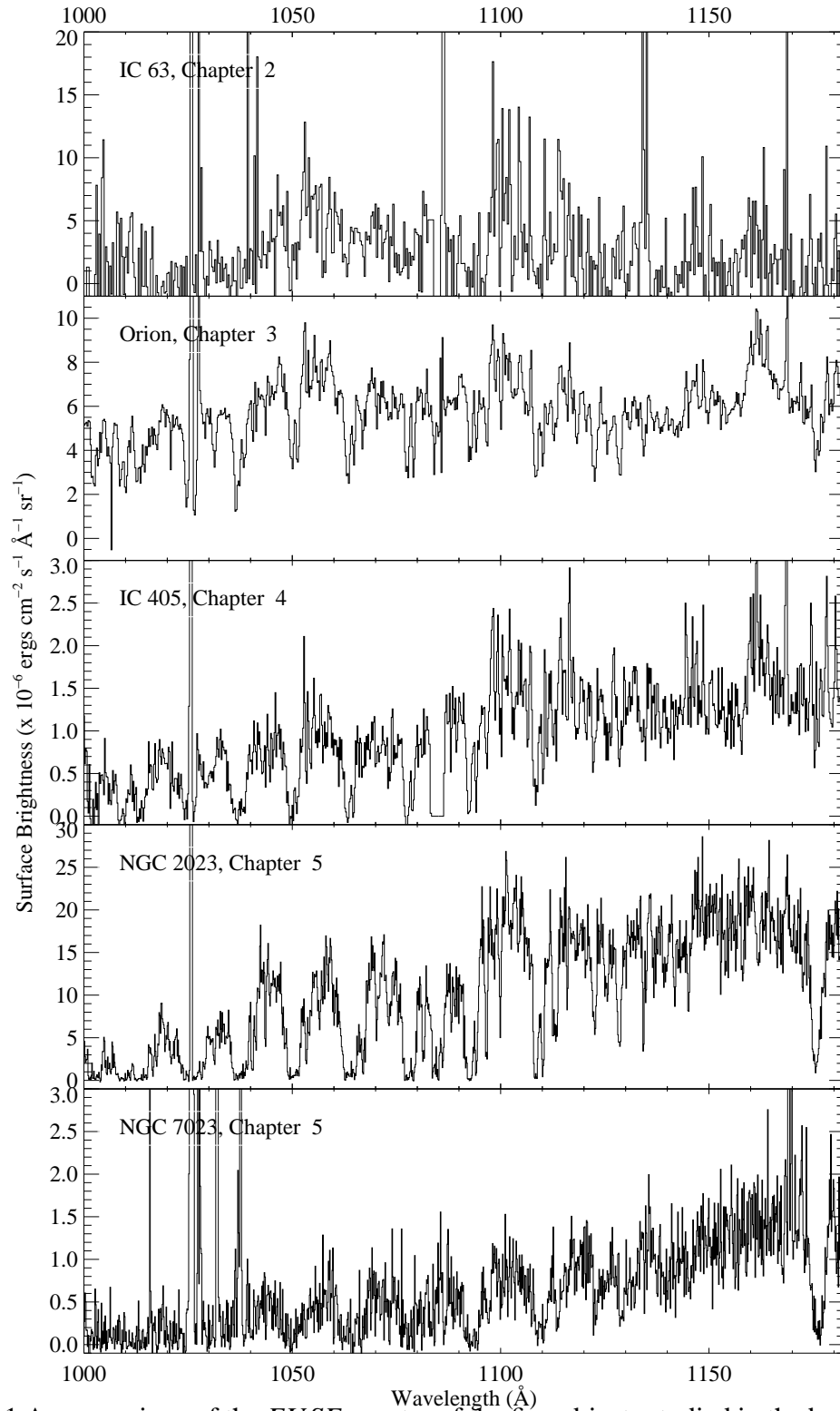
Figure 6.1 A comparison of the *FUSE* spectra of the five objects studied in the body of this dissertation. The signal was typically weak below 1000 Å.

The observed emission lines of H_2 are seen to be broader than our model predicts, a resolution of this issue is a topics of future work discussed below. We also anticipate that future modeling will shed light on the physical mechanism responsible for extinguishing the molecular hydrogen signal in NGC 2023 and NGC 7023.

6.2 Future Directions

6.2.1 Molecular Hydrogen Emission Model

One possibility suggested to explain the breadth of the observed H_2 emission lines is a coherent scattering process that redistributes the fluoresced energy depending on the width of the exciting transition. This can be more clearly understood by considering the fluorescence process as a whole. In sufficiently dense astrophysical regions (i.e. - the objects studied in this dissertation), the width of the absorbing transitions that populate the upper electronic states of the molecule ($B^1\Sigma_u^+$ and $C^1\Pi_u$) can be up to several Å. For instance, the (3 - 0) R(0) absorption line is centered on 1062.88 Å, but at column densities greater than $N(H_2) > 10^{19}$ cm^{-2}, photons with $\lambda \pm 0.5$ Å can also be absorbed by this transition. If this $\Delta\lambda$ is carried through the subsequent emission, the resultant emission spectrum will tend to be broadened in proportion to the absorption width. As demonstrated in Chapter 5, this effect can smear out the *FUSE* band H_2 emission lines completely. The emission lines below 1200 Å are so closely spaced that adding power away from line center will cause sufficient overlap to blend the individual lines together. We will work to include this effect into the model developed for comparison with the observations described in this thesis. Dealing with finite width of the absorbing transition in a physically consistent manner is the next step in the creation of an emission analog to the *H_2ools* absorption template library.

6.2.2 Ly-α Pumped H_2 in Planetary Nebulae

One natural extension to a study of the far-UV spectra of diffuse nebulae is to bring additional subclasses into the survey. This project has been started with a *FUSE* guest in-
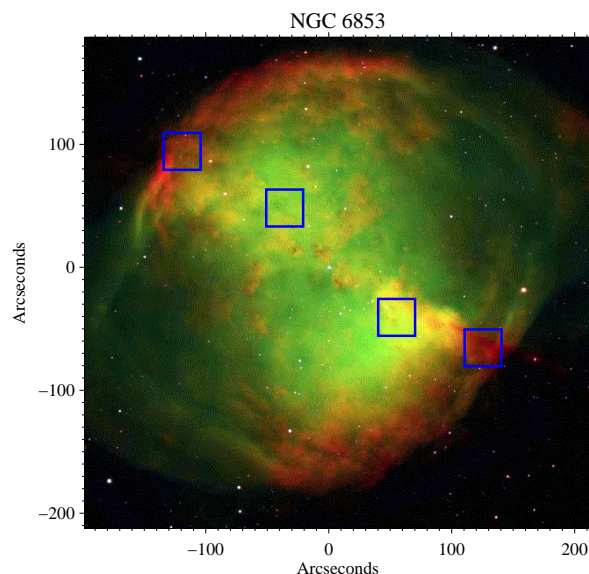
Figure 6.2 Optical image of the Dumbbell Nebula (M 27/NGC 6853) taken with the Very Large Telescope. Overlaid are projections of the *FUSE* LWRS aperture where we have acquired nebular spectra.

vestigator program to search for far-UV fluorescence in planetary nebulae (PNe). As in the case of reflection nebulae, there has been debate for a number of years about the excitation mechanism for the near-IR H_2 emission lines seen in these objects. Again, far-UV observations can distinguish between shock and photo-excitation of the molecular gas phase in the envelopes of these objects. The Dumbbell (M 27, NGC 6853; Figure 6.2) and Helix (NGC 7293) nebulae were the targets of our Cycle 5 proposal. The observations of the Dumbbell have been made, and a sample of the data is shown in Figure 6.3. The spectrum is from the inner region of the nebula and shows strong emission from He II, indicative of gas highly ionized by the hot central star. Additionally, C III and recombination lines of C II are observed to be strong in the inner region.

Figure 6.4 shows portions of the LiF 1b and LiF 2a *FUSE* spectra from the inner southwestern pointing in M27. In addition to the high-excitation emission lines of C II and C III, we have identified fluorescent H_2 emission lines at *FUSE* wavelengths for the first time in a planetary nebula. These lines are excited by nebular Ly-α photons. At first, this
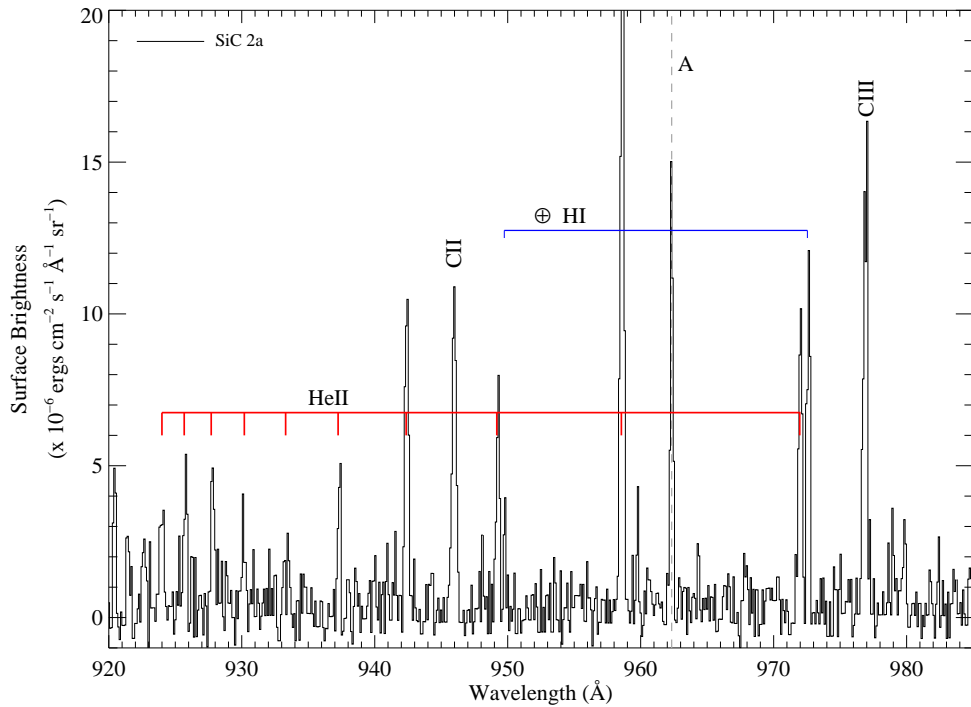
Figure 6.3 A portion of the *FUSE* spectra of M 27. This spectrum of the inner southwestern pointing shows highly ionized gas traced by He II, C II, and C III emission lines. The feature near labeled "A" near 962.4 Å may be due to O III, but the identification is uncertain.

result seemed surprising considering that the central star has an effective temperature of $\approx$110,000 K, producing a strong far-UV radiation field in the 912 – 1110 Å range usually associated with H_2 absorption. It was only after the realization that the majority of the photons emitted below the Lyman limit end up producing Ly-α photons (Spitzer, 1978) did this result become clear. A stellar model from the Rauch library (Rauch et al., 1994) was created using the parameters determined by McCandliss et al. (2005 - in preparation). Integrating this model (Figure 6.5) over the relevant wavelength intervals shows that there are approximately 14 times more photons available in the Lyman continuum than in the 912 – 1110 Å window. This observation, coupled with the fact that the majority of those photons are concentrated into line emission, explains why Ly-α excitation dominates in PNe.

We searched the *FUSE* archive for other PNe that exhibit this line-pumped fluorescence, finding NGC 3132 to be the only other candidate with an obvious H_2 signature. The
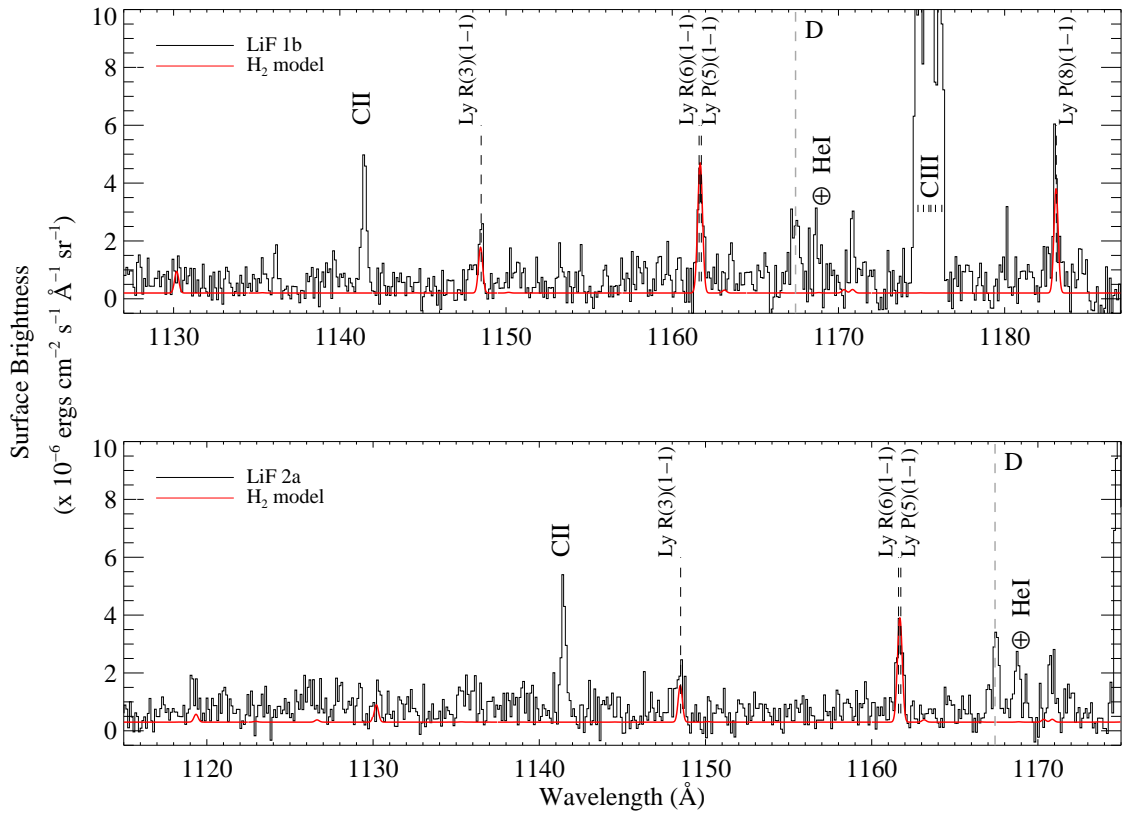
80

Figure 6.4 Far-UV H_2 emission is observed for the first time M 27. This is the first detection of molecular emission below 1200 Å in a planetary nebula. The H_2 is photo-excited by nebular Ly-α.

NGC 3132 observations were made through the MDRS aperture, with less than 10 ksec of observing time. The emission signal was weak. However, an archival HUT spectrum of the object showed that fluorescent H_2 was the dominant spectral characteristic at wavelengths longer than Ly-α (Figure 6.6). An emission model was created using the nebular parameters derived by McCandliss et al. (2005) for M 27 (T(H_2) = 2400 K and b = 5 km s^{-1}). We find an emitting column density of N(H_2) = 2.0 x 10^{17} cm^{-2}. The model is shown in red in Figure 6.4, with the individual emission lines labeled. The ability for the hydrogen molecules to be excited by Ly-α is an interesting consequence of the high gas temperature.
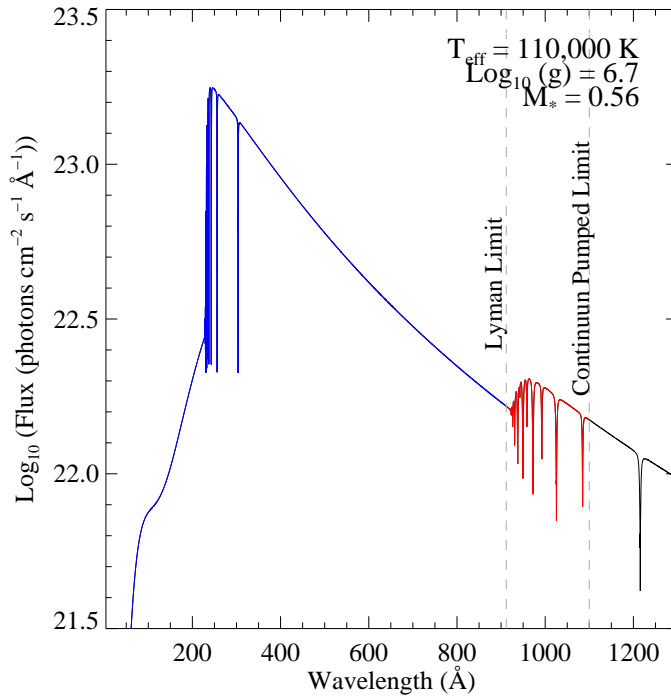
Figure 6.5 A synthetic spectrum of the central star of M 27 illustrates why Ly-α pumped H$_2$ overwhelms fluorescence by the stellar continuum. The majority of the photons emitted by the central star below the Lyman limit will lead to the production of Ly-α photons. There are approximately 14 times more photons emitted below the Lyman limit than in the 912-1110 Å region.

A nebular Ly-α line with a FWHM of 0.33 Å is coincident with the Lyman band transitions $P(5)$ $(1-2)$ and $R(6)$ $(1-2)$. Such excited rovibrational states cannot be maintained by H$_2$ at temperatures found in the diffuse ISM (T(H$_2$) = 80 K, predominately populating $J = 0$, 1 and $v = 0$). Such warm molecular gas suggests an additional physical process exciting the nebular material. The conclusion of McCandliss et al. (2005) is that shocks are responsible for the elevated gas temperatures found in M 27.

We then compared similar model (using a larger column density) to the HUT spectrum of NGC 3132 (Figure 6.6). The $(1-3)$ transitions are overpredicted by the model, but we feel that this is mostly due to poor continuum placement in the region near strong

geocoronal airglow. A more detailed analysis of PNe is beyond the scope of this thesis, but in the future we plan to use the photo-ionization code CLOUDY (Shaw et al., 2005) to better interpret these observations and determine the three-dimensional structure of these objects (Lupu et al. 2006 - in preparation). Unfortunately, observation of the Helix were not carried out before the most recent reaction wheel failure, but we anticipate these data as *FUSE*'s sky coverage returns.
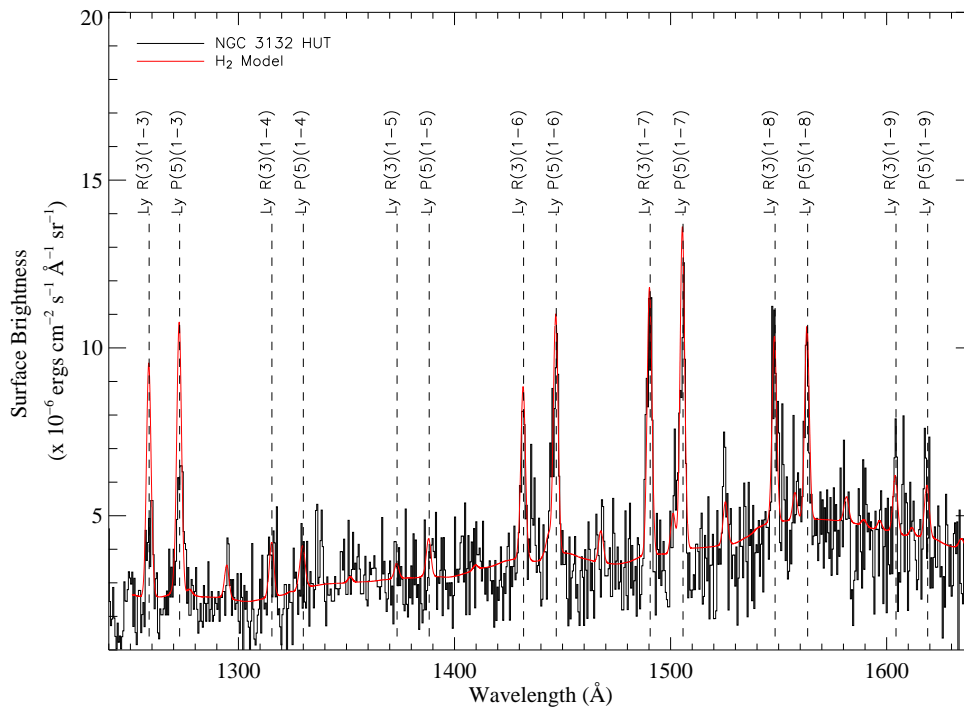
Figure 6.6 The HUT spectrum of NGC 3132 shows Ly-α pumped H_2 dominating the nebular spectrum between 1200 and 1700 Å.

6.2.3   A PAH Study of IC 405 with *Spitzer Space Telescope* - IRS

Emission from Polycyclic Aromatic Hydrocarbons (PAHs) has been found to be ubiquitous in the mid-infrared spectra (3 – 20 μm) of reflection nebulae and H II regions (van Dishoeck, 2004; Werner et al., 2004; Peeters et al., 2004). PAH emission is seen as broad

bands in the *Spitzer*-IRS wavelength range, with lines complexes centered on 6.2, 7.7, 8.6, 11.3, and 12.7 μm. These features are attributed to C–C and C–H bending and stretching modes in PAHs with a few tens to a few hundred carbon atoms (van Dishoeck, 2004). An analysis of the *Spitzer* spectrum of NGC 7023, shown in Figure 6.7, is given by Werner et al. (2004) and Peeters et al. (2004). Werner et al. (2004) find the strength of the PAH emission features to vary with position within the nebula and detect strong PAH emission in a filament that is bright in the near-IR vibrational lines of H_2 (Takami et al., 2000). They also detect new unidentified mid-IR emission features at 6.7, 10.1, 15.8, 17.4, and 19.0 μm that may be attributed to a combination of C–H out-of-plane bending modes, C–C–C bending modes, and vibrational transitions of the C_{60} molecule (Werner et al., 2004). Peeters et al. (2004), comparing $15 - 21 \mu$m spectra obtained by *Spitzer* with observations made by *ISO* show that the PAH emission varies from object to object. They attribute these spectral changes to variations in the PAH population.
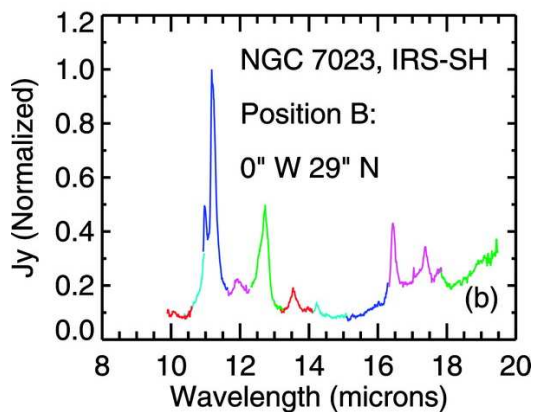

Figure 6.7 The *Spitzer* IRS spectrum of one position in NGC 7023 from Werner et al. (2004), the different colors represent different orders of dispersed light. The mid-IR spectrum is dominated by PAH emission features.

Variations in the spectral features of PAHs are indicative of the physical conditions present in the region. The C–H emission features at 3.3 and 11.2 μm are found to be well correlated over a range of physical conditions, however the relative strengths of the C–H and C–C features are observed to vary with environment (van Dishoeck, 2004). The ratio of a C–H and a C–C feature (11.2/6.2 μm for example) can be a diagnostic of the density

of a region and the ionization state of the PAHs. Additionally, there is debate about the ability of small PAHs to survive in intense UV radiation fields (Verstraete et al., 2001; van Dishoeck, 2004). Verstraete et al. (2001) have found that PAHs have a larger minimum size when exposed to a harder radiation field. The modeling results are uncertain, but it appears that this is seen as a decrease in the relative strength of the 8.6 μm feature, presumably due to photodistruction or ionization of the carrier. We will use the unique spectral coverage of *Spitzer* to investigate potential environmental dependence of these lines by comparing infrared spectra (IRS) and images (IRAC) of NGC 7023 with those of IC 405. If an unusual PAH spectrum is observed in IC 405, it could suggest a new photoluminescence process is causing the blue S/F$_\star$ described in Chapter 4.

6.2.4   IC 405 as a Local Starburst Laboratory: *Spitzer* - MIPS and *GALEX* Photometry

Dust reprocesses the UV continuum of HD 34078, converting it into thermal emission in the far-IR. MIPS scans of IC 405 enable an assessment of the variation in dust temperature throughout the region. The clumpy nature of the gas and dust in IC 405 produce a high degree of differential extinction within the nebula (Chapter 4), and determining the distribution of dust temperatures may provide a better indication of the local radiation field. The differential extinction effects observed in IC 405 are reminiscent of the attenuation characteristics observed in starburst galaxies (Calzetti 1997; Chapter 4) . It is common to use the summed infrared flux and the slope of the ultraviolet continuum (β) to correct for dust attenuation in starburst galaxies. Meurer et al. (1999) present the infrared excess-ultraviolet slope relation (IRX-β, Figure 6.8) for a sample of local starbursts. A comparison of the MIPS scans with proposed *GALEX* observations of IC 405 will allow us to create an IRX-β relation for the individual nebular filaments, testing the universality of the IRX-β relation determined by Meurer et al. (1999). A detailed study of the individual filaments is made possible by the high-resolution of the MIPS instrument. These *Spitzer* data will enable us to further explore the assertion that IC 405 is a nearby laboratory in which to study processes that operate on global scales in starburst galaxies.
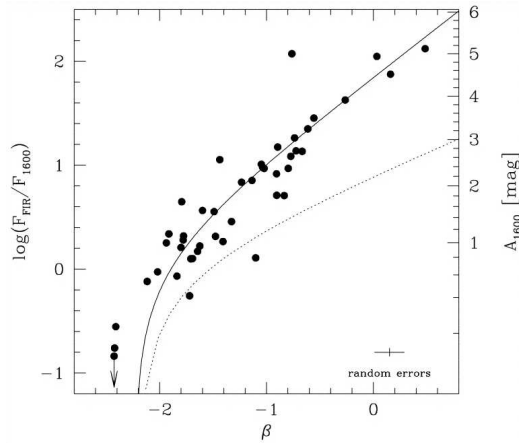
Figure 6.8 An example of the IRX-β relation from Meurer et al. (1999).

6.2.5 NASA/JHU 36.220 UG: Sounding Rocket Observations of Orion

Due to the brightness of the Trapezium stars, *FUSE* has been unable to observe near the Orion Nebula (with the exception of the observations presented in Chapter 3). Thus, no spectra of the central stars have been obtained at wavelengths less than 1150 Å since *Copernicus*, and no observations of the the surrounding nebula at these wavelengths have ever been made. With these constraints in mind, the Trapezium has been chosen as the second target of the LIDOS instrument described briefly in Chapter 2 and more extensively in the Appendix. Figure 6.9 shows a page from the mission planning documentation that describes the observing strategy. We will come to target on the Orion Bar with the MCP high-voltage on to observe emission from nebular gas and dust. The nebular observation is scheduled first to ensure that minimum success can be achieved without the operation of the command uplink system (for a more detailed description, see the Appendix). Following the MCP observation, the high-voltage will be turned off by a ground-based operator and a pointing offset will be executed to orient the spectrograph slit on the θ^1 Ori system. CCD observations of this young stellar system will provide spectroscopy with a resolution of 2 - 3 Å over the far-UV (900 - 1590 Å) bandpass of the instrument.
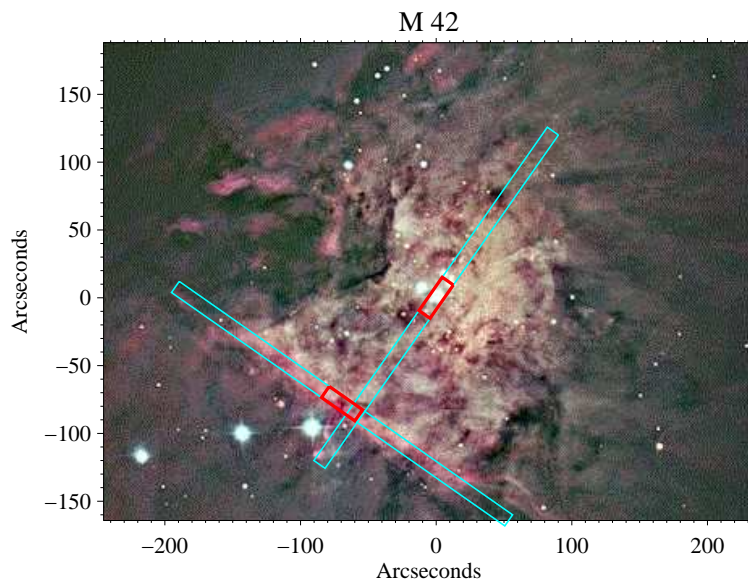
Figure 1: The Great Nebula in Orion, from the Anglo-Australian Telescope (AAT).

Targets; Pointings and Roll Angles

Pointing	Object	RA (2000) (^{h} ^{m} ^{s})	δ (2000) (° ′ ″)	Position Angles (relative to North-South)	Est. MCP Ct. rate (Hz) 5 cm^2-Å
1	M42 (Bar)	05 35 22.00	-05 24 36.0	θ = 55°	1.5 x 10^3
2	θ^1 Ori C	05 35 16.47	-05 23 23.1	θ = -35°	3.1 x 10^5

Figure 6.9 Observational plan for the second flight of the LIDOS instrument, NASA/JHU 36.220 UG has a tentative launch date of 2006 February.

5

Appendix A

Instrumentation and Rocketry

"How much disbelief, collectively, must be suspended,
to allow for tourism?"   – Dave Eggers

A.1   Long-slit Dual Order Imaging Spectrograph

This appendix describes a large portion of the supporting work that went into producing the science results discussed in the body of this dissertation. It focuses on the NASA/JHU 36.208 UG mission that contributed to the study of IC 63 presented in Chapter 2. This section describes the design, calibration, and flight of the Long-slit Dual Order Imaging Spectrograph (LIDOS, Figure A.1). Much of the calibration and flight procedures are similar to those performed for the instrument flown on the 36.198 UG mission, described in Chapter 4.

The LIDOS instrument (McCandliss et al., 2003) was designed to study faint nebulosity under an influence of the ultraviolet (UV) radiation field produced by hot stars. Such studies have been traditionally hampered by the inability of space-based observatories to work near bright stars. These observatories (such as HST and $FUSE$) were designed to be sensitive to the faint light of distant objects, and as a consequence, have stringent bright target limits. LIDOS works around this constraint by employing two complementary UV-sensitive detectors to cover the large dynamic range in flux required to perform spectroscopy of bright stars as well as the surrounding material. The long-slit configuration of the instrument pro-

vides spatial information giving another advantage over what is presently available in the ultraviolet spectral regime.

The interaction between hot stars and their surroundings give rise to photodissociation regions (PDRs, a number of which are studied in this thesis). PDRs are found in several classes of astronomical objects. Massive stars that ionize their natal cocoon create H II regions, after their inner regions are cleared out, dust scattered stellar light forms reflection nebulae, and planetary nebulae are dying stars that are ionizing their ejected stellar envelopes. PDRs exist in all three objects, where the intense UV radiation field of a hot star (or stars) interacts with the surrounding atomic/molecular gas and dust. In addition to these local examples of high contrast regions, external galaxies show a similar structure. Starburst galaxies have a bright core and star clusters that are surrounded by diffuse blue interarm emission. The far-UV bandpass is a very rich spectral window, containing the molecular and atomic signatures of H_2, CO, H I, He II, C I – C IV, N I – N V, O I, O III, O V, O VI, S I – S VI, Ar I, and Ar II among others, valuable for probing the composition over a wide range of energetic environments.

The instrument is a 600 mm diameter Rowland Circle spectrograph. LIDOS achieves a large dynamic range in flux by using a toroidally figured holographically ruled diffraction grating that provides astigmatism corrections to both the plus and minus first order light. This grating is discussed in more detail in § A.2.1. Two complementary detectors record light from each diffracted order, and it is this complementarity that permits the large dynamic range of the LIDOS instrument. Light in the positive order is recorded by a δ-doped SITe ST-001A CCD that is sensitive to objects brighter than $\approx 3 \times 10^{-11}$ ergs cm^{-2} s^{-1} Å^{-1}. Figure A.2 shows a laboratory first light image from the detector. The CCD has an 1133×330 format with 24 μm square pixels. The chip has a quantum efficiency of $\sim 45\%$ in the far-UV bandpass (the LIDOS CCD channel covers 900 – 1590 Å, see Figure A.4). A stainless steel (316 SS) flange is used to attach the detector to the body of the spectrograph, and coupled to the flange is a two-phase cooling system to reduce dark noise. A copper heatsink is attached to the flange and is cooled by a Joule-Thomson system that uses high pressure (3000 psi) argon.
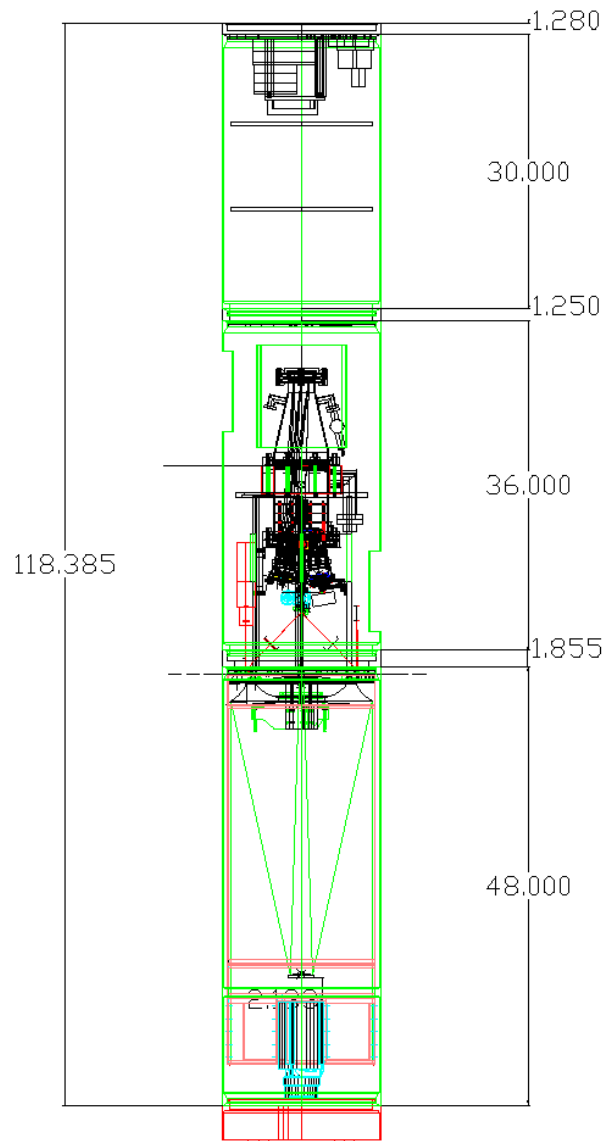
Figure A.1 A schematic of the experiment section taken from the 36.208 mission documentation. The dimensions are in inches. From bottom to top: Telescope section, Spectrograph section, Avionics section. The Telescope and Spectrograph sections are evacuated. *Figure by Stephan McCandliss.*
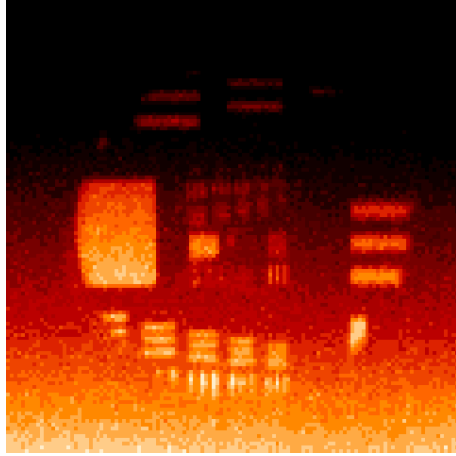
Figure A.2 Laboratory first light image from the LIDOS CCD. The calibration lamp described in this appendix used an Air Force Test Pattern to create this image in Ly-α.

A thermoelectric cooler is embedded in the copper heatsink, and it brings the chip to temperatures below 273 K. Two hermetically sealed 25-pin subminiture D-type connectors bring the data to the CCD headboard, and the related detector electronics are located outside of the evacuated section.

Our detection capability is extended to faint objects and diffuse emission (3×10^{-14} – 3×10^{-11} ergs cm^{-2} s^{-1} Å^{-1}) by using a microchannel plate (MCP) detector to measure the light in the negative order. The MCP is a windowless Z-stack readout by a double delay-line anode produced by Sensor Sciences, located in Berkeley. This detector was originally flown on a JHU rocket to observe the UV spectrum of Comet Hale-Bopp (NASA/JHU 36.156 UG; McPhate et al. 1999) and was refurbished for integration into the LIDOS instrument. It covers the wavelength range 930 – 1680 Å, essentially the entire range spanned by the electronic emission lines of H$_2$. The MCP uses a CsI photocathode to achieve a QE that ranges from 15-45% in this bandpass. The wavelength calibration is shown in Figure A.3. The detector format is 30 mm $\times$ 12 mm, and the mounting flange is similar to the one described for the CCD. The MCP has a preamplifier located inside the spectrograph section and additional electronics in the avionics section. The spectrograph focus procedure is shown graphically in Figure A.5.

The entrance aperture of the spectrograph is defined by a long-slit (10$''$ $\times$ 300$''$ pro-
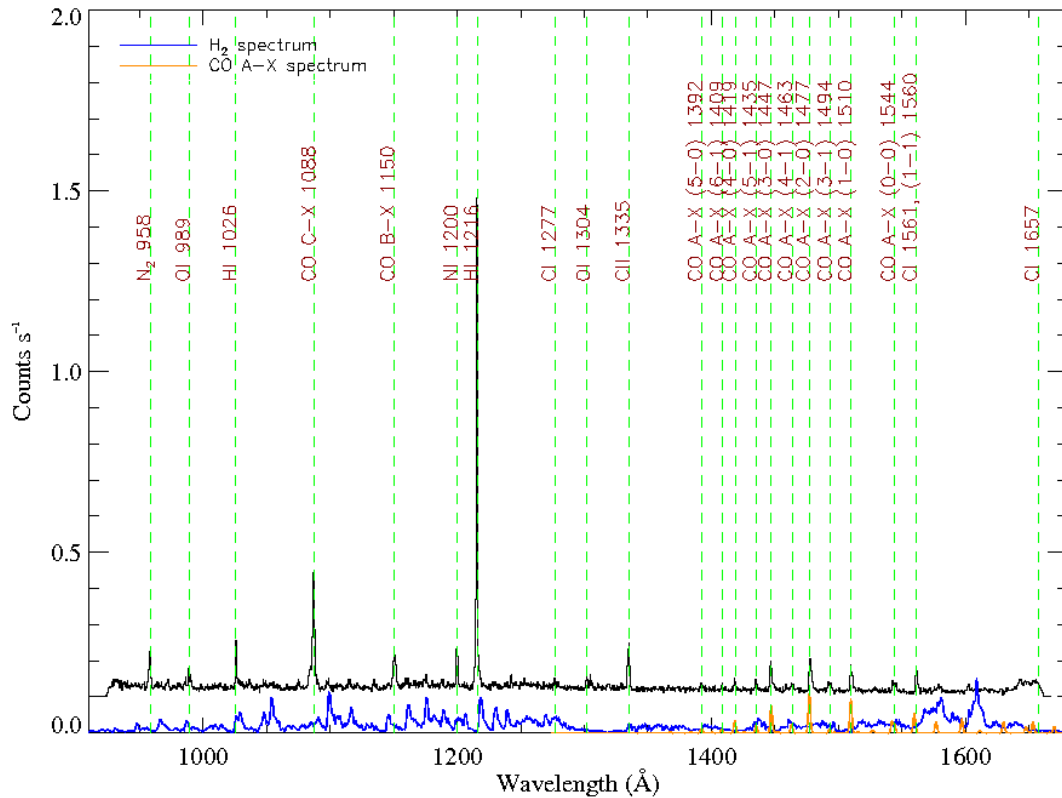
Figure A.3 The wavelength solution for the LIDOS MCP channel prior to 36.208 integration and testing. This spectrum was created using the calibration lamp described in § A.3 and fit with an 8th-order polynomial. Prominent atomic and molecular lines are labeled.

jected on the sky) etched into a mirrored slit-jaw. The slitjaw redirects the light not entering the spectrograph to a camera that transmits the target field ($20'$ field-of-view) to the ground during the flight. Light is focused at the entrance aperture of the spectrograph by a telescope whose mirrors are coated with SiC in order to increase the far-UV throughput. The telescope is a 40 cm diameter f/15.7 Dall-Kirkham, an updated version of the Faint Object Telescope (FOT) that has been flown by the JHU Rocket Group for many years (see references in Chapter 4). The FOT has a plate scale of $33''\text{mm}^{-1}$. The telescope is housed within an invar heat shield with a spider that holds both the secondary mirror mount and an axially located startracker. The startracker is aligned with the telescope optical axis, and
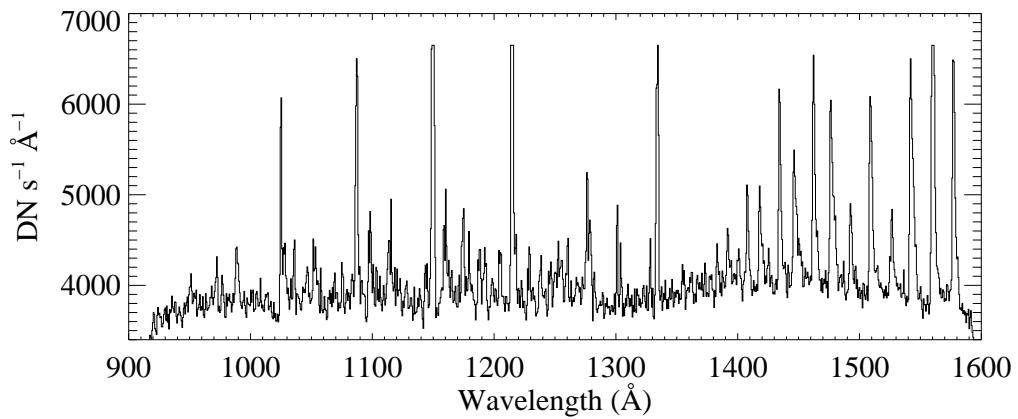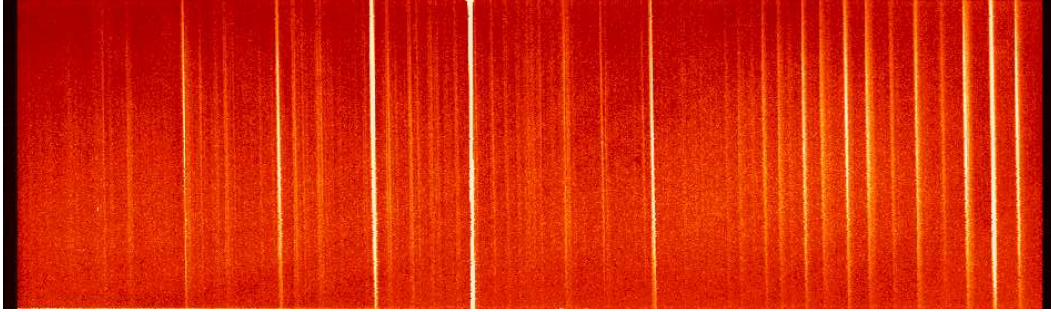
93

Figure A.4 Spectral image obtained with calibration lamp mounted directly at the spectrograph enterance aperture. The spectrum extracted from a six pixel range ($y_{pix} = 198 - 204$) near the center of the detector is shown below. The brightest lines are produced by H I, C II, O I, and CO.

is used to acquire the target field. Fine pointing adjustments are made using the transmitted camera image, and the Attitude Control System (ACS). The details of ACS and field operations are given in § A.4.
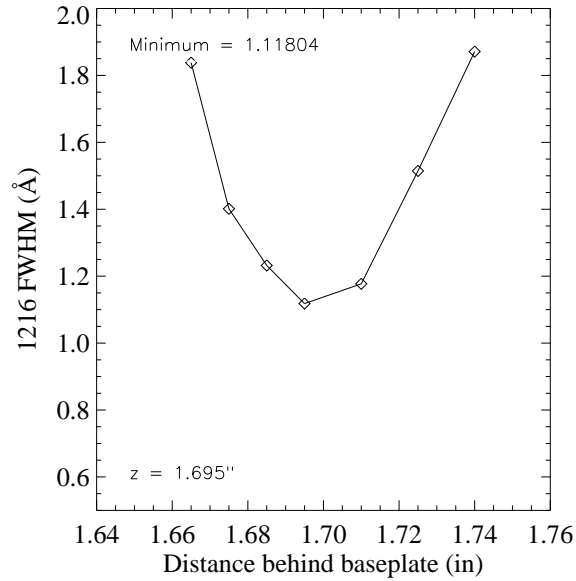

Figure A.5 The determination of best focus position was made by minimizing the FWHM of the Lyman-α line measure in the laboratory. LIDOS was measured to have a spectral resolution of slightly greater than 1 Å.

A.2 Telescope and Spectrograph Calibration

Absolute calibration is often essential to quantitative astronomical measurements. Instruments developed by the JHU Rocket Group are characterized in the Calibration and Test Equipment facility (CTE; Fastie and Kerr, 1975; Figure A.6). With this calibration facility we can measure mirror reflectivities, diffraction grating efficiencies, and detector quantum efficiencies (Figures A.7 and A.8) at vacuum ultraviolet wavelengths, from 584 – 3000 Å. The facility uses a combination of lamps and evacuated monochromators to produce incident beams for these studies. The emission line strengths are measured by a host of photomultiplier tubes (PMTs) and MCPs located on movable stages in separate vacuum chambers.
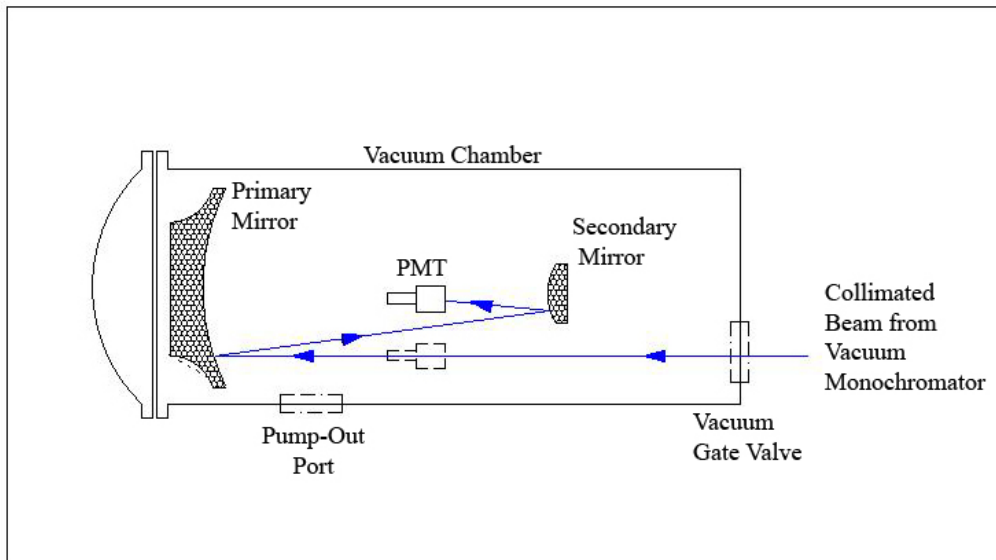
Figure A.6 A schematic representation of the telescope mirror reflectivity procedure carried out in the CTE. Spectrograph QEs and diffraction grating efficiencies are measured using a similar process.

Photomultiplier tubes used include a 542F-tube with a sapphire window and a CsTe cathode ($1600 \leq \lambda \leq 3000$ Å), a 542G-tube with a LiF window and a CsI cathode ($1050 \leq \lambda \leq 1600$ Å), and a 541E-tube that employs a sodium salicylate scintillator to downconvert far-UV photons to the visible (for $\lambda \leq 1050$ Å). These tubes are positioned to measure the intensity of the light incident on the sample and then moved to compare that with the intensity of the light reflected from the sample. Between each measurement, the chamber is closed off from the monochromator and a dark value is measured and subtracted from the signal. The standard deviations of the incident, reflected, and dark measurements are recorded and used in the error analysis.
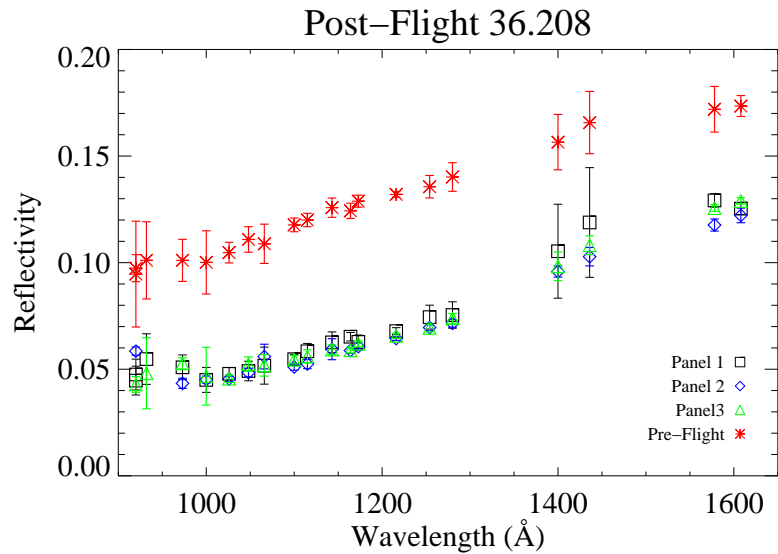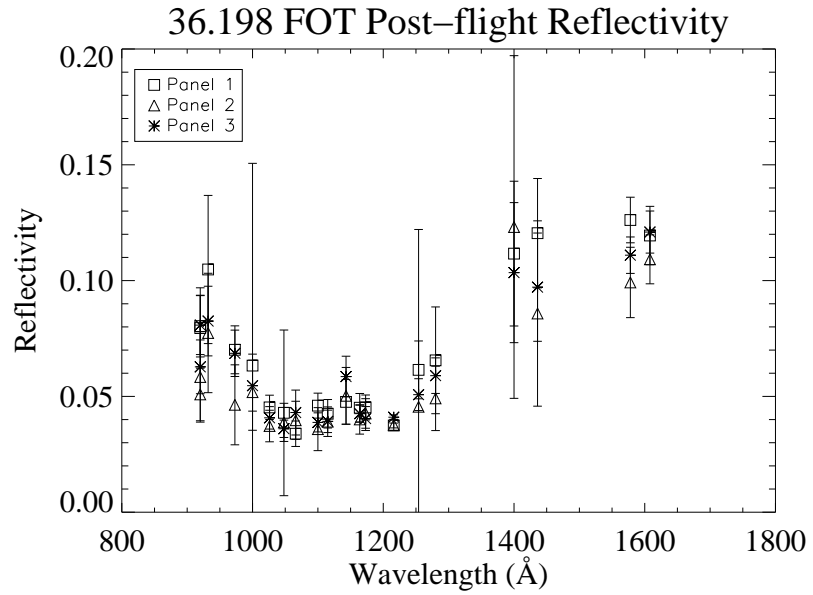
Figure A.7 Telescope reflectivities for two of the rocket flights described in this dissertation, 36.198 and 36.208. Similar degradations in reflectivity are seen in both post-launch measurements. We believe this loss is caused by frequent vacuum cycling during integration and testing. Errors are smaller in the 36.208 measurements due to improvements in the CTE monochomator.

97
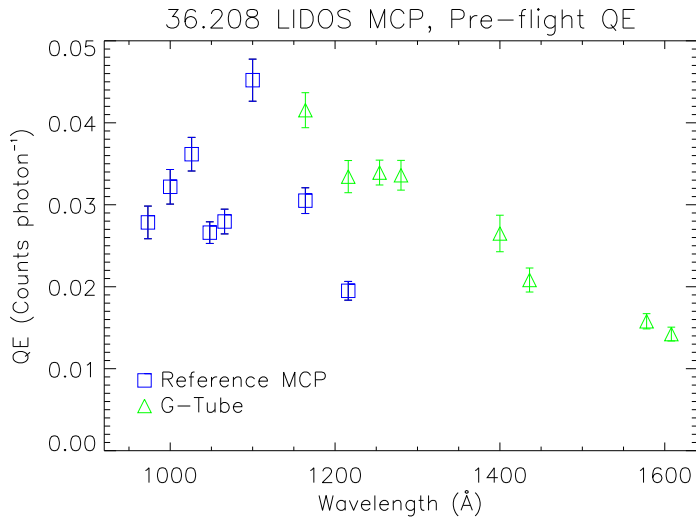
Figure A.8 LIDOS MCP channel quantum efficiency measured prior to 36.208 field operations. Unlike the telescope reflectivities, spectrograph QEs are seen to be very stable.

A.2.1 Hardware Characterization and Calibration

We also use the CTE to characterize hardware components before integrating them in to a system, such as the FOT or LIDOS. This subsection describes two pieces of hardware that we measured in preparation for the 36.208 flight. The first is the concave toroidal diffraction grating used on LIDOS. This grating was purchased from the French firm Jobin-Yvon and is made of chemical vapor deposit (CVD) SiC. The grating was ruled holographically with symmetric, trapezoidal grooves. It is the symmetry of the diffraction grating that is essential to the normal incidence ($\alpha = 0$) dual order design. Astigmatism must be minimized in order to achieve good spatial resolution and this has been accomplished by making the radius of curvature slightly smaller in the direction perpendicular to the dispersion direction. The effect of this toroidal shape causes the tangential and sagittal foci to occur at the same wavelength (LIDOS uses ~ 1275 Å as the stigmatic wavelength). The grating absolute grating reflectivities shown in Figure A.9 can be turned in to absolute groove efficiencies, which is the subject of future work.

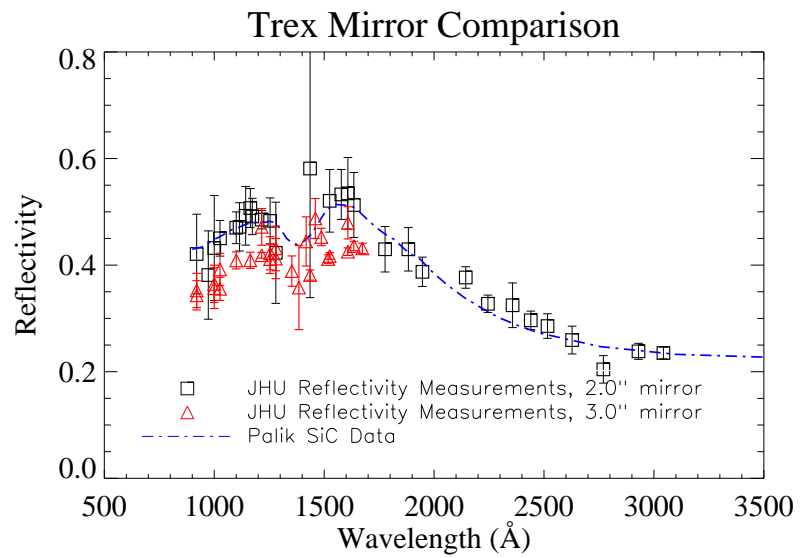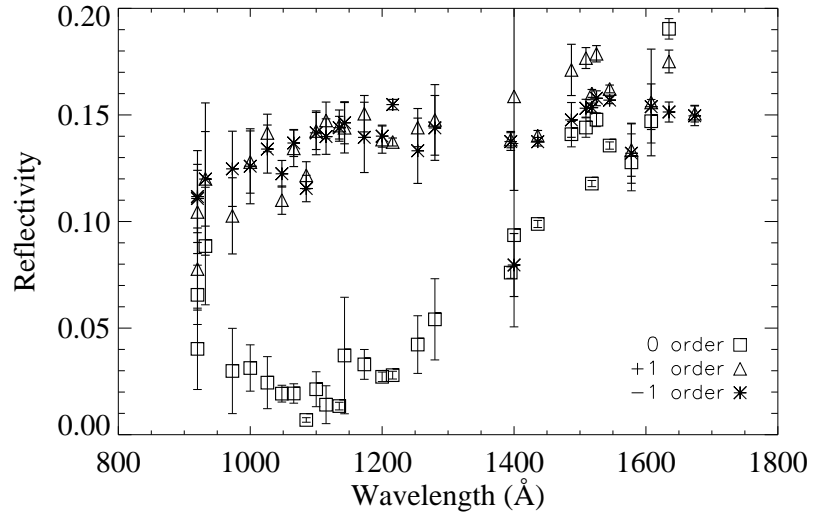Figure A.9 Dual order diffraction grating and experimental secondary mirror reflectivities measured in the CTE.

The second hardware test we conducted in preparation for the 36.208 mission was a new secondary mirror. The novel process of chemical vapor composite (CVC) has been used by Kauai-based Trex Enterprises to create pure SiC optics for a fraction of the cost of the CVD process. We were given a sample of a 2-inch diameter flat mirror in order to test the UV reflectivity of the material. The results are shown in the right panel of Figure A.9 for wavelengths $900 - 3000$ Å. We found that original flat mirror was a match to the theoretical curve computed from the optical constants of Palik (1985). Additionally, this material was robust and lightweight, ideal for sounding rocket applications. Unfortunately, the UV-reflectance of the CVC substrate was not repeatable, and while we did have a CVC secondary mirror for the FOT fabricated, we opted to fly the existing SiC coated secondary.

A.3   Far-Ultraviolet Calibration Lamps

Astronomers have long relied on emission line and continuum calibration spectra to improve science return at optical wavelengths. Emission line spectra provide wavelength solutions and continuum spectra allow for the construction of detector flat-field maps that can be used to correct for instrumental non-uniformities during the data reduction process. The most common method of obtaining such spectra is through the use of lamps designed for each application. Calibration spectra in the windowless ultraviolet are challenging to obtain as emission line sources generally require operating pressures of ≈ 1 Torr (McCandliss et al. 2000), several orders of magnitude higher than the operating pressure ($\approx 10^{-5}$ Torr) of MCP detectors commonly used in the far-UV bandpass. Continuum sources are even harder to come by as most sources are dominated by line emission. This section reports on the development of a lamp that serves as both an emission line and continuum source, and operates at the ambient vacuum necessary for far-UV instrumentation.

A.3.1   Lamp Mechanical Structure and Operation

We have found that electron impact sources can produce strong far-UV emission line and continuum spectra in high vacuum environments ($P \geq 10^{-8}$ Torr). The line spectrum is produced as free electrons collide with the residual gas in the vacuum. The continuum

100

spectrum is produced by bremsstrahlung as the electrons collide with a thick tungsten target (Bayard and Alpert 1950). In practice, current flowing through a thin tungsten ribbon filament produces a source of free electrons that are accelerated towards the target by an applied voltage. The filament is typically run at 2 – 4 Amps, and tests have been performed with target biases ranging from 20 – 2000 Volts. Unlike traditional electron impact experiments (Ajello et al. 1991; James et al. 1997), the geometry of our lamp does not produce a mono-energetic environment. Our results indicate that our lamp approximates previous mono-energetic experiments when dividing our operating voltage by a factor between four and five.

The lamp consists of a mini-conflat flange cube into which the filament and target are mounted. The target, a 3/32 in diameter tungsten welding rod, is mounted perpendicular to the the filament in order to maximize electron transfer efficiency. The lamp has a window for visual inspection and filament temperature determination during operation. In the current test configuration, the lamp directly illuminates the slit jaw of a long-slit Rowland Circle spectrograph that was the primary science instrument on three previous sounding rocket flights (NASA/JHU 36.136, 36.186, and 36.198, see Burgh et al. 2002 and this thesis). The spectrograph aperture is a narrow slit (25 μm), and uses a holographically ruled grating and MCP stack detector with a KBr photocathode, readout by a double-delay line anode (Chapter 4). All data presented here were obtained in this configuration with a spectral resolution of about 1 Å.

A.3.2 Emission Characteristics

A typical emission line spectrum shows atomic hydrogen, atomic and molecular nitrogen, and atomic oxygen; a combination of atmospheric constituents and water vapor. The spectrum can be altered by the introduction of different species into the lamp. The emission lines present and their strength will depend on the gas and the quality of the vacuum. A gas leak valve on our testbed allows us to introduce different species for a richer wavelength coverage and absolute calibration studies using electron impact cross-sections, as described below. To date, electron impact spectra of H_2, HD, Ar, N_2, O_2, and CO_2 have been measured. Typically lines of H I Lyman-α, N I λ1200, N II λ1084, O I λ1304, O I λ989, and N_2
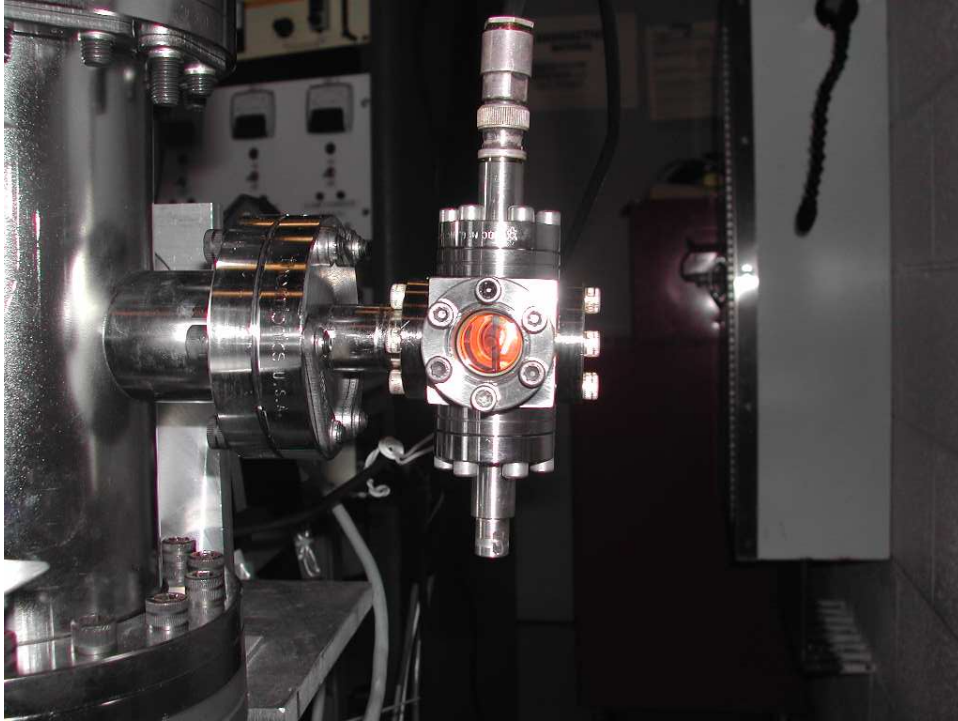
Figure A.10 Digital photograph of the electron-impact calibration lamp on the vacuum testbed at JHU. The tungsten target can be seen through the windowed port. For reference, the window has a diameter of 5/8 in.

(c$'_4$-X) 958 dominate, while Lyman-β, O I λ1152, N I λ1243, N I λ1135, C II λ1335, CO (B-X) 1150 and CO (C-X) 1088 are weaker. A complete list of the target species observed is listed in Table A.1.

The bremsstrahlung continuum spectrum is a strong function of electron emission current (i.e.- filament temperature) and target voltage. Emission current increases sharply as the filament temperature goes above > 1100 K. The dependence on operating pressure is much weaker than in the case of the emission lines, thus continuum/line contrast can be varied by changing the lamp pressure. This contrast can also be changed by increasing the target bias (see Figure A.11). The bremsstrahlung emission rises with bias where as the cross-sections for impact excitation of molecules typically rise to a peak at $50 - 100$ eV and then fall towards higher electron energies (Ajello et al. 1989; Ajello et al. 1991, James et al. 1997; Kanik et al. 1995; and Shemansky et al. 1985). Our source follows this trend
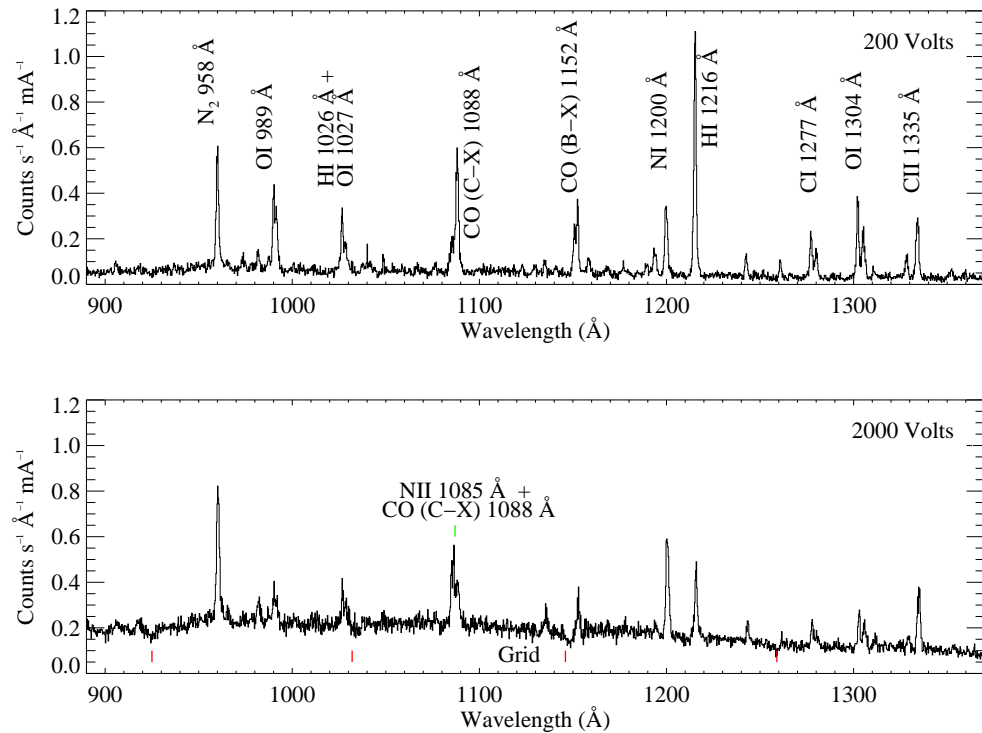
Figure A.11 Two examples of lamp spectra using a CO_2 leak. The low energy spectrum (200 V) is near the peak of the electron-impact cross-sections for the residual species, thus line emission dominates. The high energy spectrum (2000V) shows a stronger continuum from thick target bremsstrahlung, with less line emission. The features marked "Grid" are instrumental.

even though the energy of electrons in the line emitting volume is not mono-energetic.

A.3.3 Impact Cross-Sections, Absolute Calibration, and Reflectivity Tracking

We have found the rise and fall of our Lyman–α intensity (proportional to the impact cross-section) to span a much wider range of target voltage than found in the Ajello work where mono-energetic electrons were used. Our understanding of this discrepancy has been aided by the development of a N-body code to calculate the trajectories of the electrons

103

Target Gas	λ (Å)	Species	Target Gas	λ (Å)	Species
Argon	920	Ar II	Hydrogen	1026	H I
	932	Ar II		1216	H I
	1048	Ar I		several	H_2
	1066	Ar I			
Carbon Dioxide	989	O I	Nitrogen	958	N_2
	1088	CO (C-X)		1084	N II
	1150	CO (B-X)		1135	N I
	1152	O I		1200	N I
	1304	O I			
	1335	C II			
Oxygen	989	O I			
	1027	O I			
	1040	O I			
	1152	O I			
	1304	O I			

Table A.1 Electron-impact target gases measured and their characteristic emission lines.

emitted by the lamp filament and attracted towards the target rod. This code allows us to determine the electron energy distribution within the line emitting region. We found that the average energy of the electrons was ≈ 4.5 of the maximum provided by the target voltage, in good agreement with the expanded energy scale in comparison with Ajello's data. The scale change allowed a much closer match to Ajello's work, and we are now addressing discrepancies associated with the non-mono-energetic electron distribution.

For gas species with known measured cross-sections, an absolute flux can be predicted using these known values as well as a knowledge of the individual species density, electron flux, and the geometry of impact region (James et al. 1997). The electron flux can be measured from the electron emission current, thus, absolute calibration will require two additional quantities, the partial pressure of the emitting species and a detailed understanding of the emitting volume. The partial pressures can be provided by a residual gas analyzer. The emitting volume will come from the N-body calculations.

The extensive set of gas species and energies measured thus far provides data for theoretical calculations seeking to reproduce the emission line intensity variation produced by the integrated distribution of electron energies inherent to the lamp filament-target geome-
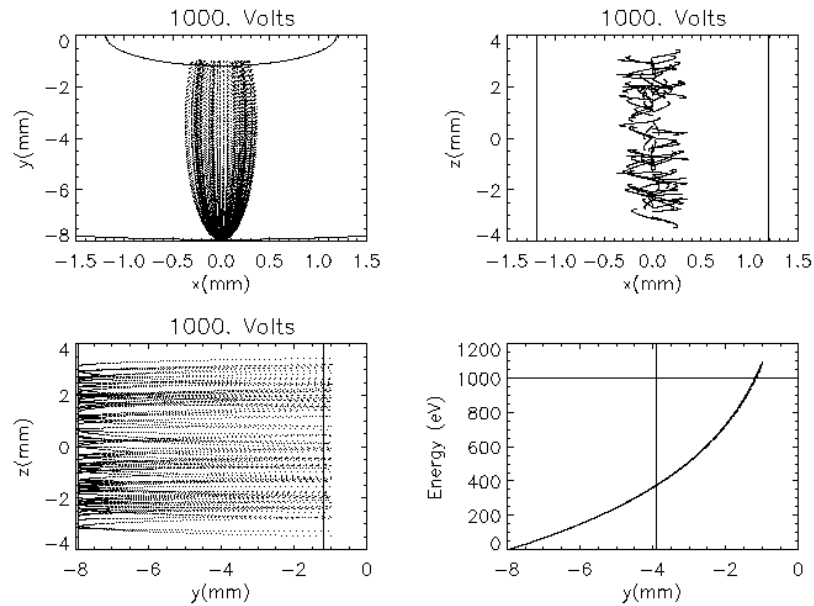
Figure A.12 N-body simulation of the electron trajectories, seen from all three views. The electrons leave the filament with ~ 2 eV and accelerate towards the high voltage tungsten target. *Figure by Stephan McCandliss*

try, a task critical to the development of an absolute calibration. If it is found that we can predict and verify the emission line intensities of a variety of gases and we find that they are repeatable from lamp to lamp, then we can transfer these emission line calibrations to the continuum emission at select wavelengths. We know that the spectral energy distribution of the bremsstrahlung continuum is a slowly varying power law in our wavelength range (Stephenson and Mason 1949) so the transfer of emission line calibrations will in effect provide a means for a self calibrated primary standard at all wavelengths in the bandpass.

To date we have used the present configuration to study the relative calibration offered by the stability and reproducibility of the continuum shape in this bandpass. In these experiments the continuum slope was found to flatten as the target voltage increased, in agreement with the expectations for bremsstrahlung emission. At high target voltage and direct illumination of the spectrograph slit, the spectrum of the continuum closely follows the shape of the absolute calibration curve of the spectrograph to within an arbitrary scale factor.
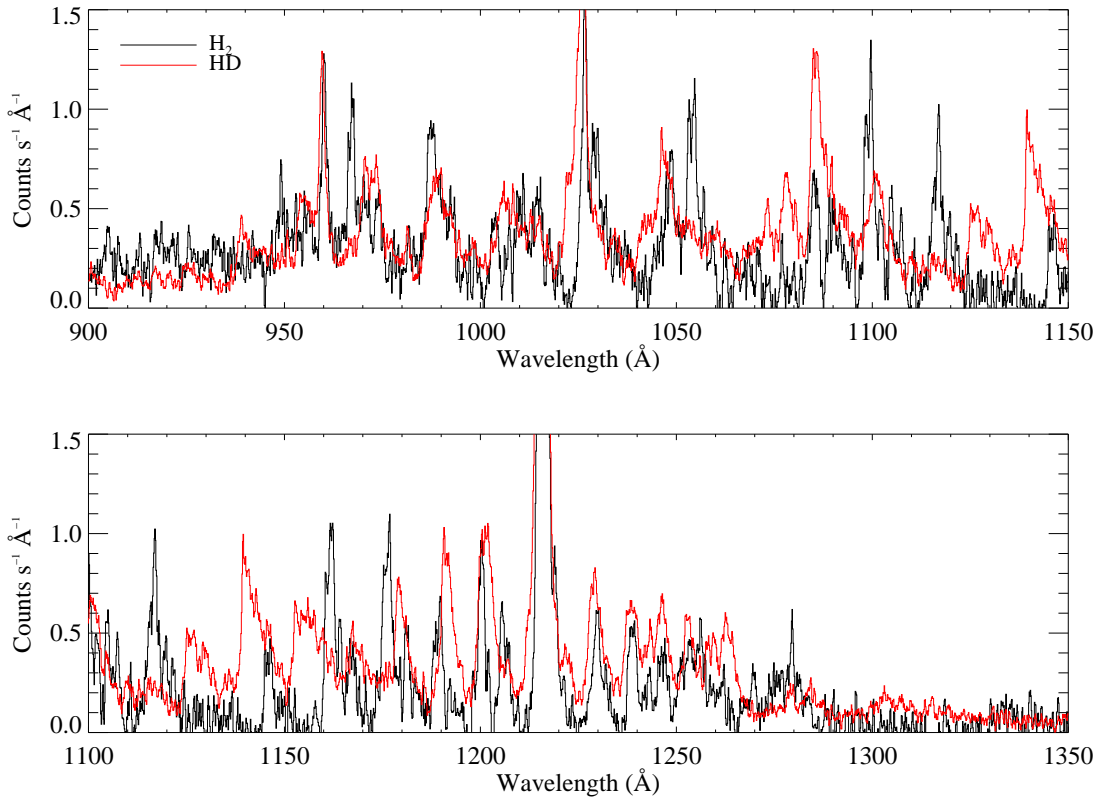
Figure A.13 A comparison of the electron impact excited emission spectra of H_2 and HD. The flux of the HD spectum has been scaled-up to match the peak intensity of Ly-α.
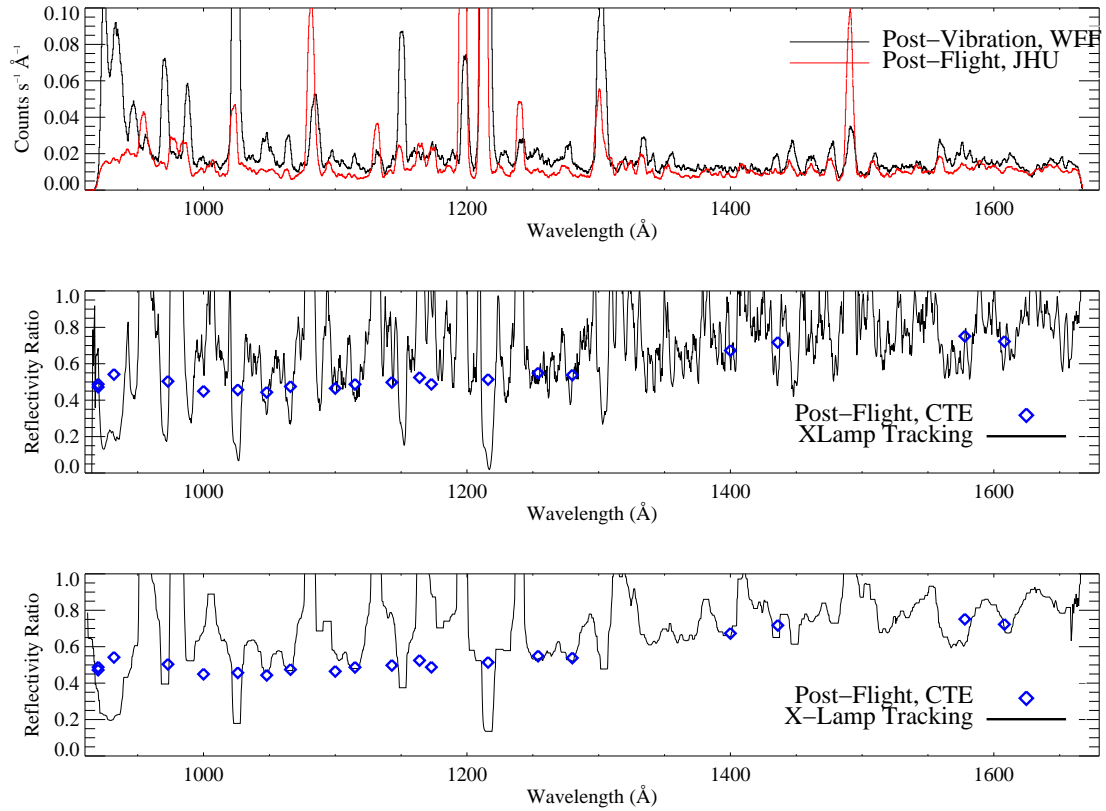
Figure A.14 Top: Reflectivity tracking using lamp spectra obtained during integration and testing compared with post-flight The emission lines are pressure effects, but the difference in continuum level reflects a decrease in reflectivity. Middle and Bottom: Ratios of the spectra, with a median filter applied to the bottom panel. The lamp tracking agrees almost identically with actual mirror measurements made in the CTE.

A ruggedized version of this lamp was used during the integration and testing of the 36.208 mission to track the telescope reflectivity (Figure A.14). A custom port was configured on the shutter door at the entrance of the telescope section, to which a lamp was attached. After various stages of field operations, we would set the lamp to predefined voltage and current settings and record the spectrum with the MCP channel of the LIDOS instrument. We were thus able to track the telescope reflectivity degradation over time during pre-flight procedures. We found that while we were steadily losing reflectivity, the projected level would be acceptable for launch. Comparing the ratio of pre-integration and post-flight spectra taken with this calibration lamp, we found that this matched the ratio of pre and post-flight mirror reflectivities almost perfectly. This lamp was used for ground calibration and was not flight hardware. An electron-impact calibration lamp onboard the LIDOS instrument is described in the next section.

A.3.4 Flight Applications

Figure A.15 shows an onboard version of the calibration lamp integrated into the optical path of the LIDOS instrument. An entrance slit for the lamp is mounted in the copper gasket in the flange joining the lamp to the spectrograph. A deep channel running the diameter of the baseplate allows for the propagation of a beam from the lamp slit into an optical path intercepting the grating and detectors. Both mirrors are made from polished stainless steel and overcoated with ion beam sputtered SiC. The first is a simple $45°$ elliptical flat. The second, located along the telescope optical axis, has a horseshoe shaped cutout to allow an unobstructed passage of the telescope beam, while picking off the faster calibration beam and redirecting it towards the grating.

This lamp was successfully tested on the 36.208 flight. In Figure A.16 we show the lamp spectrum acquired in flight along with one acquired on the ground. These spectra were both acquired in 40 seconds, with the flight spectrum taken after the science portion of the mission. Power remains on for roughly 60 seconds following the closure of the shutter door, and the lamp was turned on by the ground operator (in this instance, the author) at this time. As can be seen the spectra are dominated by Lyman-α, which is somewhat depressed and broadened in the flight data.
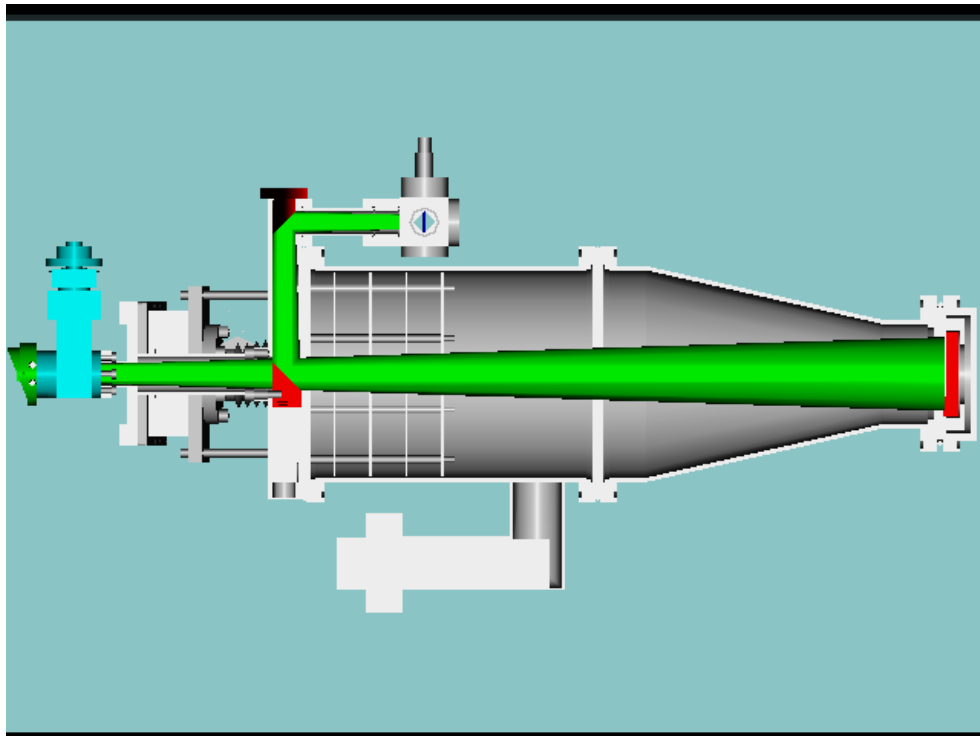
Figure A.15 A cutaway that shows how the lamp has been integrated into the LIDOS instrument. The green rays are from the onboard calibration lamp, the diffraction grating is in red at the far right. *Figure by Stephan McCandliss*.
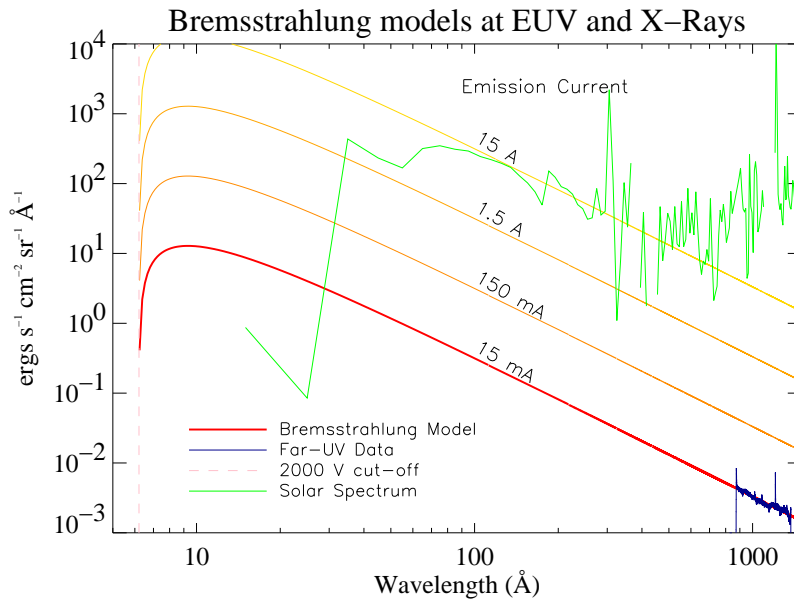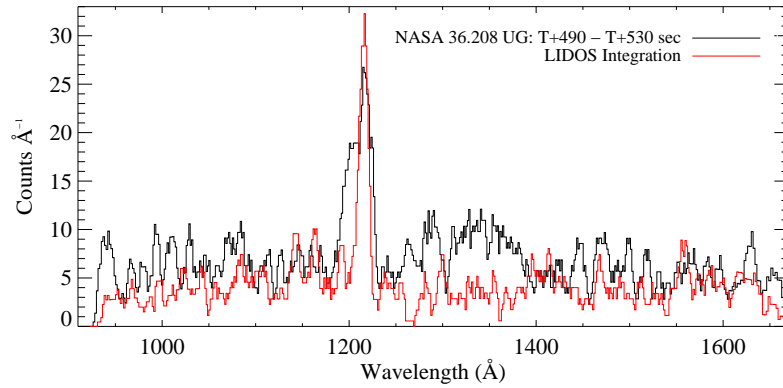
Figure A.16 Top: Flight and ground spectra of the onboard calibration lamp taken by the LIDOS MCP. Bottom: Simulations of the absolute brightness that could be achieved for a given emission current. The top curve is compared to the spectrum of the Sun to illustrate applicability to solar missions.

The demands of the sounding rocket test and flight environments dictate much of the lamp design and operational requirements, many of which are common to longer duration missions. First and foremost of these requirements is that the use of the lamp must not put the acquisition of the primary science data at risk. The instrument must be rugged enough to survive a maximum acceleration in excess of 12 g's during shake testing and launch. A compact design is desired that simplifies the optical layout, has a low power draw, and minimizes heat dissipation. In addition, the total reliance on testing to verify compliance with mission objectives requires equipment that can be operated repeatedly in the flight ready configuration. Figure A.16 shows simulations of how this type of calibration lamp could be used on by longer duration missions observing objects with a wide range of incident fluxes. The power draw becomes substantial, but the top curve shows how this type of lamp could even be applied to solar missions operating inside Earth's orbit.

A.4 Mission Planning and Field Operations

A sounding rocket mission contains many of the components of a long duration orbital astronomy mission, but on a smaller scale. Scientific goals must be identified, an instrument that can address these goals in an appropriate manner must be designed and built, the instrument calibration must be performed, mission planning must be carried out, and finally the instrument must be launched and the data analyzed. The first several sections of this appendix have dealt with most of these aspects through calibration. This final section deals with the mission planning aspect of a rocket flight and what is required of the experiment team to prepare an instrument for launch.

The first stage in the mission planning process following the Mission Initiation Conference with the NASA Sounding Rocket Operations Contract (NSROC) team at Wallops Flight Facility is to determine the exact targets and how they can best be observed. This typically concerns the experimenters and the ACS team (traditionally from the Aerojet corporation, but managed directly by NSROC in the future). The ACS engineers are in charge of the startracker and in-flight attitude control system (the Mark VI system). Precautions must be taken to prevent the startracker from acquiring the wrong star in crowded fields of bright stars, such as the Orion Nebula. Following this, the specific flight plan must be
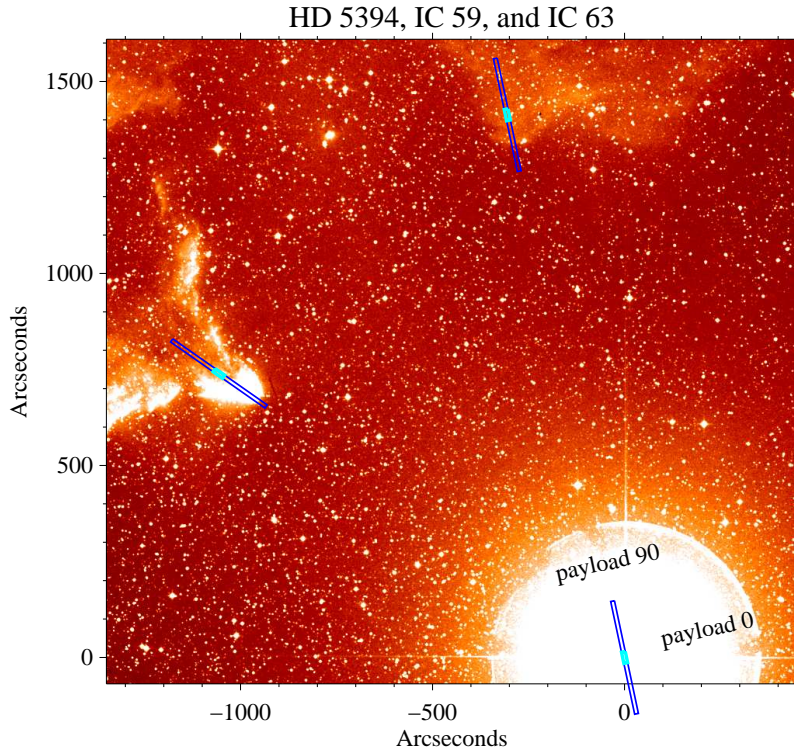
Figure A.17 A DSS image of the γ Cas - IC59/63 system with LIDOS apertures projected on the sky. This image was used during 36.208 mission planning with the ACS team.

developed, and each pointing must be preprogrammed into the ACS system. Figure A.17 shows an example of the three program steps used in the 36.208 flight. These predefined steps can either be taken as a function of time after launch or sent directly from the Command Uplink System (CUS), operated by a member of the experiment team. Furthermore, after the target fields have been acquired, fine adjustments are often required. Nominal pointing requirements for ACS are typically $\pm 5'$, but the $10''$ slit employed by the LIDOS instrument requires more precision. This fine pointing is achieved by experimenter control of the CUS. The CUS can be used to send commands in real-time to the onboard ACS, which employs argon jets to provide three-axis control during the flight. In essence, the CUS allows the experimenter to "drive the star into the slit". The ground operator becomes

familiar with operating the CUS by practicing using a flight simulator. The simulator consists of a visible light collimator that mimics the light from a distant star and an ACS cradle that the rocket rests on. The cradle takes signals from the CUS and uses electric motors to change the payload orientation in the same way as the argon jets used during flight. The 36.208 payload is shown on the cradle in Figure A.18.
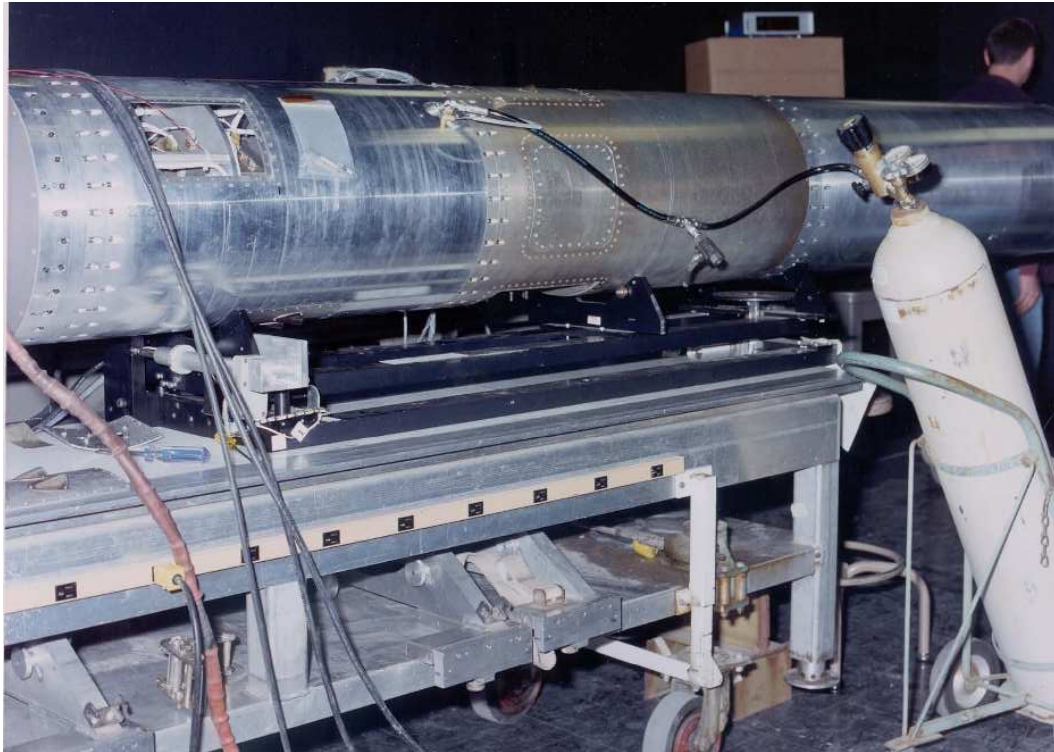
Figure A.18 The 36.208 payload on the ACS cradle for command uplink practice at White Sands Missile Range. The avionics section is at the left. The cylinder next to the rocket contains high-pressure argon for the CCD cooling system.

Once the experiment has been calibrated, field operations begin. For a new payload (such as the 36.208 LIDOS launch), this starts at Wallops before going to White Sands Missile Range for launch. Payloads that have flown before (such as the 36.198 flight) typically opt to perform a field integration at White Sands. Field operations begin with basic electrical and telemetry checks that verify that the experiment is communicating with the telemetry and other vehicle subsystems properly. A sequence test, which is a simulation

of all the events that are expected to occur during the flight, is then performed. After this, a mock startracker with a mirrored surface is installed in the telescope section in order to check the alignment between the telescope and startracker optical axes. This is done by measuring angular positions with a theodolite. When the alignment is confirmed, a series of vibrational tests are performed on the integrated payload. These tests simulate the forces that the rocket will experience during launch. The startracker and sequence tests are then performed again to confirm that all of the systems survived vibration intact.

Following the post-vibrational tests, the payload is disassembled and shipped to White Sands. Another round of sequence tests are performed, and the mock startracker is replaced by the flight unit. A second test is performed to verify that the startracker and telescope are aligned, a simulated star is acquired using by the startracker and it sends error signals to the ACS software. ACS uses these signals to command the cradle to position the star in the center of the tracker field-of-view. Once the startracker is centered, the alignment with the telescope is confirmed by verifying the star is in the middle of the slitjaw imaging camera. Once all these tests have been completed and the payload has been fully reassembled, it is moved to the launch pad.

Upon arrival at the pad, the payload is attached to the launcher (also known as "the rail") and connected to the rocket motors. The motors are made up of two stages, a booster that fires for the first 6 seconds of the flight and a sustainer that fires for approximately 32 more seconds after the booster has fallen away. A pump-out stack is attached to maintain the payload vacuum during operations on the launcher. Electrical checks are made and a final sequence test is performed with the rocket assembled on the launch pad. On the night of the launch, the experiment team goes out to the launch pad at T - 2 hours to remove and secure the pump system. The experimenters then go into a nearby blockhouse or to the ground command station to monitor payload voltages until launch. Launch occurs when the booster stage fires. At roughly T + 80 seconds, the payload shutter door is opened and the startracker updates its position by observing two bright stars before acquiring the science target. On-target fine pointing corrections are described above. 300 – 400 seconds of observing time are followed by the closing of the shutter door around T + 475 seconds. A parachute is deployed after reentry and the payload is recovered the following morning (Figure A.19). Post-flight calibrations are a repeat of the pre-flight steps described earlier

114

Figure A.19 Recovery operations for 36.198 at White Sands Missile Range, 2001 February 10. JHU engineer Russ Pelton and the author are shown. The payload is then transported back to the VAB for disassembly and shipping.

in the appendix. The subsequent data analysis forms the basis for a scientific study such as the one found in this dissertation.

Bibliography

Abel, N. P., C. L. Brogan, G. J. Ferland, C. R. O'Dell, G. Shaw, and T. H. Troland (2004, July). Physical Conditions in Orion's Veil. *ApJ 609*, 247–260.

Ajello, J. M., G. K. James, B. O. Franklin, and D. E. Shemansky (1989, October). Medium-resolution studies of extreme ultraviolet emission from N2 by electron impact - Vibrational perturbations and cross sections of the c4-prim e 1Sigma(+)u and b-prime 1Sigma(+)u states. *Phys. Rev. A 40*, 3524–3556.

Ajello, J. M., G. K. James, and D. E. Shemansky (1991, April). Cross sections for production of H(2p, 2s, 1s) by electron collisi onal dissociation of H2. *ApJ 371*, 422–431.

Arrieta, A. and S. Torres-Peimbert (2003, July). Broad Hα Wings in Nebulae around Evolved Stars and in Young Planetary Nebulae. *ApJS 147*, 97–102.

Bagnuolo, W. G., R. L. Riddle, D. R. Gies, and D. J. Barry (2001). ι Orionis – Evidence for a Capture Orgin Binary. *ApJ 554*, 362–367.

Bautista, M. A., R. W. Pogge, and D. L. Depoy (1995, October). The Nebular Extinction in the Orion Nebula. *ApJ 452*, 685–+.

Bayard, R. T. and D. Alpert (1950). Extension of the low pressure range of the ionization gauge. *Rev. Sci. Instr. 21*, 571.

Birriel, J. J. (2004, September). Raman-Scattered He II at 4851 Å in the Symbiotic Stars HM Sagittae and V1016 Cygni. *ApJ 612*, 1136–1139.

Birriel, J. J., B. R. Espey, and R. E. Schulte-Ladbeck (2000, December). Contemporaneous Ultraviolet and Optical Observations of Direct and Raman-scattered O VI Lines in Symbiotic Stars. *ApJ 545*, 1020–1033.

Blaauw, A. and W. W. Morgan (1954, May). The Space Motions of AE Aurigae and μ Columbae with Respect to the Orion Nebula. *ApJ 119*, 625–+.

Bohlin, R. C. and B. D. Savage (1981, October). Ultraviolet interstellar extinction toward stars in the Orion Nebula and toward HD 147889. *ApJ 249*, 109–117.

Burgh, E. B., S. R. McCandliss, and P. D. Feldman (2002). Rocket Observations of Far-ultraviolet Dust Scattering in NGC 2023. *ApJ 575*, 240–249.

Burgh, E. B., S. R. McCandliss, R. Pelton, K. France, and P. D. Feldman (2001). Windowless Vacuum Ultraviolet Collimator. In *Proceedings of the SPIE*, Volume 4498.

Burton, M. G., P. W. J. L. Brand, T. R. Geballe, and A. S. Webster (1989, January). Molecular hydrogen line ratios in four regions of shock-excited gas. *MNRAS 236*, 409–423.

Buss, R. H., J. W. Kruk, and H. C. Ferguson (1995, November). New Far-Ultraviolet Intrinsic Spectral Fluxes of Hot Stars and Their Photospheric Temperatures. *ApJ 454*, L55+.

Calzetti, D. (1997, January). Reddening and Star Formation in Starburst Galaxies. *AJ 113*, 162–184.

Calzetti, D., R. C. Bohlin, K. D. Gordon, A. N. Witt, and L. Bianchi (1995, June). Scattering Properties of the Dust in the Reflection Nebula IC 435. *ApJ 446*, L97+.

Cardelli, J. A., G. C. Clayton, and J. S. Mathis (1989, October). The relationship between infrared, optical, and ultraviolet extinction. *ApJ 345*, 245–256.

Carruthers, G. R. (1970, August). Rocket Observation of Interstellar Molecular Hydrogen. *ApJ 161*, L81+.

Cazaux, S. and A. Tielens (2002). Molecular Hydrogen Formation in the Interstellar Medium. *ApJL 575*, L29–L32.

118

Danforth, C. W., J. C. Howk, A. W. Fullerton, W. P. Blair, and K. R. Sembach (2002, March). An Atlas of Far Ultraviolet Spectroscopic Explorer Sight Lines toward the Magellanic Clouds. *ApJS 139*, 81–189.

Davidsen, A. F., K. S. Long, S. T. Durrance, W. P. Blair, C. W. Bowers, S. J. Conard, P. D. Feldman, H. C. Ferguson, G. H. Fountain, R. A. Kimble, G. A. Kriss, H. W. Moos, and K. A. Potocki (1992, June). The Hopkins Ultraviolet Telescope - Performance and calibration during the Astro-1 mission. *ApJ 392*, 264–271.

Draine, B. T. (1978, April). Photoelectric heating of interstellar gas. *ApJS 36*, 595–619.

Draine, B. T. (2003a). Interstellar Dust Grains. *ARA&A 41*, 241–289.

Draine, B. T. (2003b, December). Scattering by Interstellar Dust Grains. I. Optical and Ultraviolet. *ApJ 598*, 1017–1025.

Duley, W. W. and D. A. Williams (1980, December). H2 fluorescence and the diffuse galactic light in the vacuum ultraviolet. *ApJ 242*, L179–L182.

Fastie, W. G. and D. E. Kerr (1975, September). Spectroradiometric calibration techniques in the far ultraviolet - A stable emission source for the Lyman bands of molecular hydrogen. *Appl. Opt. 14*, 2133–2142.

Fitzpatrick, E. L. and D. Massa (1990). An analysis of the shapes of ultraviolet extinction curves. III. An atlas of ultraviolet extinction curves. *ApJS 72*, 163–189.

France, K., B.-G. Andersson, S. R. McCandliss, and P. D. Feldman (2005, August). Fluorescent Molecular Hydrogen Emission in IC 63: FUSE, Hopkins Ultraviolet Telescope, and Rocket Observations . *ApJ 628*, 750–757.

France, K. and S. R. McCandliss (2005). Molecular Hydrogen in Orion as Observed by *FUSE*. *ApJ 629*, 97–100.

France, K., S. R. McCandliss, E. B. Burgh, and P. D. Feldman (2004, November). Rocket and *FUSE* Observations of IC 405 Differential Extinction and Fluorescent Molecular Hydrogen. *ApJ 616*, 257–265.

Gatley, I., T. Hasegawa, H. Suzuki, R. Garden, P. Brand, J. Lightfoot, W. Glencross, H. Okuda, and T. Nagata (1987, July). Fluorescent molecular hydrogen emission from the reflection nebula NGC 2023. *ApJ 318*, L73–L76.

Gibson, S. J. and K. H. Nordsieck (2003, May). The Pleiades Reflection Nebula. I. Ultraviolet, Optical, and Far-Infrared Imaging Photometry. *ApJ 589*, 347–361.

Gizis, J. E., H. L. Shipman, and J. A. Harvin (2005, September). First Ultraviolet Spectrum of a Brown Dwarf: Evidence for H_2 Fluorescence and Accretion. *ApJ 630*, L89–L91.

Gordon, K. D., K. A. Misselt, A. N. Witt, and G. C. Clayton (2001). The DIRTY Model. I. Monte Carlo Radiative Transfer Through Dust. *ApJ 551*, 269–276.

Gordon, K. D., A. N. Witt, G. R. Carruthers, S. A. Christensen, and B. C. Dohne (1994, September). The far-ultraviolet dust albedo in the Upper Scorpius subgroup of the Scorpius OB2 association. *ApJ 432*, 641–647.

Habart, E., F. Boulanger, L. Verstraete, C. M. Walmsley, and G. Pineau des Forêts (2004, February). Some empirical estimates of the H_2 formation rate in photon-dominated regions. *A&A 414*, 531–544.

Hartig, G. F., W. G. Fastie, and A. F. Davidsen (1980, March). Rocket instrument for far-UV spectrophotometry of faint astronomical objects. *Appl. Opt. 19*, 729–740.

Henyey, L. C. and J. L. Greenstein (1941, January). Diffuse radiation in the Galaxy. *ApJ 93*, 70–83.

Herbig, G. H. (1999, July). Examination of the Interstellar Spectrum of AE AUR for Long-Term Changes. *PASP 111*, 809–811.

Herzberg, G. (1950). *Molecular Spectra and Molecular Structure*. D. Van Nostrad Company.

Herzberg, G. and H. Huber (1960). *Constants of Diatomic Molecules*. D. Van Nostrad Company.

Hollenbach, D. and A. Tielens (1997). Dense Photodissociation Regions. *Annual Reviews of Astronomy and Astrophysics 35*, 179–215.

Huggins, P. J., T. Forveille, R. Bachiller, P. Cox, N. Ageorges, and J. R. Walsh (2002, July). High-Resolution CO and H_2 Molecular Line Imaging of a Cometary Globule in the Helix Nebula. *ApJ 573*, L55–L58.

Hummer, D. G. (1962). Non-coherent scattering: I. The redistribution function with Doppler broadening. *MNRAS 125*, 21–37.

Hurwitz, M. (1998, June). Far-Ultraviolet Fluorescence of Molecular Hydrogen in IC 63. *ApJ 500*, L67+.

James, G. K., J. A. Slevin, D. E. Shemansky, J. W. McConkey, I. Bray, D. Dziczek, I. Kanik, and J. M. Ajello (1997, February). Optical excitation function of H(1s-2p) produced by electron impac t from threshold to 1.8 keV. *Phys. Rev. A 55*, 1069–1087.

Jansen, D. J., E. F. van Dishoeck, and J. H. Black (1994, February). Physical and chemical structure of the IC 63 nebula. 1: Millimeter and far-infrared observations. *A&A 282*, 605–620.

Jenkins, E. B. and A. Peimbert (1997, March). Molecular Hydrogen in the Direction of zeta Orionis A. *ApJ 477*, 265–+.

Kanik, I., G. K. James, and J. M. Ajello (1995, March). Medium-resolution studies of extreme-ultraviolet emission from CO by electron impact. *Phys. Rev. A 51*, 2067–2074.

Karr, J. L., A. Noriega-Crespo, and P. G. Martin (2005, February). A Multiwavelength study of IC 63 and IC 59. *AJ 129*, 954–968.

Kastner, S. O. (1991, November). The symbiotic stellar lines at 6830 A, 7088 A - an origin in optically thick fluorescence. *Ap&SS 185*, 265–275.

Kristensen, L. E., M. Gustafsson, D. Field, G. Callejo, J. L. Lemaire, L. Vannier, and G. Pineau des Forêts (2003, December). H_2 excitation imaging of the Orion Molecular Cloud. *A&A 412*, 727–734.

Le Petite, F., P. Boisse, E. Pineau des Forets, G. a nd Roueff, C. Gry, B.-G. Andersson, and V. Le Brun (2001). FUSE Observations towards HD 34078 Detection of highly excited H2 and HD. *astro-ph 0110358*, pre–print.

Leitherer, C., I.-H. Li, D. Calzetti, and T. M. Heckman (2002, June). Global Far-Ultraviolet (912-1800 Å) Properties of Star-forming Galaxies. *ApJS 140*, 303–329.

Liu, W. and A. Dalgarno (1996, May). The Ultraviolet Spectrum of the Jovian Dayglow. *ApJ 462*, 502–+.

Luhman, M. L., D. T. Jaffe, L. D. Keller, and S. Pak (1994, December). H2 emission as a tracer of molecular hydrogen: Large-scale observations of Orion. *ApJ 436*, L185–L188.

Luhman, M. L., K. L. Luhman, T. Benedict, D. T. Jaffe, and J. Fischer (1997). Near-Infrared Spectra of IC 59/63 and NGC 1535: Comparing Infrared and Ultraviolet Observations of H_2. *ApJL 480*, L133–L136.

Lupu, R. E., S. R. McCandliss, and K. France (2006, January). M 27 with Cloudy. *ApJ 1*, 1–10.

Maíz-Apellániz, J., N. R. Walborn, H. Á. Galué, and L. H. Wei (2004, March). A Galactic O Star Catalog. *ApJS 151*, 103–148.

Martini, P., K. Sellgren, and D. DePoy (1999). Near-Infrared Spectroscopy of Molecular Hydrogen in Four Reflection Nebulae: NGC 1333, NGC 2023, NGC 2068, and NGC 7023. *ApJ 526*, 772–787.

Massa, D. and E. L. Fitzpatrick (2000, February). A Recalibration of IUE NEWSIPS Low-Dispersion Data. *ApJS 126*, 517–535.

Mathis, J. S. (1990). Interstellar dust and extinction. *ARA&A 28*, 37–70.

Mathis, J. S., B. A. Whitney, and K. Wood (2002, August). Can Reflection from Grains Diagnose the Albedo? *ApJ 574*, 812–821.

McCandliss, S. R. (2003, June). Molecular Hydrogen Optical Depth Templates for FUSE Data Analysis. *PASP 115*, 651–661.

McCandliss, S. R., B. Burgh, E., and P. D. Feldman (2000). Flyable Windowless Calibration Lamps for Far-UV Spectroscopy. In *Proceedings of the SPIE*, Volume 4139.

McCandliss, S. R., K. France, P. D. Feldman, and R. Pelton (2003, February). Long-slit imaging dual-order spectrograph: LIDOS. In *Future EUV/UV and Visible Space Astrophysics Missions and Instrumentation. Edited by J. Chris Blades, Oswald H. W. Siegmund. Proceedings of the SPIE, Volume 4854, pp. 385-396 (2003).*, pp. 385–396.

McCandliss, S. R., M. E. Martinez, P. D. Feldman, R. Pelton, R. A. Keski-Kuha, and J. S. Gum (1994). Design and fabrication of a 40-cm-diameter SiC-coated normal incidence telescope and spectrometer. In *Proceedings of the SPIE*, Volume 2011.

McCandliss, S. R., K. R. Sembach, E. B. Burgh, K. France, P. D. Feldman, and J. Kruk (2005, December). Observations od Excited Molecular Hydrogen in M 27. *ApJ 1*, 1–10.

McPhate, J. B., P. D. Feldman, S. R. McCandliss, and E. B. Burgh (1999, August). Rocket-borne Long-Slit Ultraviolet Spectroscopy of Comet Hale-Bopp. *ApJ 521*, 920–927.

Meurer, G. R., T. M. Heckman, and D. Calzetti (1999, August). Dust Absorption and the Ultraviolet Luminosity Density at Z˜3 as Calibrated by Local Starburst Galaxies. *ApJ 521*, 64–80.

Meyer, D. M., J. T. Lauroesch, U. J. Sofia, B. T. Draine, and F. Bertoldi (2001, May). The Rich Ultraviolet Spectrum of Vibrationally Excited Interstellar H_2 toward HD 37903. *ApJ 553*, L59–L62.

Moos, H. W. et la. (2000, July). Overview of the Far Ultraviolet Spectroscopic Explorer Mission. *ApJ 538*, L1–L6.

Murthy, J., A. Dring, R. C. Henry, J. W. Kruk, W. P. Blair, R. A. Kimble, and S. T. Durrance (1993). Hopkins Ultraviolet Telescope observations of far-ultraviolet scattering in NGC 7023 - The dust albedo. *ApJL 408*, L97–L100.

Murthy, J. and D. J. Sahnow (2004, November). Observations of the Diffuse Far-Ultraviolet Background with the Far Ultraviolet Spectroscopic Explorer. *ApJ 615*, 315–322.

Murthy, J., D. J. Sahnow, and R. C. Henry (2005, January). Intense Diffuse Far-UV Emission from the Orion Nebula. *ApJ 618*, 99–102.

O'Dell, C. R. (2000, May). On the Nature of Linear Structures in the Helix and Orion Nebulae. *AJ 119*, 2311–2318.

Palik, E. D. (1985). *Handbook of optical constants of solids*. Academic Press Handbook Series, New York: Academic Press, 1985, edited by Palik, Edward D.

Peeters, E., A. L. Mattioda, D. M. Hudgins, and L. J. Allamandola (2004, December). Polycyclic Aromatic Hydrocarbon Emission in the 15-21 Micron Region. *ApJ 617*, L65–L68.

Pellerin, A., A. W. Fullerton, C. Robert, J. C. Howk, J. B. Hutchings, N. R. Walborn, L. Bianchi, P. A. Crowther, and G. Sonneborn (2002, November). An Atlas of Galactic OB Spectra Observed with the Far Ultraviolet Spectroscopic Explorer. *ApJS 143*, 159–200.

Penny, L. R. (1996, June). Projected Rotational Velocities of O-Type Stars. *ApJ 463*, 737–+.

Rachford, B. L., T. P. Snow, J. Tumlinson, J. M. Shull, W. P. Blair, R. Ferlet, S. D. Friedman, C. Gry, E. B. Jenkins, D. C. Morton, B. D. Savage, P. Sonnentrucker, A. Vidal-Madjar, D. E. Welty, and D. G. York (2002, September). A Far Ultraviolet Spectroscopic Explorer Survey of Interstellar Molecular Hydrogen in Translucent Clouds. *ApJ 577*, 221–244.

Rauch, T., J. Koeppen, and K. Werner (1994, June). Spectral analysis of the planetary nebula K 1-27 and its very hot hydrogen-deficient central star. *A&A 286*, 543–554.

Redfield, S., J. L. Linsky, T. B. Ake, T. R. Ayres, A. K. Dupree, R. D. Robinson, B. E. Wood, and P. R. Young (2002, December). A Far Ultraviolet Spectroscopic Explorer Survey of Late-Type Dwarf Stars. *ApJ 581*, 626–653.

Roberge, A. (2003, April). Ultraviolet spectroscopy of circumstellar disks. *Ph.D. Thesis*.

Rollinde, E., P. Boissé, S. R. Federman, and K. Pan (2003, April). Small scale structure in molecular gas from multi-epoch observations of HD 34078. *A&A 401*, 215–226.

Sahnow, D. J. et al. (2000, July). On-Orbit Performance of the Far Ultraviolet Spectroscopic Explorer Satellite. *ApJ 538*, L7–L11.

Sasseen, T. P., M. Hurwitz, W. V. Dixon, and S. Airieau (2002, February). A New Measurement of the Average Far-Ultraviolet Extinction Curve. *ApJ 566*, 267–275.

Schmid, H. M. (1989, March). Identification of the emission bands at 6830, 7088 A. *A&A 211*, L31–L34.

Shaw, G., G. J. Ferland, N. P. Abel, P. C. Stancil, and P. A. M. van Hoof (2005, May). Molecular Hydrogen in Star-forming Regions: Implementation of its Microphysics in CLOUDY. *ApJ 624*, 794–807.

Shemansky, D. E., D. T. Hall, and J. M. Ajello (1985, September). Electron impact excitation of H2 - Rydberg band systems and the be nchmark dissociative cross section for H Lyman-alpha. *ApJ 296*, 765–773.

Shull, M. and S. Beckwith (1982). Interstellar Molecular Hydrogen . *Annual Reviews of Astronomy and Astrophysics 30*, 163–190.

Siegmund, O. H., M. A. Gummin, J. M. Stock, D. R. Marsh, R. Raffanti, and J. Hull (1993, November). High-resolution monolithic delay-line readout techniques for two-dimensional microchannel plate detectors. In *Proc. SPIE Vol. 2006, p. 176-187, EUV, X-Ray, and Gamma-Ray Instrumentation for Astronomy IV, Oswald H. Siegmund; Ed.*, pp. 176–187.

Speck, A. K., M. Meixner, D. Fong, P. R. McCullough , D. E. Moser, and T. Ueta (2002, January). Large-Scale Extended Emission around the Helix Nebula: Dust, Mo lecules, Atoms, and Ions. *AJ 123*, 346–361.

Spitzer, L. (1978). *Physical processes in the interstellar medium*. New York Wiley-Interscience, 1978. 333 p.

Spitzer, L., W. D. Cochran, and A. Hirshfeld (1974, October). Column densities of inter-stellar molecular hydrogen. *ApJS 28*, 373–389.

Stecher, T. P. and D. A. Williams (1967, July). Photodestruction of Hydrogen Molecules in H I Regions. *ApJ 149*, L29+.

Stephenson, S. T. and F. D. Mason (1949, June). Continuous X-Ray Spectrum from 8A to 14A. *Phys. Rev. 11*, 1711–1716.

Sternberg, A. (1989). Ultraviolet fluorescent molecular hydrogen emisson. *ApJ 347*, 863–874.

Takahashi, J. and H. Uehara (2001, November). H_2 Emission Spectra with New Formation Pumping Models. *ApJ 561*, 843–857.

Takami, M., T. Usuda, H. Sugai, H. Kawabata, H. Suto, and M. Tanaka (2000). H_2 Line Ratios to Discriminate Dense Photodissociation Regions from Shocks: Application to NGC 2023 and NGC 7023. *ApJ 529*, 268–278.

Treffers, R. R., U. Fink, H. P. Larson, and T. N. Gautier (1976, November). The spectrum of the planetary nebula NGC 7027 from 0.9 to 2.7 microns. *ApJ 209*, 793–799.

Valencic, L. A., G. C. Clayton, and K. D. Gordon (2004, December). Ultraviolet Extinction Properties in the Milky Way. *ApJ 616*, 912–924.

van Dishoeck, E. F. (2004, September). ISO Spectroscopy of Gas and Dust: From Molec-ular Clouds to Protopl anetary Disks. *ARA&A 42*, 119–167.

Verstraete, L., C. Pech, C. Moutou, K. Sellgren, C. M. Wright, M. Giard, A. Léger, R. Tim-mermann, and S. Drapatz (2001, June). The Aromatic Infrared Bands as seen by ISO-SWS: Probing the PAH model. *A&A 372*, 981–997.

Vijh, U. P., A. N. Witt, and K. D. Gordon (2003, April). The Dust in Lyman Break Galaxies. *ApJ 587*, 533–543.

Vijh, U. P., A. N. Witt, and K. D. Gordon (2004, May). Discovery of Blue Luminescence in the Red Rectangle: Possible Fluorescence from Neutral Polycyclic Aromatic Hydrocarbon Molecules? *ApJ 606*, L65–L68.

Walborn, N. R., A. W. Fullerton, P. A. Crowther, L. Bianchi, J. B. Hutchings, A. Pellerin, G. Sonneborn, and A. J. Willis (2002, August). Far Ultraviolet Spectroscopic Explorer Atlas of OB Stars in the Magellanic Clouds. *ApJS 141*, 443–468.

Weingartner, J. C. and B. T. Draine (2001). Dust Grain-Size Distributions and Extinction in the Milky Way, Large Magellanic Cloud, and Small Magellanic Cloud. *ApJ 548*, 296–309.

Werner, M. W., K. I. Uchida, K. Sellgren, M. Marengo , K. D. Gordon, P. W. Morris, J. R. Houck, and J. A. Stansberry (2004, September). New Infrared Emission Features and Spectral Variations in NGC 7023 . *ApJS 154*, 309–314.

Wilkinson, E., G. M. Harper, A. Brown, and G. J. Herczeg (2002, August). The Far-Ultraviolet Spectrum of T Tauri between 912 and 1185 Å. *AJ 124*, 1077–1081.

Witt, A. N. and D. F. Malin (1989, December). The extended red emission filaments in NGC 2023. *ApJ 347*, L25–L27.

Witt, A. N., J. K. Petersohn, J. B. Holberg, J. Murthy, A. Dring, and R. C. Henry (1993). Voyager 2 Observations of NGC 7023: Dust Scattering Shortward of 1600 Å. *ApJ 410*, 714–718.

Witt, A. N., T. P. Stecher, and R. C. Boroson, T. A. an d Bohlin (1989). UV Fluorescence of Molecular Hydrogen and Red Dust Emission in the Gamma Cassiopeiae Nebula IC 63. *ApJL 336*, L21–L24.

Witt, A. N., G. A. H. Walker, R. C. Bohlin, and T. P. Stecher (1982, October). The scattering phase function of interstellar grains - The case of the reflection nebula NGC 7023. *ApJ 261*, 492–509.

Wolven, B. C., P. D. Feldman, D. F. Strobel, and M. A. McGrath (1997, February). Ly alpha-induced Fluorescence of H 2 and CO in Hubble Space Telescope Spectra of a Comet Shoemaker-Levy 9 Impact Site on Jupiter. *ApJ 475*, 835–+.

Wood, B. E. and M. Karovska (2004, January). Molecular Hydrogen Emission Lines in Far Ultraviolet Spectroscopic Explorer Observations of Mira B. *ApJ 601*, 502–511.

Vita

Kevin Christopher France was born in Dearborn, Michigan, on 1978 February 07. He attended school in Charleston, West Virginia, graduating in 1996 May with Honors from Charleston Catholic High School. In the fall of 1996, he began studies at Boston University. During his time there, he started his reseach career in the Center for Space Physics' Ultraviolet Research Group. In this capacity, he assisted in the testing and design of the *TERRIERS* satellite, the SPINR sounding rocket, and the visible light prototype for the rocket-borne SCARI absorption spectrograph. He graduated *magna cum laude* with Distinction in 2000 May with a BA in Physics and Astronomy, winning the College Prize in Astronomy, the highest undergraduate honor awarded by the university. In 2000 September, he began graduate school at the Johns Hopkins University, employed as a research assistant with the Sounding Rocket Group. In this role, he has been the lead graduate student on two sounding rocket flights and several guest investigator proposals for observing time with *FUSE*, *Spitzer*, and APO.